Unterschrift BetreuerIn

TECHNISCHE
UNIVERSITÄT
WIEN
Vienna University of Technology

DIPLOMARBEIT

Sprayed silver nanowire networks coated with nanoparticles and polymers as transparent electrodes on flexible substrates

ausgeführt am Austrian Institute of Technology
in Kooperation mit der Technischen Universität Wien

betreut von
Dr. Theodoros Dimopoulos (AIT)
und
Prof. Dr. Christian Edtmaier (TUW)

verfasst von

Katharina Rauchenwald, B.Sc.

09. November 2021

Unterschrift StudentIn

Abstract

Networks of silver nanowires (AgNWs) gain attention as transparent electrodes (TEs) that combine low sheet resistance (R_s) and high optical transmittance (T). TEs on basis of AgNW-networks on low-cost, flexible Polycarbonate (PC) were developed. Efforts were pursued to keep the processing temperature below the glass transition of the PC-substrate. The AgNWs were combined with coatings of a) zinc oxide nanoparticles (ZnONPs) and b) poly(3,4-ethylendioxythiophene)-poly(styrenesulfonate) (PEDOT:PSS). Ultrasonic spraying was the deposition method of choice, a convenient technique for industrial production. Deposition parameters were systematically studied and optimized to obtain high-performance TEs. ZnONP- and PEDOT:PSS-coatings decrease the R_s of sparse AgNW-networks, most prominently PEDOT:PSS, due to a decrease in the junction-resistance. The R_s of a representative sample of PC/AgNW was reduced from initially 21 Ω/sq to 11 Ω/sq by PEDOT:PSS-coating. Experimental results were used in percolation modelling, where material parameters, such as the critical AgNW surface fraction (ϕ_c) and the critical exponent (t) were extracted. The ϕ_c and t are decreased by the coatings. While the coating with PEDOT:PSS does not influence the haze, the coating with ZnONPs increases the surface roughness and the optical haze (H). The roughness results from coffee rings and is partly controllable through the adjustment of spray-coating parameters of ZnONPs. The coatings are shown to sufficiently protect the AgNWs from premature electrical degradation, when stored in ambient atmosphere and at 70 °C for one month. The TEs a) PC/ZnONP/AgNW/ZnONP (H ≈ 0.3, T ≈ 0.8, R_s ≈ 10 Ω/sq) and b) PC/AgNW/PEDOT:PSS (H ≈ 0.1, T ≈ 0.8, R_s ≈ 10 Ω/sq) were tested as transparent heaters. For an applied voltage of 3.5 V, surface temperature increases of + 65 °C (PC/ZnONP/AgNW/ZnONP) and + 80 °C (PC/AgNW/PEDOT:PSS) were obtained. We show, that high-quality transparent electrodes, suitable for various applications, can be fabricated at 100 °C by ultrasonic spray-coating on flexible substrates.

Zusammenfassung

Transparente Elektroden (TE) auf Basis von Silber-Nanodrähten (AgNW) zeichnen sich durch einen niedrigen Flächenwiderstand (R_s) und eine hohe optische Transparenz (T) aus. Die Diplomarbeit beschäftigte sich mit der Entwicklung von AgNW-Kompositen auf Polycarbonat (PC). Das flexible PC-Substrat limitiert die maximale Abscheidungstemperatur aufgrund der niedrigen Glasübergangstemperatur. AgNW-Netzwerke wurden in Schichtkomposite mit a) Zink Oxid Nanopartikeln (ZnONP) und b) Poly-3,4-ethylen-dioxythiophen Polystyrolsulfonat (PEDOT:PSS) eingebracht, um optische und elektrische Eigenschaften zu optimieren und die Stabilität der TE zu verbessern. Eine mit Rolle-zu-Rolle Verfahren kompatible Ultraschall-Sprühmethode wurde verwendet und die Abscheidungsparameter wurden optimiert. Die Kombination von AgNW-Netzwerken mit ZnONP und vorallem mit PEDOT:PSS reduziert den Widerstand der TE. Es konnte eine Senkung von R_s einer repräsentativen Probe PC/AgNW von 21 Ω/sq auf 11 Ω/sq in PC/AgNW/PEDOT:PSS erzielt werden. Experimentelle Daten wurden mit Perkolationsmodellen beschrieben, um zusätzliche Informationen über die kritische AgNW-Dichte (ϕ_c) und den kritischen Exponenten (t) zu erlangen. Durch das Beschichten von AgNW-Netzwerken wurden ϕ_c und t gesenkt. Dies ist durch eine Verringerung des Widerstands an AgNW-Knotenpunkten erklärbar. Gesprühte ZnONP-Schichten erhöhen aufgrund des Kaffeering-Effekts die Oberflächenrauheit und somit die optische Trübung (H). ZnONP- und PEDOT:PSS-Beschichtungen schützen AgNW-Netzwerke vor frühzeitiger, elektrischer Degradierung bei Lagerung für ein Monat bei 70°C und Umgebungsluft. Die Elektroden a) PC/ZnONP/AgNW/ZnONP (H ≈ 0,3; T ≈ 0,8; R_s ≈ 10 Ω/sq) und b) PC/AgNW/PEDOT:PSS (H ≈ 0,1; T ≈ 0,8; R_s ≈ 10 Ω/sq) wurden als transparente Heizelemente untersucht. Durch das Anlegen einer Spannung von 3,5 V konnten Oberflächentemperaturanstiege von + 65 °C (PC/ZnONP/AgNW/ZnONP) und + 80 °C (PC/AgNW/PEDOT:PSS) erzielt werden. Es konnte gezeigt werden, dass leistungsstarke transparente Elektroden, welche verschiedene Anwendungen finden können, auf Basis von beschichteten AgNW-Netzwerken bei 100 °C aus Lösung und auf flexiblen Substraten hergestellt werden können.

Eidesstattliche Erklärung

Ich erkläre an Eides statt, dass die vorliegende Arbeit nach den anerkannten Grundsätzen für wissenschaftliche Abhandlungen von mir selbstständig erstellt wurde. Alle verwendeten Hilfsmittel, insbesondere die zugrunde gelegte Literatur, sind in dieser Arbeit genannt und aufgelistet. Die aus den Quellen wörtlich entnommenen Stellen, sind als solche kenntlich gemacht. Das Thema dieser Arbeit wurde von mir bisher weder im In- noch Ausland einer Beurteilerin/einem Beurteiler zur Begutachtung in irgendeiner Form als Prüfungsarbeit vorgelegt. Diese Arbeit stimmt mit der von den Begutachterinnen/Begutachtern beurteilten Arbeit überein.

Wien, November 2021 Unterschrift .....

Acknowledgements

This work was fueled by a bunch of kind people. There follows a story about coffee rings and nanowire-networks that behave like public transport systems and I could not have done it on my own. Having fun in research was my pleasure and I want to thank everybody who taught, supported and helped me to not panic. Because. Don't panic.[1] This really is my Master Thesis.

I am grateful for the environment I was offered at the Austrian Institute of Technology under supervision of Dr. Theodoros Dimopoulos. Thank you Theo for the valuable discussions and for constantly adjusting my focus. I learned a whole lot from you. I was lucky to additionally have an academic supervisor and need to express my gratitude to Prof. Dr. Christian Edtmaier, who supported me in a very straight-forward manner. I appreciate your both guidance and support.

I want to show my appreciation to all colleagues from the Energy Conversion and Hydrogen Team, managed by Dr. Stephan Abermann. I cannot mention everyone by name. But particularly, thank you Adhi for introducing me to ultrasonic spray-coating (and PhD Comics). Thank you Dani for your connections and thanks Jana, my favourite office companion, for always having my back. A sincere thank you to Stefan for the constant support in scientific terms (and for the after-lunch cantuccini) and to Selina for the updates on recent transparent electrode publications (and the discussions about bicycles). And thanks Max for the introduction to 3D-printing (and to padel-tennis). Furthermore, thanks Sophia, Jonathan and Michi from Infineon for the fun we had at my titration trainings. I truly value the friendships I found, I enjoyed research related topics as well as our kidding.

A last big thanks is expressed to my beloved ones. Most importantly my parents, who believed in me whenever I had my doubts. Thank you Mama for the enthusiasm I got from you and to Papa, for sharing this fascination for science. Another thanks goes to my siblings, to Thomas for keeping us both curious in our own fields and to Georg for making me feel safe as my emergency contact in every lab course I ever absolved. I also thank my friends. Particularly, thank you Hanni and Laura for sharing a flat during all my university years and for our simply priceless friendship.

Katharina Rauchenwald Vienna, November 2021

Nobody ever figures out what life is all about, and it doesn't matter. Explore the world. Nearly everything is really intersting if you go into it deeply enough.

Richard P. Feynman

Contents

1 Introduction

1.1 Motivation

The ultimate goal for society should be to move towards cleaner and greener technologies. To do so, multiple countries strive to reduce CO_2-emissions in compliance with the Paris Climate Agreement.[2] The agreement aims to keep the global temperature rise below 2 °C and obliges members to pursue efforts to limit global warming to a minimum. In the same spirit and from a chemist's point of view, great effort should be employed to design processing routes in the most sustainable manner possible. The twelve principles of green chemistry, as cited in the appendix, summarize guidelines towards the design of alternative, less toxic and safer processing routes with highest possible efficiency.[3]

The use of deposition techniques that do not require vacuum equipment, working at atmospheric pressure and low temperature are in this regard attractive. Ultrasonic spraying (USS) has in this regard attracted attention due to the simplicity, cost-efficiency and ease of industrial implementation.[4, 5, 6] Continuous deposition can be achieved from diverse precursor solutions, over broad surface areas and at high deposition rates. Furthermore, USS is considered environmentally friendly and satisfies the twelve rules of green chemistry. For instance, rule one, waste prevention, can be tackled by efficient spraying patterns with minimal overspray. For rule five, safer solvents and auxiliaries, it is worth to aim for water as a solvent. If organic solvent is crucially required, it is important to find the optimal dilution to minimize the total amount of organic solvent. USS can be designed as a very energy-efficient deposition technique, as it does not require vacuum conditions. Also, the optimization of other spraying parameters for low temperature processing can adress rule six, which concerns design for energy-efficiency.

The principles of green chemistry further reflect an overall strive for resource efficiency and a favouring of abundant over scarce materials. In the field of transparent electrodes (TEs), industrial technologies mostly rely on transparent conductive oxides (TCOs). A widely used representative is indium tin oxide (ITO). Big quantities of scarce indium are required to meet today's needs in touch screens, displays, and other devices that rely on ITO. Great effort is thus devoted to its substitution. Many researchers are working on alternative TEs, as for instance, based on silver nanowires (AgNWs).[7, 8] Considering the areal mass density, the required indium in ITO is much higher than the amount of required silver in AgNW-networks, per area.[9] This makes AgNWs from an environmental aspect interesting for different kind of devices as an alternative to ITO. Thirteen scarce raw materials have recently been evaluated with respect to the time left until reserves

are depleted. In this economic study, indium depletion is predicted to be significantly delayed.[10] This results from the intensified efforts to explore alternatives and indicates a general trend towards a future of decreased indium demand. This motivates the research of TEs that are based on AgNW-networks.

The optimal trade-off between electrical and optical transmittance is of highest importance in the TE-development. The balance is partly controlled by the film thickness in TCOs, while in AgNW-networks, the important parameter is the AgNW-density.[9] On one hand, the AgNW-density needs to be sufficiently high, beyond the percolating threshold, to obtain high electrical conductivity. On the other hand, it should be low enough to obtain high optical transmittance. The percolation behaviour can in a simple paradigm be compared to a public transport network, as discussed in detail later. Such networks, either of public transport or AgNWs, are supposed to maximize mobility and keep the amount of required lines minimal.

The artist Ursus Wehrli featured the Viennese subway network (figure 1.1) and broke it down to its basic components. Composite-TEs based on AgNWs could in the same way be broken down to single components. Composites are compositions of at least two materials that work together and create specific traits. The optimization of these traits in AgNW-composites should specifically optimize optical and electrical properties. The impact of single components on the network's behaviour is of interest.

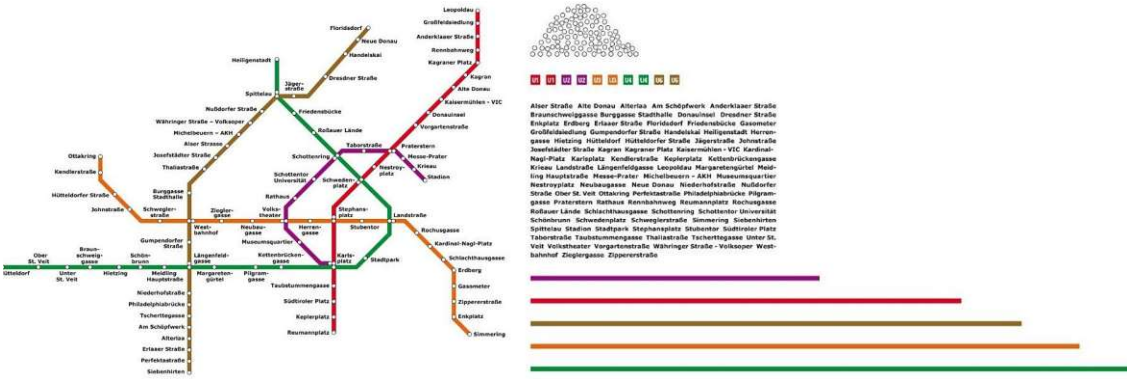

Figure 1.1: **Percolation:** AgNW networks are compared to a subway system to understand percolation theory. The artist Ursus Wehrli [11] illustrated the Viennese subway and broke it down to the constituents. This can be imagined figuratively for a composite material, which is as well composed of several components. Discussed TEs in this work are compositions of percolating AgNWs with additional materials. (illustration from "Die Kunst, aufzuräumen", Ursus Wehrli [11])

The main target of this work was to develop an up-scalable processing route for AgNW-based composite-TEs on flexible substrates by using ultrasonic spray-coating as the main deposition method. Different material combinations were explored, aiming for high conductivity and transmittance, while enhancing the environmental stability of the TEs. A

target was also to employ the developed TEs as transparent flexible heaters. Overall, the outcome should combine a low-cost, up-scalable fabrication process for TEs with high performance and functionality for the envisaged application.

1.2 Project conditions and limitations

The properties of AgNWs that are combined with metal oxide nanoparticles or conductive polymers, were studied. The processing temperature was limited to $\approx$ 100 °C to enable deposition of the layer stacks on flexible Polycarbonate (PC) substrate. The manufacturing process of choice was USS. Low temperatures and atmospheric pressure were maintained throughout manufacturing to develop a simple and low-cost process for a possible industrial-scale implementation.

1.2.1 Approach

Introduced challenges were tackled according to figure 1.2, separated in four steps.

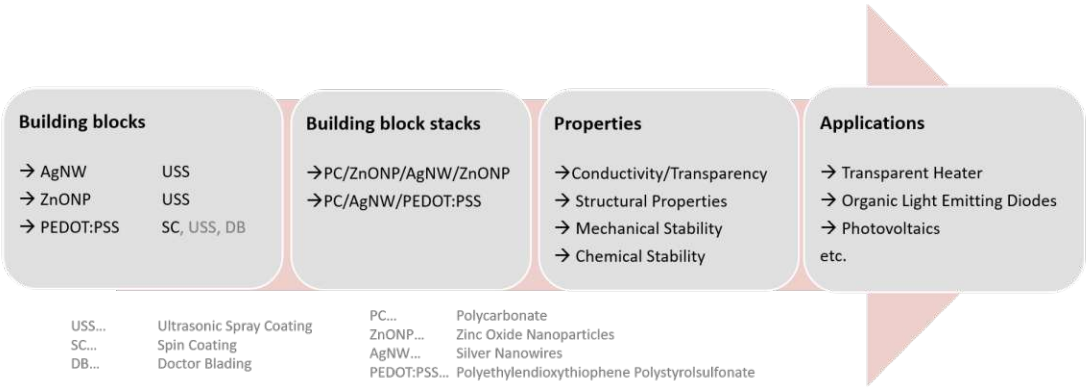

Figure 1.2: **Approach:** Development of AgNWs combined with layers of a) ZnONPs and b) PEDOT:PSS on flexible PC, processed at $\approx$ 100 °C. Samples were characterized in optical and electrical properties. Final TEs were tested as flexible THs. But results will be interesting for other TE applications.

Firstly, the optimization of the deposition parameters for all material components was of importance. Zinc oxide nanoparticles (ZnONP) and the conductive polymer Poly(3,4-ethylene dioxythiophene) polystyrene sulfonate (PEDOT:PSS) were chosen as additional building blocks to the AgNWs, due to their ease of deposition and their suitable electrical and optical properties. ZnONPs and AgNWs were deposited by means of USS, while the polymer was spin-coated at the current state of investigations. Although spin-coating cannot be scaled-up, material recipes can be transferred for USS or doctor blading (DB) deposition. The materials were stacked in two manners, namely a) AgNWs in between ZnONPs and b) AgNWs coated with PEDOT:PSS. Both composites should protect the AgNWs from oxidation and tune the optical and electrical properties of the TEs.

The two developed AgNW-based TEs are sketched in figure 1.3. Several properties are studied that include optical and electrical characteristics. Application as flexible transparent heaters (THs) should serve as a proof of concept. The set-up for testing the developed TEs as THs is sketched in figure 1.4. THs rely on resistive heating, which is linked to the Joule effect. Developed TEs could as well find use in organic light emitting diodes (OLEDs) or photovoltaics (PVs), for instance.

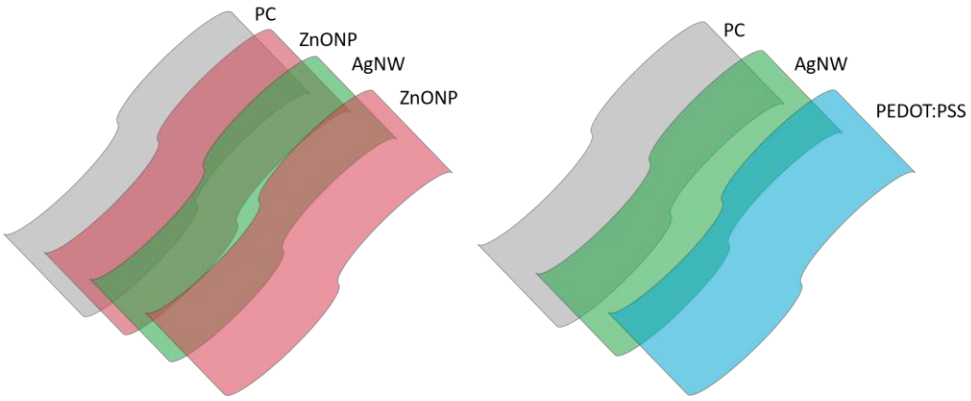

Figure 1.3: **Transparent electrode stacks:** AgNWs were stacked between ZnONPs (left) and coated with PEDOT:PSS (right). These represent two approaches for protected AgNW-networks on PC, processed at low temperature and from solution.

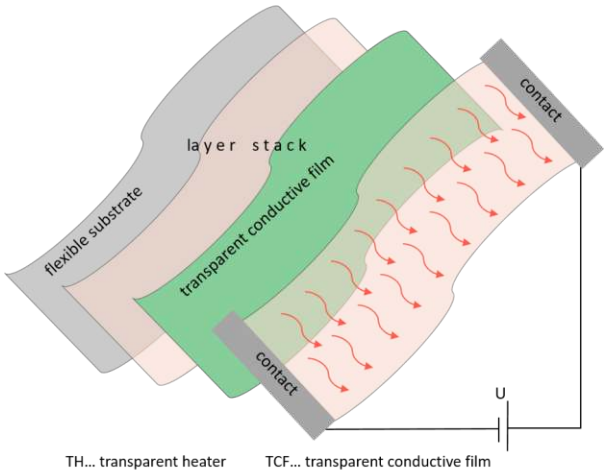

Figure 1.4: **Transparent flexible heater:** Stacks of embedded AgNWs should be tested in a TH set-up, as schematically depicted. This is exemplary for possible TE applications. Voltage is applied via two contacts, which induces resistive heating as a result of the Joule effect.

1.2.2 Methodology

Deposition by USS was the most applied and thoroughly studied method in this work. To keep the processing as simple as possible, pre-treatment of the substrate or post-treatment of the thin films were avoided. The obtained samples were characterized by sheet resistance (R_s) and transmittance measurements in the UV, VIS and IR range. Normal transmittance (T_{normal}) and total transmittance (T_{total}) were measured to determine the amount of diffuse light, known as haze. With the help of scanning electron microscopy (SEM), information about the morphology of the thin films was acquired. SEM observations could be linked to single spraying parameters, offering a way to optimize process variants step by step. Further, SEM images offer a possibility to extract quantitative values for the AgNW density by introducing the value of the AgNW surface fraction (ϕ_s), which is the relative area covered by AgNWs. This is an important value for evaluating and comparing properties of AgNW-networks. For that purpose, the image processing software ImageJ was used. In a next step, percolation models were applied on experimental data of the embedded AgNW networks. Other available characterization methods were used, which included energy dispersive X-Ray spectroscopy (EDX) and profilometry. The stability of AgNWs was investigated through storage at elevated temperature conditions for a prolonged duration. Finally, the samples were tested as flexible transparent heaters. Different bias was applied between contacts and the resulting surface temperature was monitored.

1.2.3 Outline of the thesis

This Master thesis is organized as follows. Chapter 2 'Theoretical background' lays down the relevant literature and gives theoretical background on important aspects for this work, which regard flexible substrates, ultrasonic spray-coating, transparent conductive materials in general and AgNWs in specific. Percolation theory, as well as the principles of transparent heaters are explained. Chapter 3 'Materials and methods' describes the experimental work and gives an overview of the applied deposition techniques and characterization methods. The next chapter 4 'Results and discussion' concerns the detailed analysis and discussion of the obtained experimental data. The final conclusions are drawn in chapter 5 'Conclusions'. The thesis ends with a short outlook towards possible future research in chapter 6 'Outlook'.

2 Theoretical background

2.1 Flexible substrates

For a smooth transition from lab-scale research to large-scale production, industry aims for continuous roll-to-roll (R2R) manufacturing instead of batchwise production.[12] R2R means, that all depositions and treatments for the final product are applied between two rolls, the infeed and the outfeed. Flexible substrates are required for the rolled-up product. But apart from manufacturing reasons, flexible substrates have attracted interest because the show advantages when compared to rigid substrates. Reduced weight, cost-efficiency, storage in rolled-up form, the convenience in applications and ease of integration in curved or wearable devices are convincing factors. Hence, big effort is put into enabling depositions of various materials on flexible substrates for electronics.[13] But a recurring drawback in manufacturing is the heat sensitivity, due to the organic nature of flexible polymer substrates.

In table 2.1 properties of common flexible substrates are qualitatively compared.[14] Attention should be devoted to comparing PC to other conventional polymers, but the results of developed TEs on PC could be easily transferred to PET, PEN or others.

Table 2.1: **Qualitative properties of common flexible substrates:** Observational comparison of flexible polymer substrates, based on a review by Dhanabalan et al.[14]. The ranking follows excellent - good - fair - poor.

	optical clarity	**operating temperature**	**dimensional stability**	**surface roughness**	**solvent resistance**	**moisture absorption**
PC	excellent	fair	fair	good	poor	fair
PET	good	fair	good	poor	good	good
PEN	good	good	good	poor	good	good
PES	good	good	fair	good	poor	poor
PI	poor	excellent	good	good	good	poor

PC = Polycarbonate PEN = Polyethylene naphtalate PI = Polyimide
PET = Polyethylene terephtalate PES = Polyethylene sulfonate

PC is tempting in terms of optical clarity, but suffers from limitations in the operating temperature. The temperature is limited by the T_g value, which indicates the point, where polymeric chains start to move and cause the material to deform. The T_g of PC is around 145°C.[15] PI for instance exhibits a T_g up to 400°C [16], due to stiffer chains. Manufacturing conditions for processing PC should not exceed a threshold of 100 °C to prevent product deformation when T approaches T_g.

2.2 Ultrasonic spray coating

Ultrasonic spraying (USS) is an interesting technique, as it is easy to upscale and mostly working at ambient conditions. It is compatible with R2R and beneficial for sustainability as well as for economic reasons. Further scalability can be obtained by multi-jet and multi-nozzle modes, as applied in industry. It is distinguished between spray-pyrolysis and spray-coating. Spray-pyrolysis includes a reaction. In spray-coating, heating can be applied to evaporate solvent, but no reaction occurs for film formation.[17] Literature is often focussing on spray-pyrolysis. But knowledge from spray-pyrolysis can be transferred to spray-coating of nanostructures, when keeping the basic difference in mind. The set-up and parameters are similar, but deposition mechanisms are obviously different.

The ultrasonic nozzle is the center-piece of an ultrasonic spray-coater. The nozzle forms a spraying cone of tiny droplets by using ultrasonic energy, it vibrates at a specific frequency and a standing wave is formed. When the nozzle power is high enough, the amplitude of this standing wave is increased until the peaks break off and tiny droplets are formed. The droplet size can be estimated with equations based on Lang equation (equation 2.1).[18] Additional dependencies on the nozzle geometry and the solvent viscosity, flow rate and the amplitude of ultrasonic vibrations were introduced by others in literature.[19] The latter are linked to critical values, above these becomes the influence of the parameters significant. But Lang equation gives a good approximation of the droplet diameter from ultrasonic nozzles, which is mainly dependent on the frequency, the surface tension and the density of the solvent.

$$d = 0.34\left(\frac{8\pi\sigma}{\rho f^2}\right)^{1/3} \quad [18] \tag{2.1}$$

d... droplet diameter f... frequency σ... surface tension ρ... solvent density

In figure 2.1 a scheme of USS is depicted. An ultrasonic spray-coater is equipped with a supply that feeds the ultrasonic nozzle. The stream is directed towards the substrate by a stream of pressurized gas, the so-called shaping air. The droplets decrease in their diameter during their flight, due to solvent evaporation. The droplet size determines the interaction of the material with the substrate. They either hit the surface as droplet, agglomerate or precipitate, as vapour or very dry powder. As indicated to the right in figure 2.1, either the I) substrate temperature or the II) initial droplet size decide over

the solvent content and final droplet size at the moment of deposition. But the final droplet size is further dependent on the flow rate and shaping air pressure. Furthermore, the nozzle to substrate distance and the droplet velocity influence the final droplet size and film formation. Hence, a whole set of interacting parameters control homogeneity, morphology and the general properties of the deposited thin film from USS.

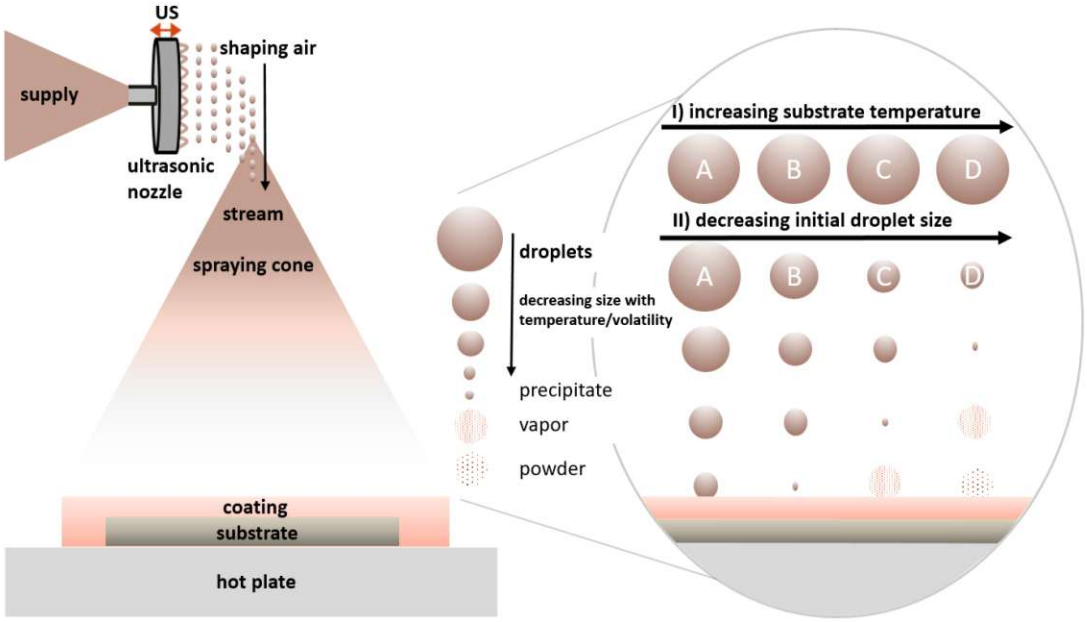

Figure 2.1: **Spray-coating:** USS and evaporation processes are sketched. Droplets are generated at an ultrasonic nozzle. The right side shows that droplets of either I) constant size but increasing temperature or II) decreasing initial droplet size at constant temperature determine the final droplet size, when solvent is evaporating during the flight towards the substrate. (modified from Filipovic et al. [4])

Sprayed droplets are exposed to turbulences induced by the shaping air, solvent evaporation and repulsion from the heated substrate. Following four main forces determine the trajectory and evaporation kinetics of droplets in spraying techniques.[20]

a) Gravitation b) Thermophoretic forces c) Stokes forces d) Electric forces

Gravitation pulls droplets downwards, which depends on the droplet mass. When droplets approach the heated surface, velocity decreases along a thermal gradient. This is due to a thermophoretic force, which pushes droplets away from the heated surface. The droplets experience another retarding force, due to the air resistance, the so-called Stokes force. In spraying-techniques like spray-pyrolysis or electrospraying, when ions are involved in the deposition mechanism, electric forces add up to a total of the four main forces.[20, 4] The interplay of these forces is not trivial.

A strive for deposition of solid particles from gas phase is often discussed in literature.[4, 17] This case is sketched to the very right in figure 2.1, as obtained from either high surface temperature or small initial droplets. But it is a matter of discussion if it is beneficial to evaporate all solvent prior to thin film formation.[20] In spray-coating, deposition from wet and stationary droplets can be desired. Wet droplets undergo splashing and/or form stationary droplets. Droplets can dissipate energy by splashing on the substrate. Stationary droplets are formed for a certain amount of time, while solvent evaporates. A stationary droplet can either result from lower substrate temperature or bigger initial droplet size. Spreading of slightly wet droplets of optimal droplet size, velocity, impact and wetting can contribute more to the film deposition in spray coating than dry powder deposited from gas.

The initial droplet size is of microscale importance, but the shape of the spraying cone further affects the coating in a macroscale manner. Perednis et al. [20] showed that droplets concentrate within a narrow angle, centered within the spraying cone from an air blast atomizer. In figure 2.2 their idea of the spraying cone and the vapour vent is depicted. The vent partly directs the stream away from the center and out of reach for film deposition. They discuss that it is difficult to estimate the exact impact of certain forces on the vent. But the spraying cone might be deformed and can cause material loss to the vent, which is interesting when discussing material loss within the spraying chamber and to the overspray. The fraction of coating that is not deposited on the substrate but on surroundings is called overspray. A certain amount of overspray is taken into account to guarantee, that the substrate faces the same interaction with the center of the spraying cone to achieve homogeneous coverage.

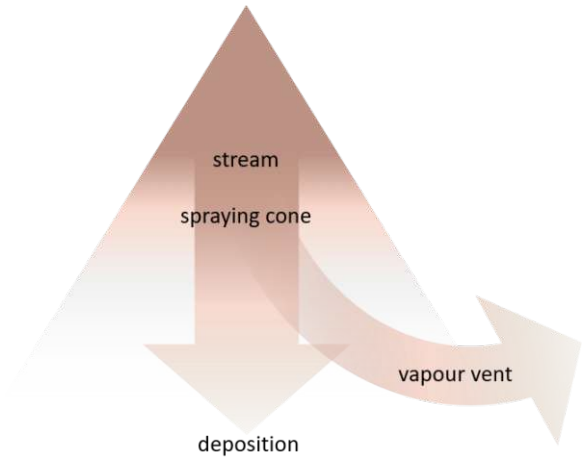

Figure 2.2: **Spraying cone:** The aerosol transport within the spraying cone can be separated into a centered direct stream and the vent. The centered stream carries the main part of material to deposit. A fraction of the stream is changed in trajectory and lost to the vent. (modified from Perednis et al. [20])

An optimized recipe is thus required to assure that the whole substrate area faces the same interaction with the center of the spraying cone. Several parameters need to be studied, which depend on the specific material. Well considered process-parameters make it possible to avoid inhomogeneous coverage and control the interactions during the film formation.

2.2.1 Process and parameters

The USS-process implicates the following parameters, as summarized in table 2.2. Well considered spray-parameters determine droplet size, velocity, droplet impact, residence time of droplets on the substrate and the evaporation kinetics. The parameters interact with each other and significantly affect the final thin film properties. Detailed discussion of the influence of single parameters on the outcome of sprayed nanowires and nanoparticles follow in chapter 4.

Table 2.2: **Parameters for ultrasonic spray-coating of nanostructures:** USS parameters are listed and explained. The final outcome of sprayed nanostructured thin films is determined by setting optimal parameters.

Substrate temperature	- hot-plate temperature, where samples are positioned
Suspension composition	- choice of solvent and possible additives
Suspension dilution	- solid content of nanostructures dispersed in the solvent
Nozzle power	- power causing the nozzle to vibrate to induce nebulization
Flow rate	- volume of suspension per unit of time that is nebulized
Shaping air	- air stream pressure that directs the stream to the substrate
Spraying pattern	- shape of lines drawn by the moving nozzle
Spacing	- distance in between sprayed lines
Spraying speed	- velocity of the nozzle movement
Sample position	- position in the chamber within the spraying area
Overspray	- excess material deposited beyond the targeted area
Scan number	- number of layered spraying repetitions to build the film

2.2.2 Coffee ring effect

A recurring issue in terms of depositions from solution or suspensions is the so-called coffee ring effect. Ring-like structures can occur in thin films deposited from solution. These were first called 'coffee rings' by Yunker et al. in 2011 [21], because microscope images resemble dried drops of coffee. It results from the drying process, where a capillary flow forces particles to suspend along the narrow edges of the initial droplets.[22] The effect is schematically depicted in figure 2.3, where directions of the capillary flow to the narrow edges, the contact lines, are indicated with arrows. The morphology of the rings is studied thoroughly in literature and was reported to be affected, for instance, by the particle shape [21], external forces like acoustic fields [23] or alternating frequencies [24]. Due to complex fluid dynamics, several coffee ring patterns are possible.[25, 26]

The wetting is often discussed in regards to coffee rings.[27] The wetting behaviour is quantified by the contact angle [28] and determines the position and length of the three phase contact line at the interface of suspension, substrate and atmosphere at the droplet edges. This contact line is indicated in figure 2.3 for different wetting cases. The wetting significantly affects the final pattern and morphology of coffee rings.[27, 29] It is reported that hydrophobic surfaces and poor wetting help to avoid coffee rings.[30]

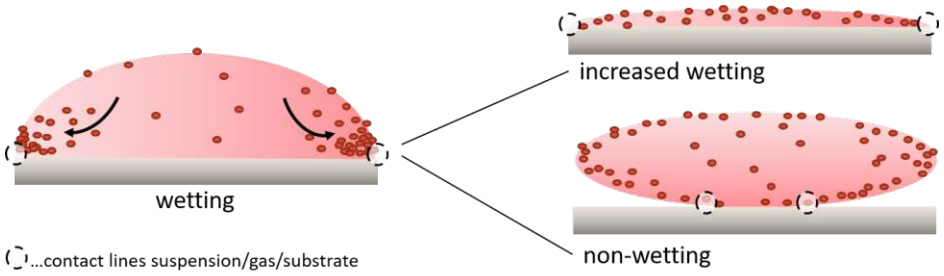

Figure 2.3: **Coffee ring effect:** Suspended nanoparticles within a sessile droplet can cause ring-shaped solid stains, similar to dried drops of coffee.[22, 21] Rings mark former contact lines of suspension, substrate and atmosphere. Kinetics of the particle diffusion to droplet edges are controlled by several parameters, including the wetting.[31]

Furthermore, the process is diffusion controlled and highly time-dependent.[32] The residence time of droplets on the substrate is thus important. For instance, when the drying process is faster, fractions of nanostructures diffuse to gradually shrinking droplet edges. The droplet is decreasing in diameter and so are the rings. This results in several coffee rings within the initial droplet size, which is referred to as inner coffee ring deposits (ICRDs).[33] The ICRDs are linked to later pinning of contact lines as a result of evaporation kinetics.

Such stepwise pinning of contact lines is sketched in figure 2.4. A balance between static and dynamic friction inhibits a smooth motion. Contact lines pin at decreasing diameters in a stick-slip mechanism.[34, 25]

Static friction needs to be exceeded, otherwise, the droplet sticks. The droplet decreases in curvature, before the contact line is shifted. The droplet then slips to a new equilibrium position. It sticks until it again slips. When the stick phases are longer than diffusion time, particles diffuse to the shrinking droplet's edges.

stick: particles diffuse to contact lines, solvent evaporates and curvature decreases
slip: static friction is overcome and diameter decreases until the contact line pins

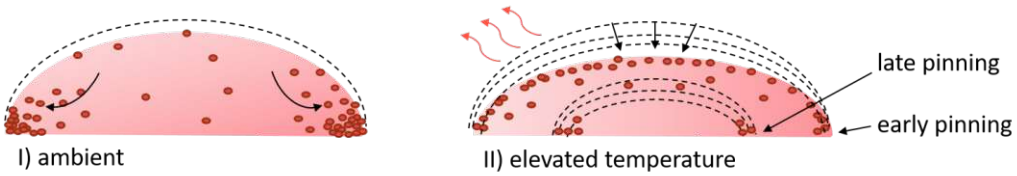

Figure 2.4: **Inner coffee ring deposits:** Elevated substrate temperature avoids I) single coffee rings but causes II) ICRDs. This is argued to come from diffusion kinetics and stepwise sticking and slipping of contact lines during droplet shrinkage.[33]

Coffee rings are usually not desired. They can cause inhomogeneities and disturbed morphology and this influences the surface roughness of deposits from solution. Researchers have reported methods to circumvent or minimize this effect. Mampallil et al. [31] summarized ways to suppress coffee rings by three strategies.

I) prevent pinning of contact lines
II) hinder particles to be transported to contact lines
III) disturb the capillary flow

The influence of the speed of evaporation is discussed in literature, which affects the stationarity of pinned contact lines.[33] If the droplet shrinkage rate is lower than the particle diffusion rate, particles have time to be transported to the edges.[32] Fluid dynamics and particle diffusion are affected by temperature gradients and controlled temperature treatment is therefore important.[35] The coffee ring effect is also dependent on the size and shape of the nanostructures.[6] This can be attributed to a reduced capillary flow. Fleury and coworkers [6] progressively decreased coffee rings with non-stable, agglomerated colloids and obtained better homogeneity in sprayed thin films of nanoparticles. Yunker et al. [21] similarly showed suppression of ring formation with ellipsoidal particles. Movement of particles to the edges of shrinking droplets is in summary suppressed by fast solvent evaporation, elongated nanoparticle shapes, increased nanoparticle size and well considered thermal treatment.

2.3 State of the art transparent conductive materials

Transparent conductive materials (TCMs) represent a broad class of materials that combine high electrical conductivity and maximal optical transparency. This property combination was first reported by Karl Bädeker in 1907 for Cadmium Oxide.[36] A lot of effort has been devoted to the development of materials of this kind. Nowadays, they are required in a wide range of applications and known under the term of transparent electrodes (TEs). To maintain transparency while sufficient conductivity is provided is a challenging matter of modern engineering.

A common benchmark for TEs was introduced by Haacke [37] who proposed a figure of merit (FOM) in 1976. Although other FOMs exist, depending on the field of application, Haacke's FOM remains widely used (equation 2.2). This value is desired to be high and can act as a ranking of TEs. High FOM_{Haacke} values represent good transparent electrode performance.

$$FOM_{Haacke} = \frac{T^{10}}{R_s} \quad [37] \tag{2.2}$$

Sophisticated nanomaterials were developed as TCMs. For instance, for application in organic light-emitting devices [38], for photovoltaics [39] or for flexible transparent heaters [40, 41, 42]. Established TCMs can basically be divided into three groups - transparent conductive oxides, organics and metals.

2.3.1 Transparent conductive oxides

Since Bädeker [36] launched CdO, development focussed on other transparent conductive oxides (TCOs). Particularly, SnO_2 marked a breakthrough for heated airplane cockpit windows, as patented in 1947.[43] In 1970s, indium oxide began to rise and tin doped indium oxide ($In_2O_3 : SnO_2$) still sets the market standard for TCMs.[44] But indium is scarce, the supply heavily controlled and research is striving for alternatives.

The balance of high optical transmittance and low resistance is tackled in TCOs by thoughtful energy band structure engineering. TCOs are n-type doped semiconductors with wide bandgaps of 2.5 - 5 eV.[45] Common TCOs are often based on In_2O_3, SnO_2, ZnO and TiO_2.[46, 44] The conductivity of the TCO is dependent on the composition and microstructural characteristics, such as the particle size, the defect concentration, the density, the morphology and the distribution of phases. Undoped ZnO for instance, can be processed as conductive thin films, but for that purpose the layer needs to be thick and dense enough and depositions usually require higher temperatures to control the growth of the layer.[47]

The conductivity of TCOs can be significantly enhanced by intentional doping, which is widely applied and leads to a long list of different reported TCOs.[48] Heavily doped ZnO with In [49, 50] Ga [51] or Al [52] (IZO, GZO or AZO) are for instance promising candidates, as well as commercially available flourine doped tin oxide (FTO).[53]

2.3.2 Organic conductive materials

At the beginning of 21st century, organic conductive materials attracted attention. They represent an important field of research, as honored with Nobel Prizes [54, 55] in short time intervals. For flexible applications, the brittleness of oxides is unfavourable and organic TCMs can meet requirements for flexible devices in a more straight-forward manner. Also, they are usually cheap and solution-processable. The field of organic TCMs can further be separated into organic nanostructures and conductive polymers.

2.3.2.1 Carbon-based nanostructures

The quick rise of graphene, since the discovery in 2004 and as awarded with a Nobel Prize in 2010 [54], shows that carbon-based nanostructures exhibit high potential for modern applications on basis of the very abundant material carbon. Graphene is a single hexagonal layer of graphite, first studied in 1947.[56] Apart from graphene, 2D layers of carbon in rolled up form have also attracted attention under the term of carbon nanotubes (CNTs).[57] These allotropes of carbon contain numerous double bonds, to which their high electrical conductivity is attributed. Gaps in deposited networks and the very low thickness allow light to pass and cause optical transmittance on top of conductivity. Thin films of graphene and CNTs are as well suitable candidates for replacing ITO.[57, 58, 59]

2.3.2.2 Conductive polymers

Another sensation was the idea to apply doping mechanisms, as known from semiconductors, to polymers. The doping mechanisms are obviously different, but the principle of incorporating very small amounts of certain species to largely increase the conductivity. is similar. Doping of polymers refers to a partial oxidation or reduction of the polymer to delocalize electrons. The work on conductive polymers was awarded with the Nobel Prize in 2000, which innovated polymer chemistry and electronic industry.[55] In early stages, a lot of work was devoted to the improvement of processibility and stability of conductive polymers.[60] Research started with Polyacetylene.[55] Nowadays, Polyaniline (PANI) and Poly(3,4-ethylene dioxithiophene) (PEDOT) are common. They have in common, that they exhibit conjugated backbone chains of alternating double and single bonds.

PEDOT is mostly combined with poly(4-styrenesulfonate) (PSS), which makes it stable in aqueous dispersion and allows application on an industrial scale from aqueous

solution.[61] As depicted in figure 2.5, the structure PEDOT:PSS can be described hierarchically by primary, secondary, terniary and quarternary structures.[62] Understanding the structure makes the properties of conductive polymers comprehensible.

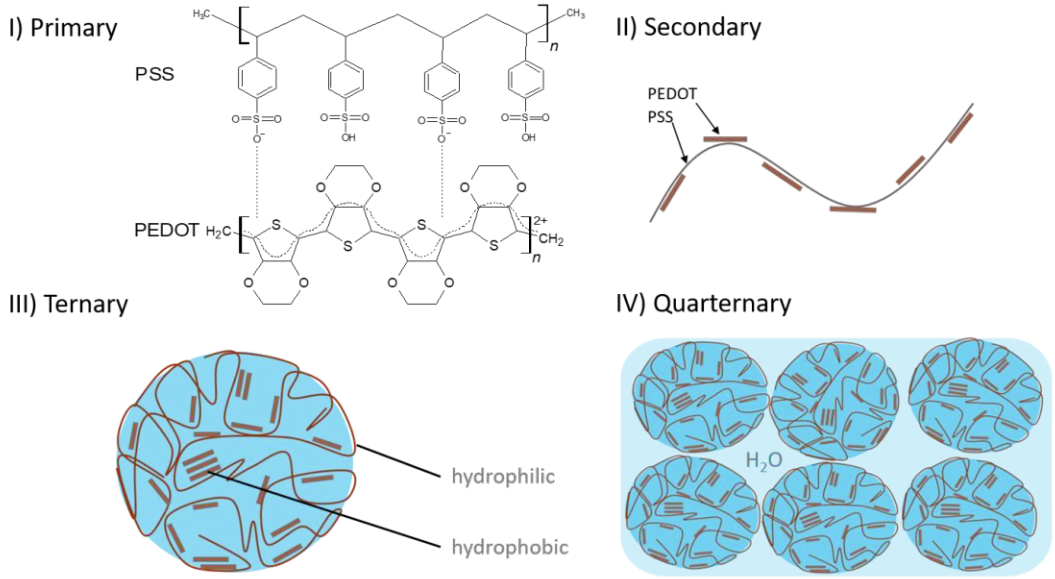

Figure 2.5: **Structure of PEDOT:PSS:** Shown are hierarchic structures. Due to electrostatic interaction, hydrophobic PEDOT attaches to hydrophilic PSS. A water soluble gel is formed. PEDOT (brown) is conductive if packed and well segregated from PSS. (modified from Mochizuki [63] and Horii et al. [62])

The primary structure shows the monomer units. PEDOT and PSS form a polyionic complex. But the conductivity of the complex is linked to PEDOT, a fully conjugated and rather stiff polymer, where electrons can move freely along the backbone of delocalized π-orbitals. PEDOT:PSS is formed from electrostatic interactions.[64] Rigid PEDOT-fractions tend to stick to flexible PSS-chains, as shown in the secondary structure. The water solubility of PEDOT:PSS can be explained by the ternary structure. PEDOT aggregates and induces the formation of colloidal gel particles of hydrophobic PEDOT-cores and hydrophilic PSS-shells. These particles are suspendible in water, as sketched in the quarternary structure.[63]

The conductivity of PEDOT can further be explained with figure 2.6. PEDOT has a stiff and mostly aromatic structure, stacks of PEDOT can thus be represented as layered sheets.[65] Conductive PEDOT forms a separate phase from PSS. Basically, three charge-transport processes are possible between these lamellaes in the solid state. Charge transport is possible a) intrachain, b) interchain or c) interlamellar. Conductivity is decreasing from a-c, intrachain to interlamellar. The intrachain transport along the backbone is contributing most to the conductivity.[66, 65]

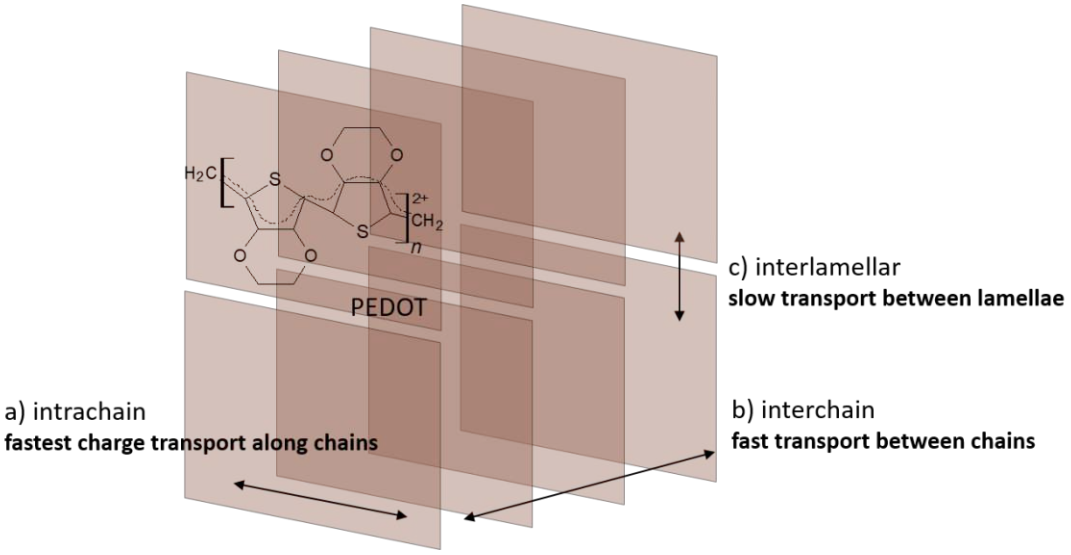

Figure 2.6: **Lamellar π-π-stacking in PEDOT:** Three conduction paths are available in stacked PEDOT lamellas. a) Intrachain contributes most to the conductivity. b) Interchain, or face-to-face transport is improved by dense packing. c) Interlamellar has a small contribution. Any measures improving the stacking, crystallinity and phase segregation of PEDOT from PSS enhances the conductivity of the conductive polymer. (modified from Gueye et al. [65])

There are possibilities to enhance the conductivity of PEDOT:PSS. Most of them can be ascribed to two effects. But exact mechanisms are a subject of debate.[67]

I) improved packing density of π-π-stacked PEDOT
II) improved phase separation of PEDOT from PSS

There is a lot of literature dealing with understanding the conductivity of free-standing PEDOT:PSS films.[67, 68, 65] The most prominent attempt for PEDOT:PSS conductivity enhancement is doping with high boiling point solvents like Dimethylsulfoxide (DMSO) or Ethyleneglycol (EG).[69, 70] This is said to decrease the PEDOT:PSS water solubility, leading to better phase separation between PEDOT and PSS. This is increasing the interactions between PEDOT-sheets and thus increases the conductivity.[70] Another effective approach is pH-optimization. Acidic pH is reported to successfully decrease the sheet resistance.[63] Acidity also improves the phase separation of PEDOT from PSS in free standing PEDOT:PSS.

2.3.3 Metallic conductive nanostructures

In terms of electrical properties, it is hard for ceramics or organic materials to compete with electron conductors like metals. Metals, on the contrary to insulators and semiconductors, have huge densities of free electrons and exhibit high electron mobility.[71]

But in metals, the fraction of light not reflected from the surface, is absorbed by the electron gas and the lattice. Sophisticated engineering is thus required to limit optical losses, while electrical conductivity is maintained. Consuming a very low quantity of raw material is key, when striving for metal-based TEs. This challenge can be tackled by either I) ultrathin layers of metal or by II) metallic nanostructures like nanowires. Both attempts require modern engineering and controlled deposition.

2.3.3.1 Metallic thin films

Very thin metallic films, sandwiched between dielectric layers in dielectric-metal-dielectric (DMD) stacks can meet TE requirements.[72, 73] Through this architecture, reflection losses are minimized by destructive interference at the different interfaces. The thin layers of metal have thicknesses down to 6 nm.[72] A certain critical thickness needs to be exceeded to provide a continuous conductive film, the thin film deposition must therefore be well controlled. The metal film can be formed in an island growth mode, which affects the minimal thickness. The island films can be desired or not.[74]

Coinage metals are common metals in DMDs, as they possess low optical loss and high conductivities. Silver is dominating the field of metallic conductive materials due to the highest known electrical conductivity of bulk Ag among metals.[75] But the implementation of other metals like Cu [76, 77] or Au [78, 79] instead of Ag, are also reported in DMDs as well as in nanowire-based TEs.

2.3.3.2 Metallic nanowires

The most prominent metal nanostructures are silver nanowires (AgNWs). When deposited as a random network of sufficient density, the network provides electric percolation paths, while free gaps still allow light to be transmitted.[80, 7]

Synthesis of such nanostructures is sophisticated. But since polyol reduction was introduced in 2002 [81], AgNWs attracted particular attention. Directional growth can be induced by a variety of methods, for instance hydrothermal reaction [82] or electrodeposition [83]. But polyol reduction is most common and commercially applied. The challenge in synthesis is to control the length (L) and diameter (D), which are included in the value of the aspect ratio (AR=L/D). The effect of the AR on properties of AgNW-TEs is studied and modelled and studied extensively in literature.[84, 85] Synthesis is thus expected to guarantee narrow L- and D-distribution for reliable AR-distributions and reproducibility of targeted properties in the final TEs.

The fabrication of AgNWs by polyol reduction is using a polyol (usually Ethylene glycol) as reductant of a metal precursor (usually $AgNO_3$), in the presence of a capping agent (usually Polyvinylpyrrolidone, PVP).[81] This causes an anisotropic confinement and induces growth in one dimension. The basic principle of this synthesis route is depicted in figure 2.7. PVP passivates (100) sides and exposes lower energy (111) sides as

abundant seeds for Ag deposition. PVP was originally only used to prevent aggregation, as it is a common surfactant. But it was shown to be crucial.[86, 87] PVP exhibits carboxyl groups that preferably attach to (100) sides via Ag-O coordination, as sketched with red dashed lines in figure 2.7 below. Conformational reasons thus explain the role of PVP in the unidirectional growth.[88]

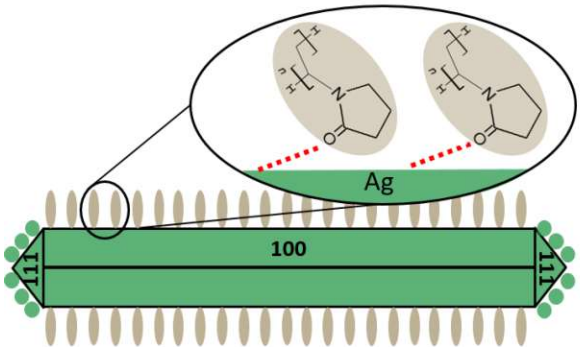

Figure 2.7: **AgNW synthesis via polyol reduction:** Shown is the role of PVP in the directional growth of AgNWs from reducing $AgNO_3$ with ethylene glycol. PVP passivates (100) and leaves (111) free for Ag deposition, which induces the 1D-growth.[81, 86]

The precise control of AgNW-synthesis, mostly through PVP concentration, gives rise to commercially available AgNWs of narrow L- and D-distributions.[89] This is important to predict and control optical and electrical properties of percolating AgNW-networks.[84]

2.4 Percolation theory

It is crucial to obtain percolating behaviour, when working with AgNW-networks. Percolation concepts describe abrupt transition changes, caused by the formation of long-range networks. Percolating networks describe interaction patterns in complex systems as applied in physics, biology and sociology or also, to understand epidemic spreading.[90, 91]

2.4.1 Principles of percolating networks

In terms of AgNW-networks, the system changes from non-conductive to conductive when entering the percolating regime by exceeding a critical AgNW-density.[90] To explain the concept of percolating networks in simple terms, an efficiently working public transport system is hereinafter discussed as a functional analogue. Figure 2.8 shows the Viennese subway network growth from a) 1982 - d) 2030. A construction of subway lines of optimal length and spatial distribution allows public transport in a fast and convenient manner, which is linked to high mobility. But a wholly interconnected network that covers broad areas is required.

Figure 2.8 shows interesting features of percolating systems, as the development of the Viennese subway system has a positive impact on the personal mobility.

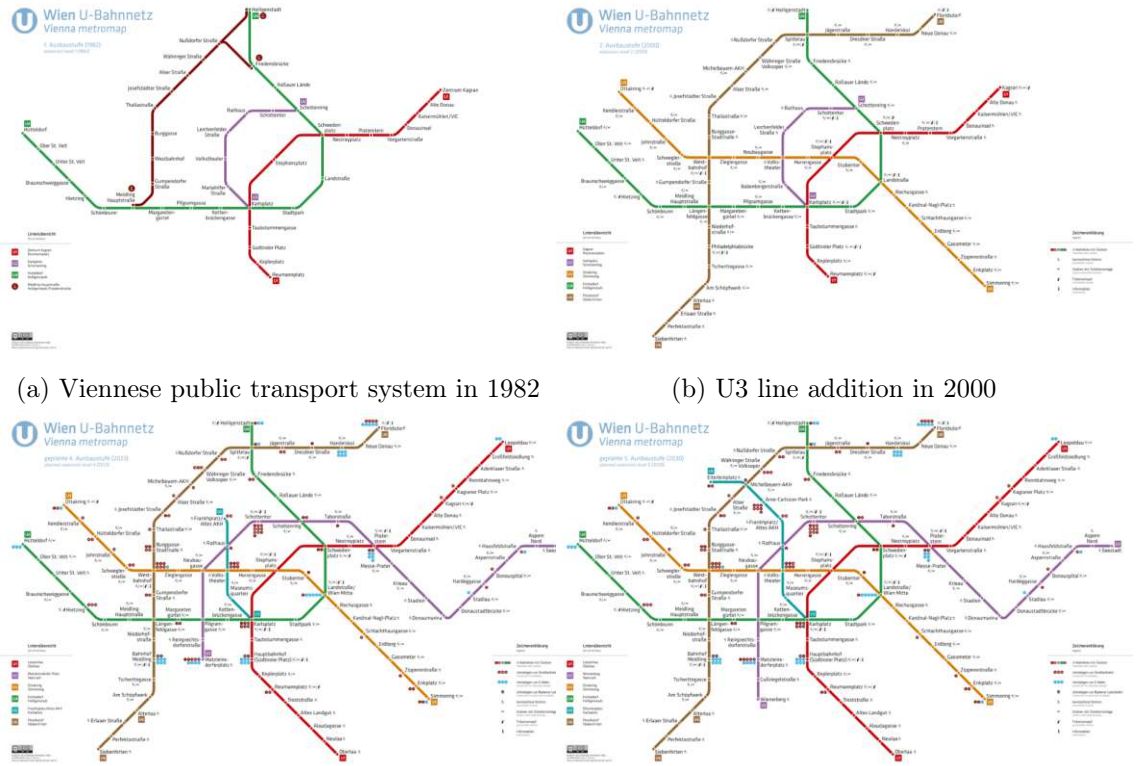

(a) Viennese public transport system in 1982

(b) U3 line addition in 2000

(c) U5 line addition as planned until 2023

(d) Further planned line expansions until 2030

Figure 2.8: **Viennese subway system, a percolating network:** Public transport systems affect the mobility, which is comparable to electron-mobility in percolating AgNW-networks. a) A working subway system in 1982 is built on four lines. b) Addition of U3 (orange) in 2000 increased mobility significantly, additional lines improve mobility. c) But planned U5 (turquoise) will not contribute as much as U3 did. As soon as a critical number of lines is by far exceeded, additional lines contribute less to the overall mobility. c-d) Expansions of lines also increase mobility, but to a lower extent than the line-density. (graphs https://www.u-wien.at/ausbaustufen)

In 1982 the network started to cover the most important spots and a critical density was exceeded, the network started to work. Using public transport was suddenly an effective way of transport in the city. When U6 (brown) was expanded and U3 (orange) was added in 2000, the perceived mobility increased significantly. When further lines were added, more benefits were gained. U5 (turquoise) will, as supposedly finished until 2030, further improve mobility. But addition of U5 will not have an impact as high as the addition of U3 back then. The contribution of one line to the overall mobility is not as high anymore. The expansion of lines also positively affects the network-quality, it reduces the required number of junctions for changing lines. But the highest impact has the addition

of new lines in early stages of the network-formation. One can conclude, that addition of single lines has a higher impact on the overall network-mobility, if the line density is low. If the line density is high already, additional lines improve mobility, but to a lower extent. Hence, mobility contribution of additional lines is decreasing with increasing line density.

Insights gained from this example suggest some effects that can be linked to AgNW networks. The line-density (AgNW-density) determines the mobility (electrical conductivity or resistance). The speed and quality of the lines themselves are important for the efficiency of the network (wire resistance). Also the length of the lines has an important impact, as it influences the required number of changing possibilities. The efficiency of changing between lines can be rate-determining, such as one tries to avoid changing the lines in subways (junction resistance). But the premise for these assumptions is that the network exhibits a random and sufficient distribution of lines and junctions. And it needs to exceed a minimal density to actually percolate (critical AgNW-density). Otherwise, the network breaks down.

2.4.2 Dependence of electrical properties on the AgNW-density

Percolating networks exhibit critical values and show sudden changes in properties when these values are approached. For AgNW-networks close to their percolation threshold, the conductivity as a function of the AgNW-density, AgNW-length, the device-width or also the AgNW-alignment-angle can be described with power laws.[93] Several groups have worked on analytical [84, 94, 95, 96] and computational [93, 85, 97] models to describe the electrical properties of sparse AgNW-networks. The aim of these percolation models is to describe the sheet resistance (R_s) as a function of AgNW-density (ϕ_s), while the wire- (R_w) and junction-resistance (R_j) are accordingly considered.

$$R_{network} \quad \approx \quad R_s \quad \approx \quad f\ (\phi_s,\ R_w,\ R_j) \tag{2.3}$$

$R_{network}$		$\rightarrow$ network-resistance, given by the measured sheet resistance (R_{sheet}, R_s)
$\phi_{surface}$	ϕ_s	$\rightarrow$ AgNW-density, biggest impact on R_s
R_{wire}	R_w	$\rightarrow$ wire-resistance, depends on the wire material
$R_{junction}$	R_j	$\rightarrow$ junction-resistance, depends on junction-quality and network-connectivity

The AgNW-density can be quantified differently. It can be represented by the number of wires [96] or the number of junctions.[85, 98] But these numbers do not consider distributions of AgNW-lengths and -diameters from synthesis, which causes an error in modelling.[84] Alternatively, AgNW-density can also be quantified by an areal mass density of Ag [94] or an areal surface fraction.[84] The AgNW surface fraction can be extracted from optical transmission measurements [84] or from image processing as a fraction of pixels.[92] In this work, the AgNW-density is extracted from SEM images as the surface area fraction that is covered with AgNWs, as referred to with ϕ_s.

The R_s as a function of ϕ_s describes important electrical characteristics of percolating AgNW-networks. The power law shown in equation 2.4 introduces theoretical values, namely the critical density ϕ_c, the critical exponent t and the proportionality factor M. The values are explained in detail below and will be further discussed in chapter 4, when percolation modelling is applied to own experimental data.

$$\mathbf{R_s} = \frac{\mathbf{M}}{(\phi_\mathbf{s} - \phi_\mathbf{c})^\mathbf{t}} \quad [84] \tag{2.4}$$

ϕ_s	$=\frac{\varphi_{Ag}}{\varphi_{total}}$	[ ]	= silver nanowire surface fraction → experimental value
R_s		$[\frac{\Omega}{sq}]$	= sheet resistance of the network → experimental value
ϕ_c		[ ]	= critical AgNW surface fraction minimal ϕ_s that is required for an interconnected network
M		[ ]	= material factor proportionality factor which is indipendent from ϕ_s
t		[ ]	= critical exponent deviation from linearity in $\frac{1}{R_s}(\phi_s)$

2.4.2.1 Critical AgNW surface fraction (ϕ_c)

The critical AgNW surface fraction (ϕ_c) defines the percolation threshold. Figure 2.9 shows three regimes in relation to the position of ϕ_c. Below ϕ_c, clusters are not connected. As soon as $\phi_s > \phi_c$, the network starts to work as a network, AgNWs are connected and build a conductive backbone. This backbone can carry a current over broad areas and causes R_s to decrease drastically when ϕ_s exceeds ϕ_c. When $\phi_s >> \phi_c$, the system approaches bulk metal properties.The network properties are sensitive within the percolating regime and small changes in wire- and junction-resistance have a relatively big impact. It is the percolating regime that is of interest for transparent electrodes to combine high electrical conductivity and high optical transmittance.

Lagrange et al. [92] define ϕ_c as the AgNW-density, where the percolation probability is $\frac{1}{2}$. This would mean that a charge carrier can either be transferred or not by a 50 % chance. Khanarian et al. [84] further introduce equation 2.5 to calculate the theoretical ϕ_c. The authors discuss the importance of the D- and L-distribution, the higher the effective length of AgNWs, the lower is the ϕ_c.

$$\phi_c = \frac{18 \langle D \rangle \langle L \rangle}{\pi \langle L^2 \rangle} \quad [84] \tag{2.5}$$

The ϕ_c is thus defined in literature by the effective AgNW-dimensions as given by the D- and L-distributions [84] and also, by the percolation probablity.[92]

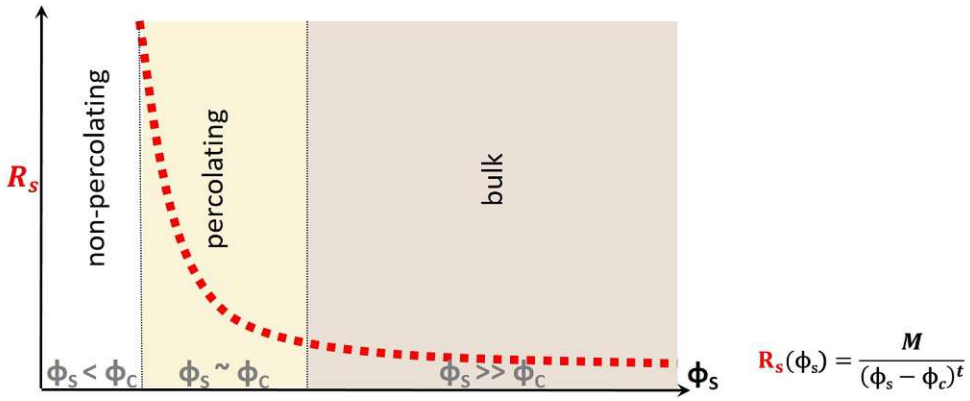

Figure 2.9: **Percolation regimes:** The critical AgNW surface fraction is marking the threshold that needs to be exceeded to enter the percolating and conductive regime. Below ϕ_c the network is not conductive. At high ϕ_s the system approaches bulk Ag properties.

2.4.2.2 Material factor (M)

Several authors emphasize the importance of a multitude of material parameters, like the length (L), diameter (D), L- and D-distribution, synthesis residuals and other apects of processing and applied treatments. A material factor M is required to take these influences into account. Bellet et al. [94] refer to this with a factor that depends on features of the specimen but not on the AgNW-density. Khanarian et al. [84] further define the material factor as shown in equation 2.6 below. The D is the AgNW diameter, ρ the resistance of bulk silver and C the deviation of AgNW-resistance from ρ. It is based on Monte-Carlo simulations [99] and experimental data from AgNWs of different AR that are embedded in a polymer.[84]

$$M = \frac{8\,\rho\,C}{\pi\,D} \quad [84] \tag{2.6}$$

If C = 1, the AgNWs would be flawless. But metal nanostructures cannot achieve the same level of conductivity as bulk metal, it is thus assumed that C > 1. The resistance in AgNWs depends on defects, the size of the nanostructures and surfactant residuals from synthesis. When AgNW-TEs are optimized, then R_s, ϕ_c and C should be minimized by considerate choice of AgNW-dimensions and treatments, which affects R_w and R_j. The specific contribution of R_w and R_w are discussed in literature. [85, 97, 93] But the relative resistance contributions are not trivial.[95, 93] The authors propose equation 2.6 for networks with wires in intimate contact, so that R_j can be neglected.[84]

2.4.2.3 Resistance ratio ($\frac{R_{junction}}{R_{wire}}$)

The relative resistance ratio can be assessed from microscale or macroscale levels.[95] In figure 2.10 a SEM image of AgNWs in microscale is depicted, where the AgNWs are schematically equivalent to an electrical circuit, as seen in literature.[95, 93]

The AgNW-AgNW contact resistances are shown as R_j and the wires themselves have an intrinsic resistance R_w.

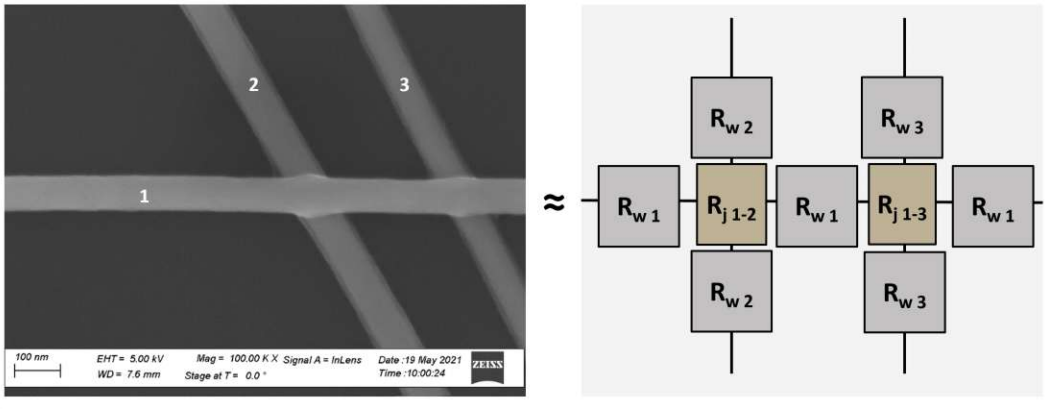

Figure 2.10: **Junction- and wire-resistances:** Schematic representation of resistance-contributions in an electrical circuit. Macroscopically, the single contributions can be summarized in overall R_j- and R_w-values. (modified from [93, 95])

It is convenient to introduce a resistance ratio ($\frac{R_j}{R_w}$) to handle relative resistance contributions from wires and junctions. Within the percolating regime, the network resistance can either be wire-dominated (low $\frac{R_j}{R_w}$) or junction-dominated (high $\frac{R_j}{R_w}$).

a) $R_{junction}$-dominated network - high $\frac{R_j}{R_w}$:

AgNW-networks are often assumed to be dominated by R_j and junction-improvement is thus considered particularly effective.[85, 97] The measured R_j of single nanowire-junctions are reported to be extremely high without any treatment [100] and various approaches are suggested in literature to decrease R_j. Possible treatments for R_j-reduction are listed below. Most of them are based on joining AgNWs and removing insulating surfactant. The choice depends on the processing conditions. Heat sensitive substrates for instance, often forbid thermal treatments.

I) Thermal treatment [100]
II) Mechanical pressing [101]
III) Plasma treatment [38]
IV) Chemical treatment [102]
V) Electrical treatment, Joule heating [103]

b) R_{wire}-dominated network - low $\frac{R_j}{R_w}$:

When R_j is minimized, then the network-resistance is dominated by R_w. Networks dominated by R_w are considered ideal. Partial resistance contributions from defects and grain boundaries, D and L as well as D- and L-distributions, are included in R_w. These explain a resistance increase in AgNWs in comparison to bulk Ag, as discussed with the C-factor before (equation 2.6).

2.4.2.4 Critical exponent (t)

If t=1, then $\frac{1}{R_s}$ plotted against ϕ_s is linear (equation 2.4). But this can only be the case in periodic meshes. AgNW-networks are not periodic and depend on a random distribution of AgNWs.[104, 93] Random networks have dangling and isolated regions that are not part of the current-carrying backbone.[105] In random networks, the critical exponent is thus increased (t $>$ 1). Based on computational models, the exponent t approaches a universal value of 4/3 ($\approx$ 1.3) in 2D networks.[106, 94, 84] The current flows in x- and y- direction, while current-flow in z-direction is negligible. A transition from 2D to 3D causes an additional dependence of conductivity on the thickness, as conduction paths in z-direction are available. In 3D networks, the critical exponent is said to approach 2.[107] A periodic mesh is compared to 2D-, and 3D-networks in figure 2.11.

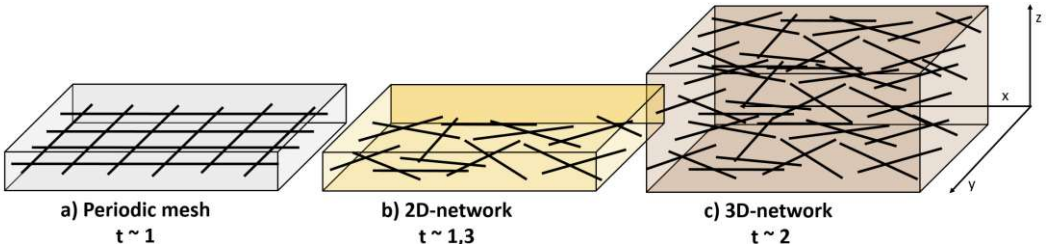

Figure 2.11: **Critical exponent:** The t contains information about the network-dimensionality. In 2D, the current flows in x- and y- direction, while in 3D, paths in z-direction are available.

The critical exponent t is further affected by the resistance ratio. Using Monte-Carlo simulations, Fata et al. [93] observed that t decreases with decreasing resistance contribution of R_j. Decreasing R_j thus decreases the effective dimensionality of the network.

2.4.3 Dependence of optical properties on the AgNW-density

In transparent electrodes, high conductivity is combined with high transmittance, which is as well dependent on the AgNW-density. Lagrange et al. [92] proposed equation 4.5 to describe linearly decreasing transmittance with increasing AgNW-density.

$$T = T_{substr}(1 - \beta\phi_s) \quad [92] \tag{2.7}$$

T... AgNW-TE transmittance T_{substr}... substrate transmittance β... fitting factor

The slope β is further defined in equation 2.8 for uncoated AgNW-networks.[92]

$$\beta = \frac{4}{\pi d_{Ag} D}(1 - (1 - refl_{AgNW})T_{AgNW}) \quad [92] \tag{2.8}$$

d_{Ag}...	density of bulk Ag	D...	AgNW-diameter
$refl_{AgNW}$...	optical reflection of one AgNW	T_{AgNW}...	transmittance of one AgNW

2.5 Applications

AgNW-TEs can find several applications. Characteristics are mostly ruled by the AgNW-density, as quantified by the AgNW surface fraction (ϕ_s). The targeted properties are based on the desired application and conditions in the final device. The application determines the choice of additional materials for building composites and decides over the expected properties.

2.5.1 Transparent electrode properties

Figure 2.12 gives an overview of electro-optical properties in dependence on the AgNW-density. Relevant trends of the transmittance (T, total transmittance T_{total} or normal transmittance T_{normal}), sheet resistance (R_s) as well as the FOM_{Haacke} and the haze (H=$\frac{T_{diffuse}}{T_{total}} = \frac{T_{total}-T_{normal}}{T_{total}}$) as a function of ϕ_s are sketched. It shows that a compromise between electrical and optical properties requires well considered ϕ_s.

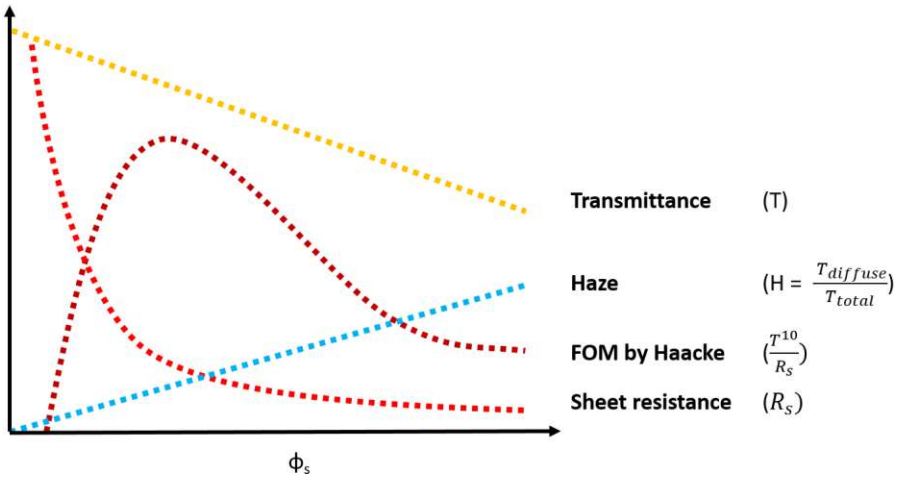

Figure 2.12: **Influence of the AgNW surface fraction ϕ_s:** The interplay between electro-optical characteristics and ϕ_s is shown. T and H scale linearly. R_s shows indirect proportionality, as explained with equation 2.4. FOM_{Haacke} shows a maximum at certain ϕ_s, indicating good TE-performance. This comparison demonstrates the complexity of a good understanding of the AgNW-based TE properties and the importance of well considered ϕ_s. (modified from Sannicolo et al. [9])

Optical transmittance usually decreases linearly with increasing ϕ_s, due to increasing covered areas. The R_s drops with ϕ_s, because more AgNWs offer more electrical pathways, which increases electrical conductivity and decreases R_s. Electrical properties are based on the formation of a network and the indirect proportional behaviour of $R_s(\phi_s)$ can be modelled with percolation modelling, as explained before (equation 2.4). The interplay between R_s and T is commonly rated by the FOM by Haacke.[37] When FOM_{Haacke} is plotted against ϕ_s, a bell-shaped curve can be obtained. Maximal values

indicate a good trade-off in electro-optical properties for a certain material. Haze represents the amount of diffusely scattered light, which is of interest in many applications. It is expected, that haze increases linearly with ϕ_s because of the increasing surface area that increases the chance of light to be scattered.[92]

The targeted TE-properties depend on the final application, profound considerations of the final application are thus required beforehand to develop optimal TEs. Common applications are linked to certain requirements and the optical properties are often decisive. High T_{total} is detrimental in applications, where the vision would be restricted. For instance, in displays, touch-screens or smart windows one aims for high T_{total} and also, low haze to prevent blurriness. High haze on the other hand, is of interest in photovoltaics (PV) or organic light emitting diodes (OLED). Scattered light enhances the optical path length of photons, high haze thus increases the absorbance probability of photons. The conversion efficiency in PV was reported to be greatly improved by using hazy electrodes.[108, 109] Also, the power efficiency in OLED devices was reported to be increased by AgNW-anodes as compared to ITO.[110]

When it comes to economic and environmental aspects, one always strives for low brittleness, low toxicity, high stability and low costs. To discuss the stability of AgNW-networks, some theoretical background on silver migration is given.

2.5.2 Silver migration

The long-term stability is often decisive for the feasibility of TEs in the final device. Electrical properties of AgNW-networks can degrade, due to Ag migration. Furthermore is the stability of sparse AgNW-networks particularly sensitive within the percolating regime. The tendency of silver to migrate is thoroughly studied for environmental and possible health risk reasons.[111] But silver migration is also of interest to understand the stability of AgNW-networks.[112]

Glover et al. [111] proposed a mechanism for the formation of new particles in vicinity to parent silver nanostructures, they suggest a pathway in three stages:

I) surface oxidation and particle degradation
II) surface confined mass transport within an adsorbed water layer
III) nanoparticle nucleation with help of a mild reductant

Ion release of Ag^+ in the first stage is widely studied to understand the environmental fate and biological impact of silver nanoparticles.[111, 113] The Ag^+-formation is rate-dependent on the size of the nanostructure [113] and the acidity of the environment.[114] Any conditions that enhance the formation, transport, reduction of Ag^+ are potentially destabilizing for AgNW-networks. AgNW-networks are in particular sensitive towards high temperature[92], acidic environment [115, 116], light exposure [112], humidity [116],

corrosive atmosphere [112] and if integrated in composites, non-sufficient coverage can enhance corrosion of bare AgNW-sites. Furthermore, hygroscopic and acidic properties of PEDOT:PSS are discussed to cause poor stability, when integrated in AgNW composites.[112, 9, 115, 116, 117]

Within this work, the stability of TEs at elevated temperature and atmospheric conditions are of interest, as the application of TEs as transparent flexible heater is targeted.

2.5.3 Flexible transparent heater

Transparent heaters (TH) are TEs that are supposed to generate heat. Resistive heating is induced by a current that flows through the electrode layer. Heat is usually regulated by the applied voltage. The relevance of transparent heaters takes roots in the 1950s, when SnO_2 was applied on cockpit windows for defrosting purposes.[43] The additional transparency allows that the field of vision is not restricted. The heating can thus find application to remove ice and frost from exterior facing windows that are exposed to temperature variations in vehicles, buildings or sensors. But it can also be used in sophisticated applications, as a medium to induce thermochromic transitions, for instance.[118, 119] Flexibility gives rise to more possibilities. The market for flexible THs is thus growing fast.

In 2012, Celle et al. [40] were among the first to report the implementation of AgNW-networks as TEs for heating. The same group a few years later also reported efficient THs that are based on conductive polymers only.[120] Since then, several other reviews and papers have been published, showing the value of AgNWs for TH applications.[42, 9, 41, 121]

The concept of resistive heating is based on Joule's law, experimentally shown in 19th century. An electrical current that flows through a material with a certain electrical resistance releases heat, equation 2.9 describes this effect. In addition to equation 2.9, heat can also be defined through equation 2.10 with the specific heat.

$$H = I^2 * R * t \tag{2.9}$$

H = heat I = current R = resistance t = time

$$H = C * m * \Delta T \tag{2.10}$$

U = voltage m = sample mass C = specific heat capacity T = temperature

Equations 2.9 and 2.10 can be set equal. Taking Ohm's law ($U = R * I \rightarrow I = \frac{U}{R}$) into account, the current factor can be substituted. Rearrangements lead to equation 2.9,

which shows a squared relationship between the temperature change and the voltage, the heating is further indirectly proportional to the material's specific heat capacity.

$$\mathbf{\Delta T} = \frac{\mathbf{t}}{\mathbf{C} * \mathbf{m} * \mathbf{R}} \mathbf{U^2} \tag{2.11}$$

An optimal combination of sample resistance and applied voltage determine the temperature increase, but research effort is devoted to efficiency and heating from low voltages. The particular operation voltages depend on the application. Example given, 3,6 V of common batteries up to 12 V from car batteries are convenient threshold voltages for TH development. Further, the specific heat capacity affects the energy that is required to raise the temperature for a specific sample mass. The heat capacity and mass quantities of the materials that are combined in the composite-TE significantly affect the heating properties.

Important properties of flexible transparent film heaters, that require to be considered are in summary the following.[42]

a) Steady state temperature

At an applied voltage, temperature rises rapidly. Temperature saturates at a steady-state temperature (T_{steady}), because of a balance with heat loss.

b) Thermal response time

In an energy-efficient TH, a voltage causes maximal temperature increase in minimal time. The time until 90 % of T_{steady} is achieved, is called the response time.[9]

c) Cycling stability

The stability of an TH can be tested by thermal cycling, where the reproducibility of heating is investigated by switching voltage ON/OFF.

d) Homogeneity

The homogeneity of the TH is important to guarantee uniform temperature over broad surface areas without hot-spots. AgNW-agglomerations or -clusters can disturb the current-carrying backbone and can cause hot-spots. Hot-spots are areas that carry high currents which may break the network in long-term usage.[42] The homogeneity of heating and the current-distribution in AgNW-based THs is in literature reported to be significantly improved by TCO-embedding.[122]

3 Materials and methods

3.1 Deposition of materials

3.1.1 Substrate preparation

ZnONP-layers were first deposited on Si-substrates to improve the contrast in SEM. For cleaning, the Si-substrates were ultrasonicated in Aceton, Isopropanol and deionized water for 15 min each. Polycarbonate (PC), with a thickness of 250 μm, was used as substrate for the developed transparent electrodes. The PC-foil was protected by two liners, which were peeled off before usage. No further cleaning was required. The substrates were cut in sample sizes of 2.5 x 2.5 cm and 5 x 5 cm.

3.1.2 Spray-coating

A sketch of the spraying set-up is shown in figure 3.1. ZnONPs and AgNW were sprayed with a Sono-Tek ExactaCoat system, equipped with an ultrasonic Sono-Tek Impact Nozzle operating at 120 kHz frequency in horizontal geometry. Pressurized air was used as shaping air to guide the stream towards the substrate, which was placed on a steel plate that resides on a hot plate. The dispersion was fed from a single supply. The flow rate was controlled through steady syringe movement.

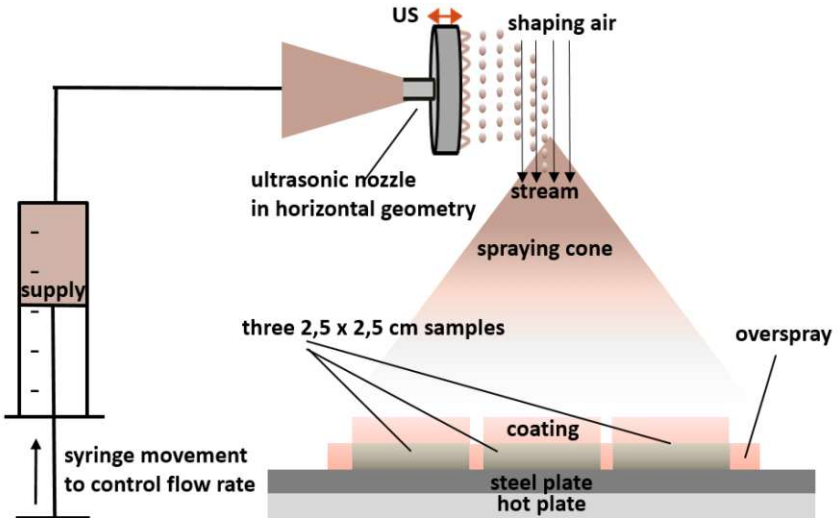

Figure 3.1: **Spray coating set-up:** Dispersion is fed from a single supply syringe to the ultrasonic nozzle in horizontal geometry. Pressurized air is directing the stream towards three alligned samples, where the coating is deposited within the defined area.

Due to the fact that the substrates are lightweight and flexible, it was necessary to fix them with glass plates to prevent them from being blown away. The nozzle was following an arc spraying pattern, as sketched in figure 3.2 a). The area is set with y- and x- values, which define a rectangular spraying area. The speed and the spacing need to be set. The spraying area and position in the spraying chamber were adjusted empirically by spraying water on the steel plate first, and marking the desired sample positions in the middle of the wet area. Fine adjustments to find the optimum positioning were undertaken on the basis of obtained sheet resistance gradients and SEM observations. Three 2.5 x 2.5 cm samples or two 5 x 5 cm samples (dashed lines) were positioned on the hot plate in the spraying chamber, as indicated in figure 3.2 b).

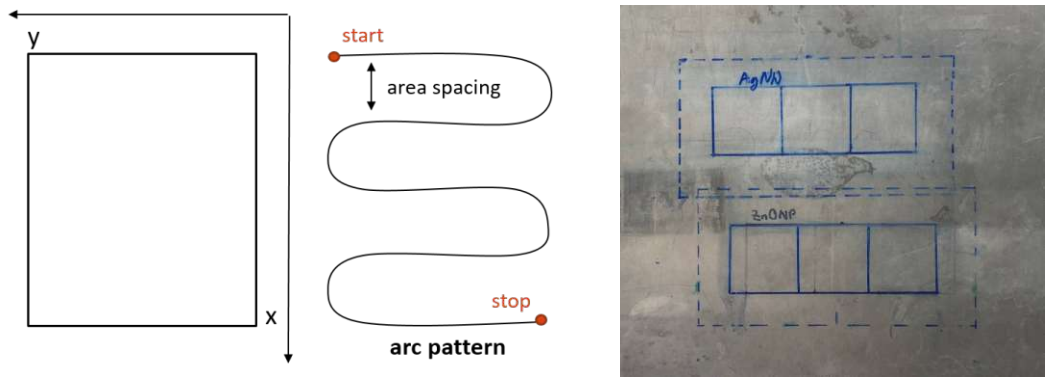

(a) spraying pattern within sprayed area (b) steel plate with marked sample positions

Figure 3.2: **Spray coating nozzle movement:** The nozzle draws an arc pattern with defined speed and area spacing. Samples are placed in optimized positions.

3.1.2.1 Spray-coating of ZnONPs

The ZnONP suspension was prepared by diluting ZnO nanoparticle ink (Sigma Aldrich, 793361, 10-15 nm particle size, 2.5 wt.%) 1:10 by volume with Isopropanol (2-Propanol 99.9 % for HPLC, Sigma Aldrich, 34863). The dilution is stable in the fridge for several months and was ultrasonicated for 5 min before usage to avoid agglomerates. The deposition was carried out at 0.4 mL/min flow rate, 1-5 bar shaping air overpressure and hot plate temperature that varied between room temperature ($\approx$ 23 °C) and 100 °C during optimization. 3 bar shaping air pressure and 100 °C substrate temperature lead to satisfying films. The nozzle operated at a power of 1.7 W and a frequency of 120 kHz. The scan speed was 20 mm/sec drawing and the nozzle movement was an arc pattern with 25 mm area spacing from a nozzle to substrate distance of $\approx$ 14 cm. A complete run of 30 scans lasts $\approx$ 6 minutes and consumed $\approx$ 2.4 mL stock dispersion. A total of 10-60 scans were tested in intervals of 10 scans during thickness optimization. 30 scans resulted in sufficient coverage. After spraying, a rest time of 5 min at 100 °C was employed to guarantee full solvent evaporation. The ZnONP layer deposited in this manner was then investigated as base- and top-layer for AgNW embedding.

3.1.2.2 Spray-coating of AgNWs

Silver nanowires (60 nm D, 10 µm L, 0.5 wt. %, Sigma Aldrich, 739421) were gently shaken by hand before adding certain amounts to Isopropanol (2- Propanol 99.9 % for HPLC, Sigma aldrich, 34863) to obtain the dilutions. Dilutions ranging from 1:5 to 1:40 by volume were prepared during optimization. The 1:10 dilution with a solution transmittance ≈ 0.3 (as described later) was chosen for further investigations. The suspension is diluted to avoid agglomerations of AgNW during spraying. But the dilution should not be too high in order to obtain fast depositions. The used AgNWs were provided as suspensions with certain solid contents in IPA. High purity IPA was used for dilutions. Low puritiy IPA was not used, because AgNWs are expected to corrode in the presence of water and impurities.[123, 124]

Although, the nominal solid content of the different AgNW bottles was the same, significant deviations from one bottle to another occurred in some cases. To increase the reproducibility, transmittance measurements of the diluted suspensions were introduced as quality control measure. Samples were also prepared with AgNWs from ACS (7440-22-4, 60 nm D, 20-30 µm L, 20 mg/mL) due to their larger length. The dilution with Isopropanol was varied between 1:50 and 1:200 by volume, where 1:100 with a solution normal transmittance of ~0.3 was chosen as optimal for further processing.

To investigate the influence of D and L on the optical and electrical properties, samples with thicker (D=90nm) and thinner (D=40nm) AgNWs were investigated. Dispersions from ACS AgNWs were diluted 1:100 by volume for D= 40 nm AgNW (7440-22-4, 40 nm D, 20-30 µm L, 20 mg/mL). AgNWs with D= 90 nm were less diluted, namely 1:50 by volume (7440-22-4, 90 nm diameter, 20 mg/mL). IPA (2- Propanol 99.9 % for HPLC, Sigma aldrich, 34863) was used as solvent for dilution. For explanation, to obtain similar numbers of AgNW per volume, the dilution per volume needed to be adjusted from 1:100 to 1:50 for D= 90 nm AgNWs. The weight concentration is the same for all D, but the molar concentration varies.

(a) Rings (b) Sedimentation

Figure 3.3: **AgNW dispersion stability:** Observations from a) shaking over night and b) storage in the fridge for one month without intermediate shaking.

Prepared dilutions were placed on a benchtop shaker for 2-3 hours to avoid aggregation and guarantee a homogeneous dispersion. Shaking overnight caused rings of AgNWs at the liquid level (figure 3.3 a)) and was therefore avoided. Ultrasonication can break the nanowires and thus shift the length distribution towards lower lengths, as also observed in the literature.[125] Ultrasonication of AgNW suspensions was therefore excluded. Dispersions were prepared freshly or sprayed within a few days. The suspensions were stored in the fridge and gently shaken before usage. Sedimentation was otherwise observed. Suspensions stored for one month in the fridge are shown in 3.3 b). These were hard to redisperse by shaking and were thus discarded.

The spray coating was carried out with 9 bar shaping air overpressure and 1.7 W nozzle power at 100 °C substrate temperature. Flow rates of 0.4 mL/min and 0.8 mL/min were compared. 0.8 mL/min resulted in more stacked AgNWs and was therefore not continued. A spraying speed of 10 mm/s and a narrow area spacing of 1 mm at a flow rate of 0.4 mL/min resulted in homogeneous layers of AgNW networks, confirmed by SEM. One scan of AgNW deposition in this manner lasts ≈ 6 min 40 sec and requires ≈ 2.6 mL stock dispersion. Variations in stock dilutions (1:5 to 1:40 with MKCL3904) and in scan number from 2-6 scans gave rise to varying AgNW density. The number of scans were kept minimal, as to avoid 3D stacking of AgNWs.

3.1.3 Spin-coating

Spin coating was used at the current stage of development for the deposition of PEDOT:PSS. Spin coating is a convenient pre-upscaling method. Upscaling could be realized by means of spray coating or doctor blading from similar stock suspensions.

3.1.3.1 Spin-coating of PEDOT:PSS

Heraeus Clevios PH1000 with a content of 1.3 wt. % PEDOT:PSS (0.5 % PEDOT, 0.8 % PSS) in aqueous dispersion was used. It was brought to room temperature and filtered through a 0.45 μm syringe filter before usage. Spin coating of the concentrated dispersion did not result in homogeneous films due to too high viscosity. Thus, the dispersion was further diluted, namely 1:1 with ultrapure water (Merck Millipore Milli-Q, >18 MΩ) by volume to decrease the viscosity. Homogenization of the dispersion was done by magnetic stirring for ≈ 5 min at room temperature. The thus obtained dispersion with pH ≈ 2.7 was stored in the fridge, where it remained stable for several weeks.

To study the influence of addition of a low boiling point solvent, 5 vol.% of Dimethylsulfoxide (DMSO, Sigma Aldrich, D8418) was added to the described PEDOT:PSS dispersion, to investigate enhanced conductivity as described in literature.[69, 67, 126] Another series of samples was prepared to investigate the influence of pH on the stability and conductivity of AgNWs. Dispersions were neutralized to pH 6.9 by cautiously adding 0.5 M NaOH. But for most samples, acidic PEDOT:PSS without DMSO was used.

Spin coating was done by distributing 900 μL of PEDOT:PSS dispersion with a pipette on the sample. Spinning was performed for 30 seconds with 4000 rpm. Velocities of 2000 rpm and 3000 rpm were tested, but 4000 rpm lead to most homogeneous films. After spinning, a curing step at 100 °C for 30 minutes on a hot plate was conducted.

3.1.3.2 Spin-coating of PVP

It was seen that the wettability of aqueous PEDOT:PSS dispersion on PC/AgNW was satisfactory. But PEDOT:PSS did not wet the bare PC, forming islands instead of continuous films. To deposit single PEDOT:PSS on PC, Poly(vinylpyrrolidone) (PVP) was therefore used as wetting agent on PC. 1 mg/mL PVP (Sigma Aldrich, average 10.000 g/mol, 9003-39-8) was dissolved in ultrapure water (Merck Millipore Milli-Q, >18 MΩ), ultrasonicated for 10 minutes and deposited as wetting layer prior to PEDOT:PSS deposition. 500 µL were applied and spun at 4000 rpm for 30 seconds, followed by a curing step at 100°C for 10 min.

3.1.4 Final recipes

Described optimization resulted in the following recipes for sprayed AgNW (ACS, 7440-24-4, D 60 nm, L20-30µm, 20 mg/mL) and sprayed ZnONP (Sigma Aldrich, 793361, D 10-15 nm, 2.5 wt.%). Both were suspended in IPA (2-Propanol for HPLC, Sigma Aldrich, 34863, 99.9 %). Spraying was carried out at a power of 1.7 W and with 120 kHz frequency to gain a fine spray of IPA with the suspended nanostructures. A flow rate of 0.4 mL/min and a substrate temperature of 100 °C were used. The distance between nozzle and substrate was ≈ 14 cm. After spraying, a dwell time of 5 minutes at 100 °C was employed to assure full evaporation of IPA.

Other spraying parameters are shown in 3.1. The parameters for spin-coating of PEDOT:PSS are shown in table 3.2.

With these building blocks, the two TEs PC/ZnONP/AgNW/ZnONP and PC/AgNW/PEDOT:PSS were built, which were compared to a reference PC/AgNW.

Table 3.1: **Final recipes spray coating:** Parameters for deposition of AgNWs and ZnONPs

	dilution *per vol.*	**scans** *number*	**volume** *mL/scan*	**time** *sec/scan*	**shaping air** *bar*	**speed** *mm/sec*	**spacing** *mm*
ZnONP	1:10 IPA	30	≈ 0.08	≈ 13	3	20	25
AgNW	1:100 IPA	3	≈ 2.6	≈ 400	9	10	1

Table 3.2: **Final recipes spin-coating:** Parameters for deposition of PEDOT:PSS and PVP

	dilution *vol.*	**speed** *rpm*	**spinning time** *sec.*	**temperature** *°C*	**annealing** *min.*
PEDOT:PSS	1:1 DI water	4000	30	100	30
PVP	1 mg/mL DI water	4000	30	100	10

3.2 Characterization

3.2.1 Sheet resistance

The sheet resistance (R_s) was measured with a 4-point-probe (Nagy SD-600) at five spots per sample, as shown in figure 3.4. The average and standard deviation were calculated.

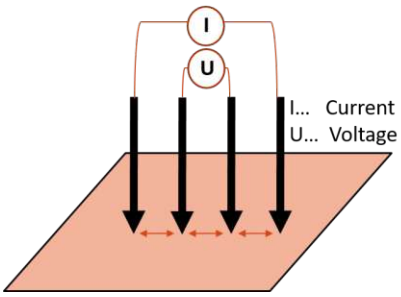

(a) Four probe sheet resistance measurement

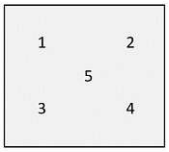

(b) Five spot measurement routine

Figure 3.4: **Sheet resistance measurement:** a) 4-point-probes induce a current while voltage is measured. Five spots were measured per sample, as sketched in b). (modified from [127])

3.2.2 UV/Vis Transmittance

The transmittance of thin films and AgNW suspensions was systematically measured. The sample holder for solution transmittance measurements was custom-made. Optical transmittance in ultraviolet (UV), visible (Vis) and infrared (IR) region was conducted on a Bruker Vertex 70 Fourier transform spectrometer. For 330-550 nm a GaP-detector was used and a Si-detector for the 550-1150 nm range. Two different detector geometries were employed. For measuring normal transmittance, the detector was aligned with the incident beam. Measurement of total transmittance, including specular and diffuse transmittance, was carried out with a teflon-coated integration sphere from Bruker and a detector in orthogonal position to the sample.

The set-ups are sketched in figure 3.5. From transmittance measurement in these two set-ups, haze values were calculated according to equation 3.1.

$$haze = \frac{T_{diffuse}}{T_{total}} = \frac{T_{total} - T_{normal}}{T_{total}} \tag{3.1}$$

T_{total} = total transmittance (integration sphere in orthogonal position)
T_{normal} = normal transmittance (detector and beam in line)

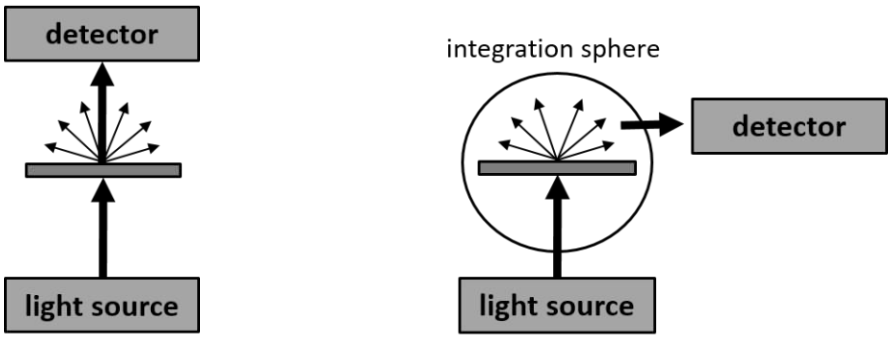

(a) alligned detector position for T_{normal} (b) orthogonal detector position for T_{total}

Figure 3.5: **Transmittance measurement:** Normal transmittance is excluding diffusively scattered light while total transmittance includes scattered light with help of an integration sphere.

For further data treatment and calculating haze with equation 3.1, transmittance values at 550 nm were used as representative values for visible light range and as commonly used in the literature.[128, 92]

3.2.3 Profilometry

Height profiles were measured on a KLA Tencor surface-profiler (Alpha-Step IQ) over a distance of 500 µm with a speed of 20 µm/s. The roughness was determined. Rq values were noted, which correspond to the root mean square values of height differences.

3.2.4 Scanning electron microscopy

Scanning electron microscopy (SEM) was performed on a Zeiss SUPRA-40 using 5 kV acceleration voltage and an in-lens positioned secondary electron detector.

3.2.5 Energy dispersive X-Ray spectroscopy

The SEM is also equipped with an Energy Dispersive X-Ray Detector (EDX, Octane Elite EDS System and EDAX APEX software) for measuring elemental compositions of spots, lines or for mapping. It was operated at 8.5 mm working distance and an acceleration voltage of 5-20 kV. A secondary electron detector was used for imaging purposes.

3.2.6 ImageJ

SEM images were further analyzed with ImageJ software. Basic settings were adjusted and information such as layer thicknesses, AgNW dimensions and AgNW surface coverage were extracted from the images.

3.2.6.1 AgNW surface fractions

The AgNW density was quantified using the AgNW surface fraction (ϕ_s). The ϕ_s refers to the percentage of the surface covered by the AgNWs. The ϕ_s was calculated with help of ImageJ. The method of determining ϕ_s is inspired by experimental reports by Lagrange et al.[92] The parameter was extracted from 4-5 SEM images taken at different locations on the samples. Firstly, threshold values for the contrast were set in ImageJ and then the percentage of image pixels above this threshold was extracted, representing the ϕ_s. Screenshots from ImageJ from determination of AgNW surface fractions (ϕ_s) are shown in figure 3.6. The red areas are the identified AgNW areas. Also shown are un-processed SEM images for comparison below. The determination of ϕ_s for ZnONP embedded AgNWs in comparison to PEDOT:PSS coated AgNWs is challenging due to smaller contrast differences and regions of high-density ZnONPs. This increases the standard deviation in ϕ_s for the PC/ZnONP/AgNW/ZnONP samples.

3.2.6.2 AgNW length- and diameter-distributions

Length- and diameter-distributions were determined for used AgNWs (referred to as sigma60, ACS40, ACS60 and ACS90). Low density AgNW coatings were sprayed on PC in the manner described above. Low AgNW density was required to easily identify single wires. Coating with PEDOT:PSS reduced charging effects and therefore produced better contrast in the SEM images, as shown in figure 3.7. Pictures were taken from at least three different spots to measure diameters and lengths with help of ImageJ. 15-40 random measurements of AgNW lengths and diameters per sample were used to build averages and standard deviations. Obtained distributions were compared to manufacturer's material specifications.

3.2.7 Percolation modelling

Electrical properties originate from the percolating behaviour of AgNW networks. Percolation models were used to extract theoretical values from experimental data.[84, 92, 94, 93] As input parameters for these models, the extracted AgNW surface fractions (ϕ_s) were of critical importance. Data sets for several samples of different ϕ_s were fitted to $R_s(\phi_s)$ and also, $T_{total}(\phi_s)$. The fitting of experimental data was done in OriginPro 2016 with user defined fits.

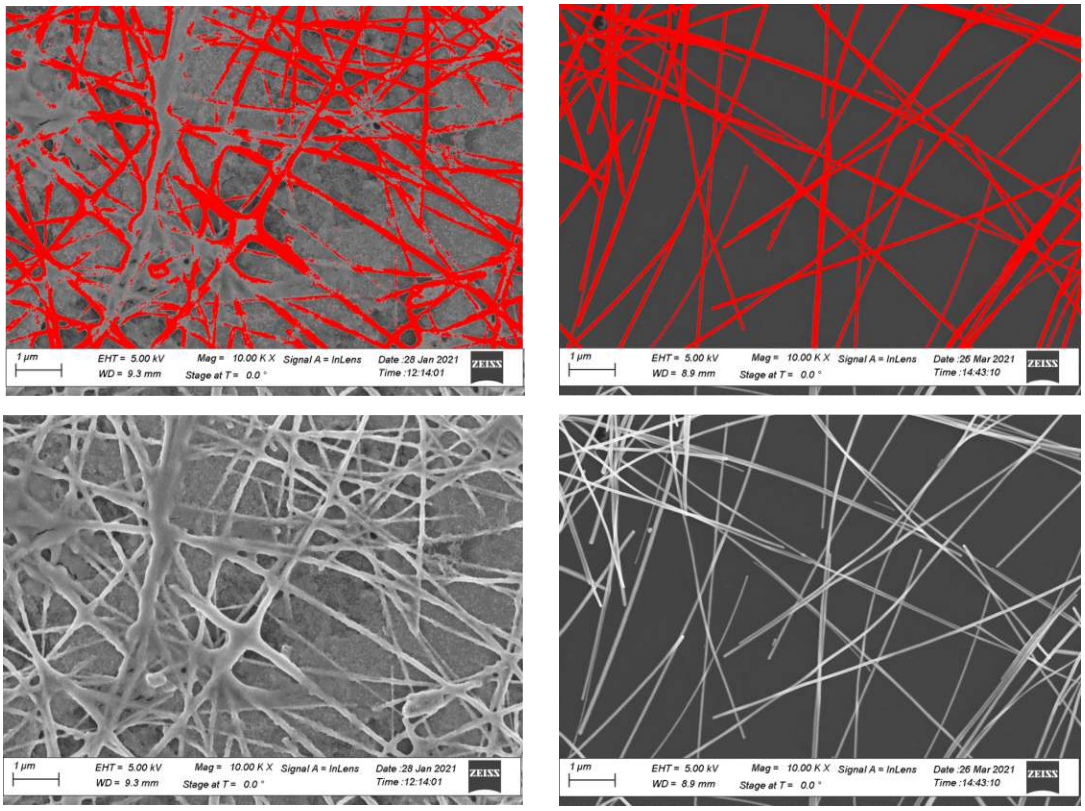

(a) PC/ZnONP/AgNW/ZnONP (b) PC/AgNW/PEDOT:PSS

Figure 3.6: **ImageJ:** Screenshots from ImageJ show ϕ_s areas in red. It can be seen, that this calculation is accurate for b) AgNW covered with PEDOT:PSS due to good contrast in SEM. The ϕ_s from a) AgNW embedded in ZnONP have an error.

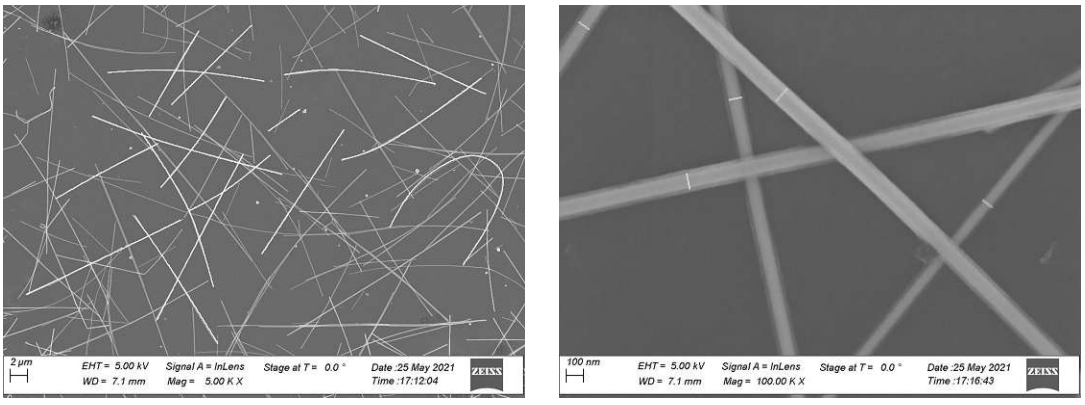

(a) AgNW length distribution (b) AgNW diameter distribution

Figure 3.7: **AgNW L- and D-distributions:** Examplary SEM pictures for AgNW ACS40 a) length and b) diameter distribution on low AgNW density sample covered with PEDOT:PSS. Random size measurements done in ImageJ are highlighted.

3.2.8 Stability study

To investigate the stability of AgNWs in different embeddings against oxidation in ambient, inert and elevated temperature (70 °C) conditions. Inert conditions were in N_2 atmosphere in a glove-box (pressure 3 mbar, water 0.6 ppm and oxygen 2.6 ppm). Sheet resistance values were measured every 2-3 days for the duration of one month. Two samples of each kind were investigated, one with high AgNW surface fraction by spraying 3 scans and one with low AgNW content by spraying 2 scans from 60 nm x 20-30 µm AgNW from ACS (7440-22-4). SEM images were taken weekly.

3.2.9 Transparent flexible heater

For the resistive heating experiments, the set-up is sketched in figure 3.8. Contacts were applied by brushing stripes of Ag paste on two sides. After drying over night, Cu tape was folded tightly around the Ag paste stripes. Wires were soldered on the Cu tape. Clamps were attached to the wires and connected to the terminals of the power supply (Keithley Sourcemeter Model 2400) as sketched in figure 3.8. The measurements were conducted free-standing, meaning that the heaters were not in contact with any surfaces. Voltages between 1-3.5 V were applied, until the measured surface temperature was stable (steady-state temperature). Resulting current was noted to calculate the resistance. Repeated power ON/OFF cycles at certain voltages were executed to investigate the reproducibility of reached temperatures. The thermal emissivity value of the sample (PC foil) was taken 0.8. Surface temperature was monitored as a function of time with an IR Thermometer (Peaktech 4960) from a distance of ≈ 20 cm via USB connection. The IR beam was directed on the PC foil side. The software ENV tool was used for data logging.

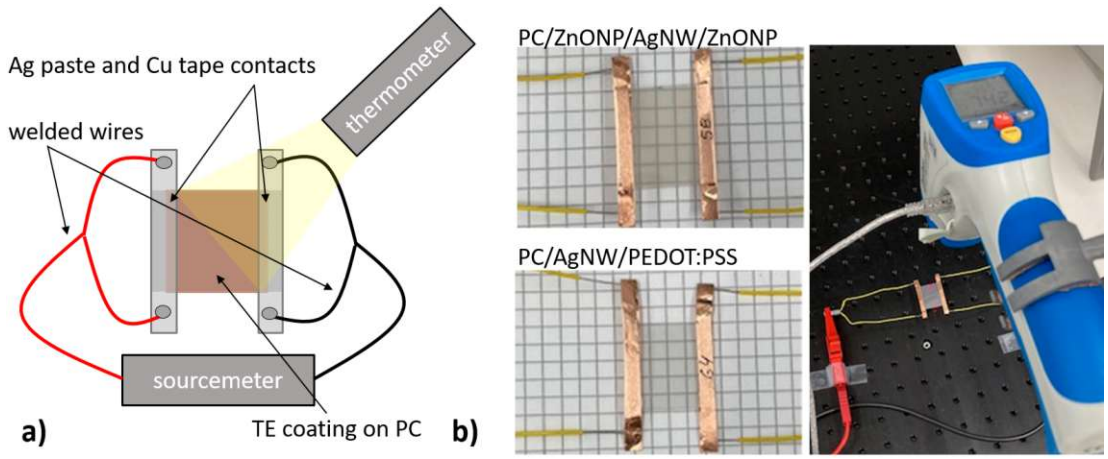

Figure 3.8: **Flexible transparent heater:** The set-up for resistive heating is shown. Voltage was applied via depicted contacts while surface temperature was measured. a) Sketched resistive heating set-up b) Photos of samples and the heating set-up

4 Results and discussion

Following representation of results focuses on the optimization of thin film deposition from ultrasonic spray-coating. Developed TEs are presented, followed by a discussion of electro-optical properties and observed effects in the percolating behaviour. Experimental data is fitted with percolation models to extract theoretical values. Stability aspects and application as transparent heaters are shown.

4.1 Deposition of materials

The TEs are built from three building blocks, spray-coated AgNWs and ZnONPs as well as spin-coated PEDOT:PSS. The AgNW-dimensions, as provided by suppliers, were investigated. Deposition parameters were studied and optimized.

4.1.1 Choice of silver nanowires

Figure 4.1 shows representative SEM images of investigated AgNWs. In table 4.1, averaged L- and D-values of these AgNWs are listed. The values were determined from SEM images of low AgNW-density. A number of 15-25 AgNWs were measured, averages and standard deviations were calculated. The AgNW diameter (D) and length (L) are put into relation in the aspect ratio (AR = L/D). The ARs in table 4.1 were determined from averaged L- and D-values. The errors equal the standard deviation.

The distributions are important, as they can be critical for the minimal number of required AgNWs for a conductive network.The AgNWs show certain standard deviations from the average length. It is thus important to exceed ϕ_c accordingly, to assure percolation. It can be seen, that diameter distributions are broader than length distributions. It is further apparent, that ACS90 fell below expectations, they were thus not investigated in more detail.

High ARs are desired for transparency and conductivity. Long wires with short diameters can provide longer percolation paths, leading to decreasing critical AgNW surface fractions with increasing AR.[129] But high-AR AgNWs are more difficult to spray. High AR values can cause the AgNW-length to exceed the droplet size, which can result in curved AgNWs.[128]

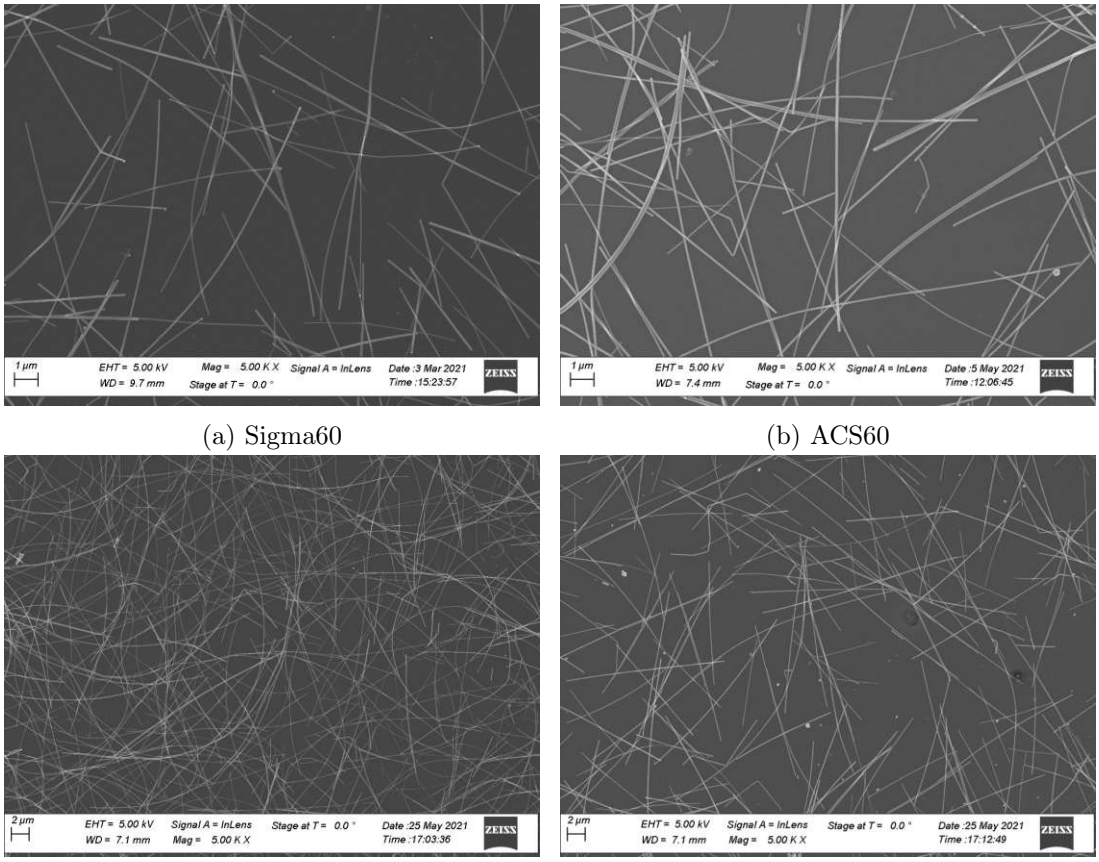

(a) Sigma60 (b) ACS60

(c) ACS40 (d) ACS90

Figure 4.1: **AgNW dimensions:** Representative SEM images of AgNWs, as indicated in a)-d).

Table 4.1: **AgNW dimensions:** Lengths, diameters and resulting aspect ratios of used AgNWs.

		expected	average	error	AR = L/D	measured AgNWs
Sigma60	D	60 nm	58.3 nm	± 15.2	158	21
	L	10 µm	9.2 µm	± 2.8		33
ACS60	D	60 nm	73.9 nm	± 12.7	356	15
	L	20-30 µm	26.3 µm	± 6.7		25
ACS40	D	40 nm	44.2 nm	± 11.0	545	16
	L	20-30 µm	24.1 µm	± 5.8		23
ACS90	D	90 nm	74.4 nm	± 14.0	208	24
	L	-	15.5 µm	± 5.2		42

Curved instead of elongated AgNWs compromise the formation of an efficient network and are therefore not desired. This curving effect can be more severe for thinner wires, due to their softer character. A slight curving effect can be seen in figure 4.1 c) for the thinnest AgNWs (D≈ 40 nm). Thicker wires are usually stiffer and easier to deposit randomly and without mechanical deformation. Further, thinner AgNWs are expected to be more sensitive towards silver migration, due to their higher surface to volume ratio.[114] Stability issues could be a limitation for thinner AgNWs in the final device. Also, when D approaches the mean free path of electrons in bulk silver, scattering of electrons increases the resistivity.[130]

For these reasons, diameters of 60 nm were considered a good compromise of high AR and good processibility, stability and conductivity. Most experiments during optimization were conducted with AgNWs from Sigma with nominal diameters of 60 nm and 10 µm length. But for final studies of environmental stability and the final representative samples, AgNWs supplied by ACS with nominal diameters of 60 nm and higher lengths of 20-30 µm were investigated. Khanarian et al. [84] recommend to use AR $>$ 250. The final AgNWs of choice with AR $\approx$ 356 were considered a suitable choice of AgNW-dimensions. They combine good expected stability and sufficient percolating behaviour, while maintaining good processability through spray-coating.

4.1.2 Spray-coating parameter study

Several spraying parameters contribute to the properties of spray-coated thin films, involving many mechanisms that occur simultaneously. The substrate temperature is a critical parameter that influences droplet size, solvent evaporation and thus affects the properties of the thin film. Low temperature processing requires thoughtful parameter optimization.

This subsection should serve as an overview of what is expected, when certain variables in spray-coating are changed. Interesting aspects of single parameters are stated. Discussed parameters include the following:

1. Substrate temperature
2. Solution composition
3. Nozzle Power
4. Flow rate
5. Shaping air
6. Sample positioning
7. Spraying pattern
8. Scan number

The separate discussion of either spraying ZnONPs or AgNWs follows afterwards in subsection 4.1.3.

4.1.2.1 Substrate temperature

The substrate temperature has an impact on the surface morphology in spray-coating, especially for sprayed ZnONPs. Figure 4.2 shows sprayed ZnONPs at room temperature and at 85 °C substrate temperature, which is close to IPA's boiling point.

At room temperature, ZnONPs are deposited as rings. A temperature increase leads to formation of several rings within each other, instead of single rings. The outer ring size stems from the initial spread of the impinged droplet, before solvent evaporation sets in. The observed rings are due to the coffee ring effect.[31, 21, 22] Capillary forces drive suspended particles to diffuse towards the droplet edges. This process is affected by the applied temperature, which speeds up the droplet drying process.

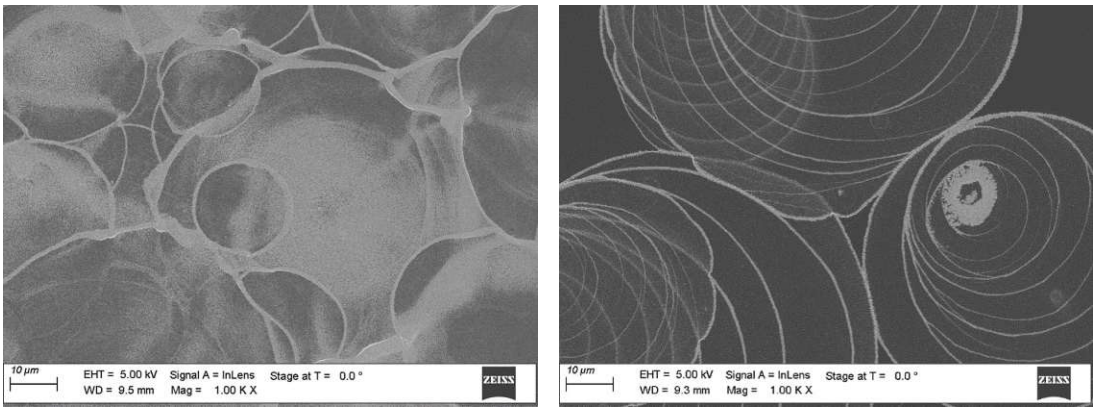

(a) ZnONPs, room temperature (b) ZnONPs, 85 °C substrate temperature

Figure 4.2: **Coffee ring effect:** Coffee rings from sprayed ZnONPs on Si-substrate. 10 scans were sprayed at a) room temperature and b) 85 °C. The latter lead to multiple rings within one initial droplet and a pattern of inner coffee ring deposits. The temperature in the final recipe was further increased to 100 °C.

The residence time of droplets on the substrate is longer at room temperature. The slowly shrinking droplet at room temperature carries less dispersed particles. Most are deposited within the initial droplet. At elevated substrate temperature, the droplet shrinkage is faster and fluid dynamics within the droplet are enhanced. The droplet shrinks in a stick-slip-mechanism and carries particles, which can diffuse to the shrinking droplet's contact lines to build inner coffee ring deposits (ICRDs).

Sprayed AgNWs do not show coffee rings. The effect is avoided by their high AR. Elongated nanostructures show suppressed diffusion.[21] For sprayed ZnONPs, the substrate temperature was further increased to 100 °C, which improved the ZnONP distribution due to the ICRDs instead of single rings. But other parameters needed to be investigated to achieve good coverage from this particular pattern of spray-coated ZnONPs.

4.1.2.2 Solution composition

The nanostructures were provided suspended and highly concentrated in IPA, but provided AgNWs settle in the bottle and they needed to be diluted for spraying purposes. The diluted dispersions need to be optimized within a specific range. The maximum dilution is determined by the requirements to maximize material usage and decrease the deposition times. The minimum is determined by the requirement to prevent agglomeration. The dilutions were developed empirically.

The reproducibility of the targeted AgNW solid contents is important. Concentration variations, due to sedimentation, made consistent dilution by volume challenging. Transmittance solution measurements were introduced to unveil batch to batch differences and to control batch to batch differences. Graphs in figure 4.3 show a) transmittance measurements of AgNW-suspensions of different solid contents, b) shows measured transmittance values at 900 nm as a function of solid contents.

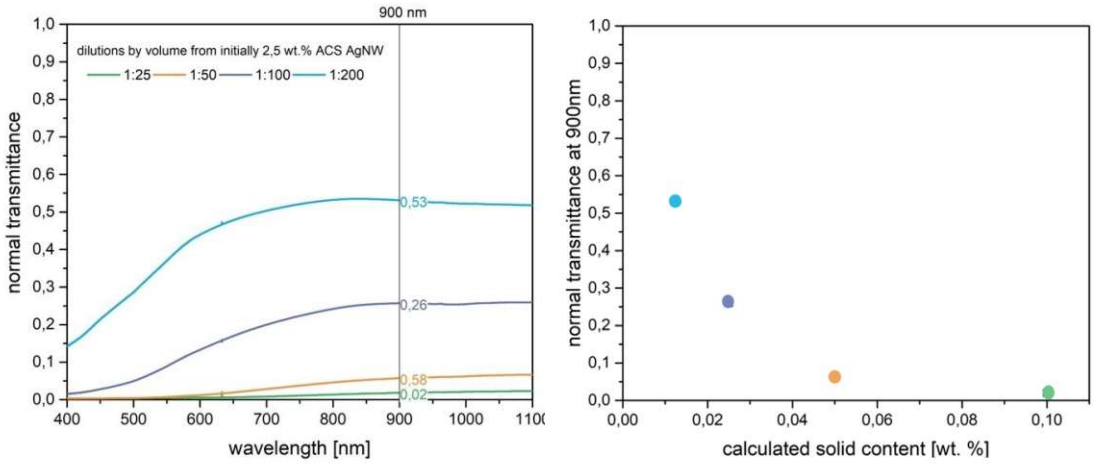

(a) (b)

Figure 4.3: **Quality-control of AgNW solid content:** UV/Vis solution transmittance of dispersions were measured for checking the desired concentration. Shown are a) T_{normal} from liquid ACS AgNW dispersions at different dilutions and b) values at 900 nm plotted against solid contents.

Dispersions with AgNW solid contents of ≈ 0.02 wt.% were considered appropriate for spraying, which show transmittances around 0.3. This graph served as a benchmark to evaluate the solid content of the prepared dispersions. Solution transmittances can be compared in a fast manner and are therefore an easy quality-control tool.

AgNW-suspensions were less stable than ZnONP-dispersions. Three weeks storage in the fridge resulted in sedimentation of solid AgNWs at the bottom of the bottle, as previously shown in chapter 3 in figure 3.3. Surfactants like PVP, as commonly used

in AgNW-synthesis [81], might have improved the dilution stability. But as AgNWs are already coated during their synthesis, further surfactant additives were not used. The insulating polymer shell increases the junction resistance of the AgNWs.[100] It would require 130 - 600 °C to fully pyrolize PVP from AgNW-surfaces, based on TGA-analysis from the literature.[88] Pyrolization of PVP after deposition, was not an option. Low temperature processing was desired for not deforming the PC-substrate. AgNWs were thus sprayed freshly diluted in IPA only, serving as a convenient low cost, low boiling point, pH neutral, non-toxic and non-corrosive solvent. This lead to homogeneous distribution of AgNWs without agglomeration.

ZnONP-dispersions were very stable and only required ultrasonication prior to spraying. This breaks apart possible agglomerates. Dilutions of ZnONPs in IPA without any additives could be used after several weeks of storage.

4.1.2.3 Nozzle power

A minimal nozzle power is required to break off droplets from a standing wave that is induced by ultrasonic vibration at the nozzle-tip. An ultrasonic nozzle operates at a certain resonant frequency, in our case at 120 kHz. If the power is too low, liquid stalls at the nozzle-tip and a vibrating bulb is formed. No droplets break off. In our case with IPA as the solvent, 1.7 W were sufficient to obtain a homogeneous spray. Tiny IPA droplets carry the dispersed nanostructures of AgNWs or ZnONPs.

The droplet diameter is not significantly dependent on the nozzle power. But the droplet diameter is a function of the nozzle frequency. The Lang formula (equation 4.2) is a good approach for calculating the expected droplet diameters obtained from the ultrasonic nozzle.

$$d = 0.34(\frac{8\pi\sigma}{\rho f^2})^{1/3} \quad [18] \tag{4.1}$$

d...	droplet diameter		
f...	frequency		= 120 kHz
σ...	surface tension	(IPA)	= 0.023 N/m [131]
ρ...	solvent density	(IPA)	= 0.785 g/mL (25 °C)

$$d_{IPA} \approx 0.34(\frac{8 * \pi * 23[gms^{-2}m^{-1}]}{0.785 * 10^{-6}[gm^3] * 120000^2[s^{-2}]})^{1/3} \approx 12.6 * 10^{-6}[m] \tag{4.2}$$

Taking surface tension and solvent density of 99.5 % IPA (CAS 67-63-0) and a frequency of 120 kHz into account, as released from the ultrasonic nozzle, droplet diameters of ≈ 12.6 µm are expected.

4.1.2.4 Flow rate

The flow rate for AgNW-deposition was attempted to be increased to minimize deposition-time. SEM images from depositions with 0.4 and 0.8 mL/min are shown in figure 4.4. It was observed that a flow rate of 0.8 mL/min leads to more stacked AgNWs. Regions of stacked AgNWs are encircled with dashed lines in figure 4.4 b). Low flow rates are reported to lead to more individual droplets, while higher flow rates increase the tendency of droplets to merge.[5] Excessive flow rate can cause bigger droplets, delayed drying and increased probability of agglomeration. Stacked AgNWs are not desired. For spraying AgNWs, 0.4 mL/min is optimal to obtain randomly distributed AgNWs without agglomerates. For ZnONPs, the flow rate was not further investigated, as 0.4 mL/min was proven to be sufficient.

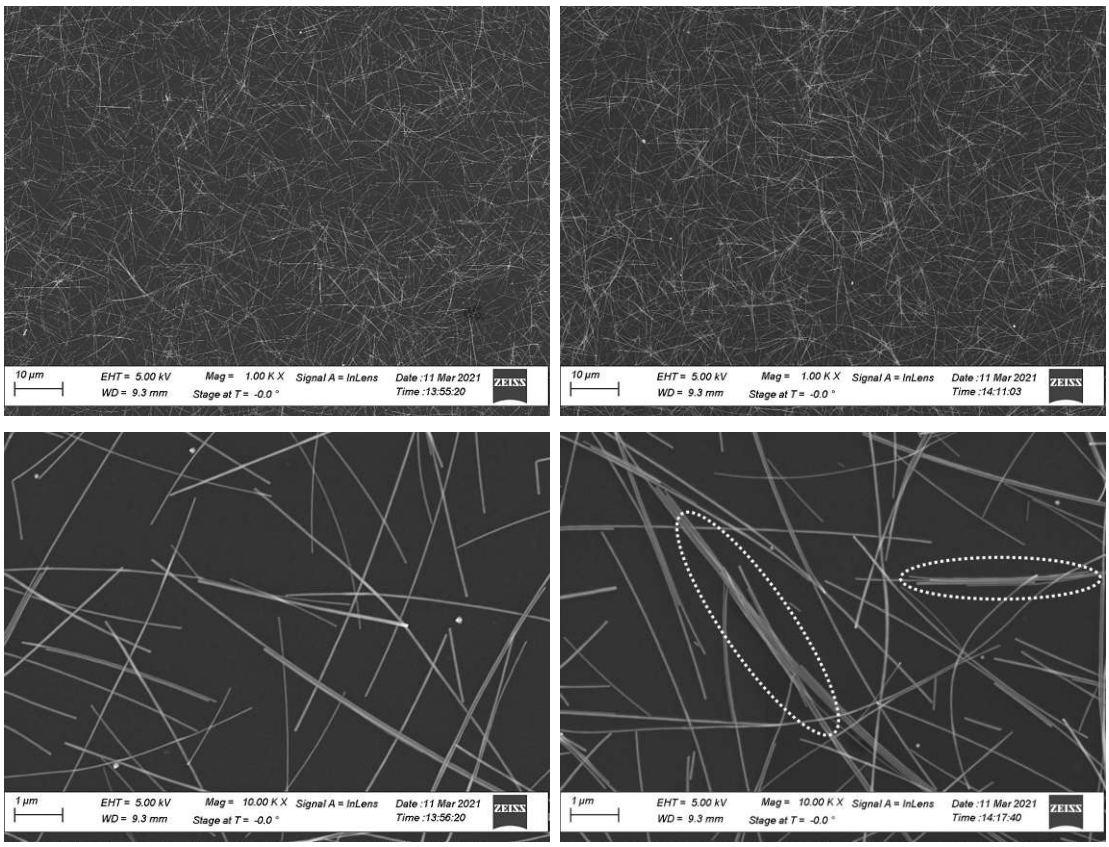

(a) 0.4 mL/min (b) 0.8 mL/min

Figure 4.4: **Flow rate:** The influence of the flow rate a) 0.4 mL/min and b) 0.8 mL/min is shown. Higher flow rate leads to a higher tendency for AgNW to stack, as indicated with dashed lines. These are not desired as they are possible hotspots in the device.

4.1.2.5 Shaping air

The shaping air pressure needs to be high enough to direct the stream towards the substrate. It can also force nanostructures to adhere to the substrate. In spray-pyrolysis low pressure is common to decrease droplet velocity and increase flight time. This usually assures proper crystal growth on the heated substrate.[50]) In cold spray (CS) for instance, another conventional spraying-technique, high kinetic energy from high pressure (up to 40 bar) causes high droplet velocities (up to 1200 m/s or more). As a consequence, microstructures deform.[132] Spray-coating of nanostructures is situated in between these two cases. USS uses a spray-pyrolysis set-up but deposits at higher pressures to form a wet layer. But USS uses lower pressure than CS to avoid deformation and repulsion of impinging nanostructures.

Figure 4.5 shows the influence of the shaping air on the amount of deposited material of ZnONPs on Si. A total number of 10 scans was sprayed at 100 °C substrate temperature with 1, 3 and 5 bar shaping air overpressure. Droplet velocity is a function of the carrier gas pressure.[133] Higher pressure causes higher droplet velocities and prevents ZnONPs from deflection by the air stream of the ventilation. Authors [133] state that increased pressure does not impact the droplet diameter. A slight dependence could, however, be observed. A total number of 20 droplets were measured from SEM images. Measured diameters are shown in table 4.2. Standard deviations are high, but there seems to be the tendency that higher shaping air pressure causes droplet diameters to decrease.

Table 4.2: **Initial coffee ring diameters:** Measured initial ring-diameters from SEM images at different shaping air pressures.

shaping air pressure	ring-diameters in SEM
1 bar	68.2 ± 24.2 µm
3 bar	49.3 ± 19.9 µm
5 bar	35.5 ± 21.3 µm

The calculated droplet diameter from the ultrasonic nozzle was calculated to be ≈ 12.6 µm. The diameters of coffee rings from impinged droplets are bigger. This can be linked to the spreading of IPA on PC and could further be linked to the shaping air pressure. The measured ring-diameters could suggest that lower shaping air increase the flight time and the probability of droplets to merge.

ZnONPs were sprayed with 3 bar to obtain a gentle stream while not lose too much material. A film of layered ZnONPs was built by adjusting the scan number. For AgNWs, 9 bar was proven sufficient, without deformation of the wires or severe material loss (figure 4.6). A shaping air of 9 bar is at the maximum for the set-up and was not further varied.

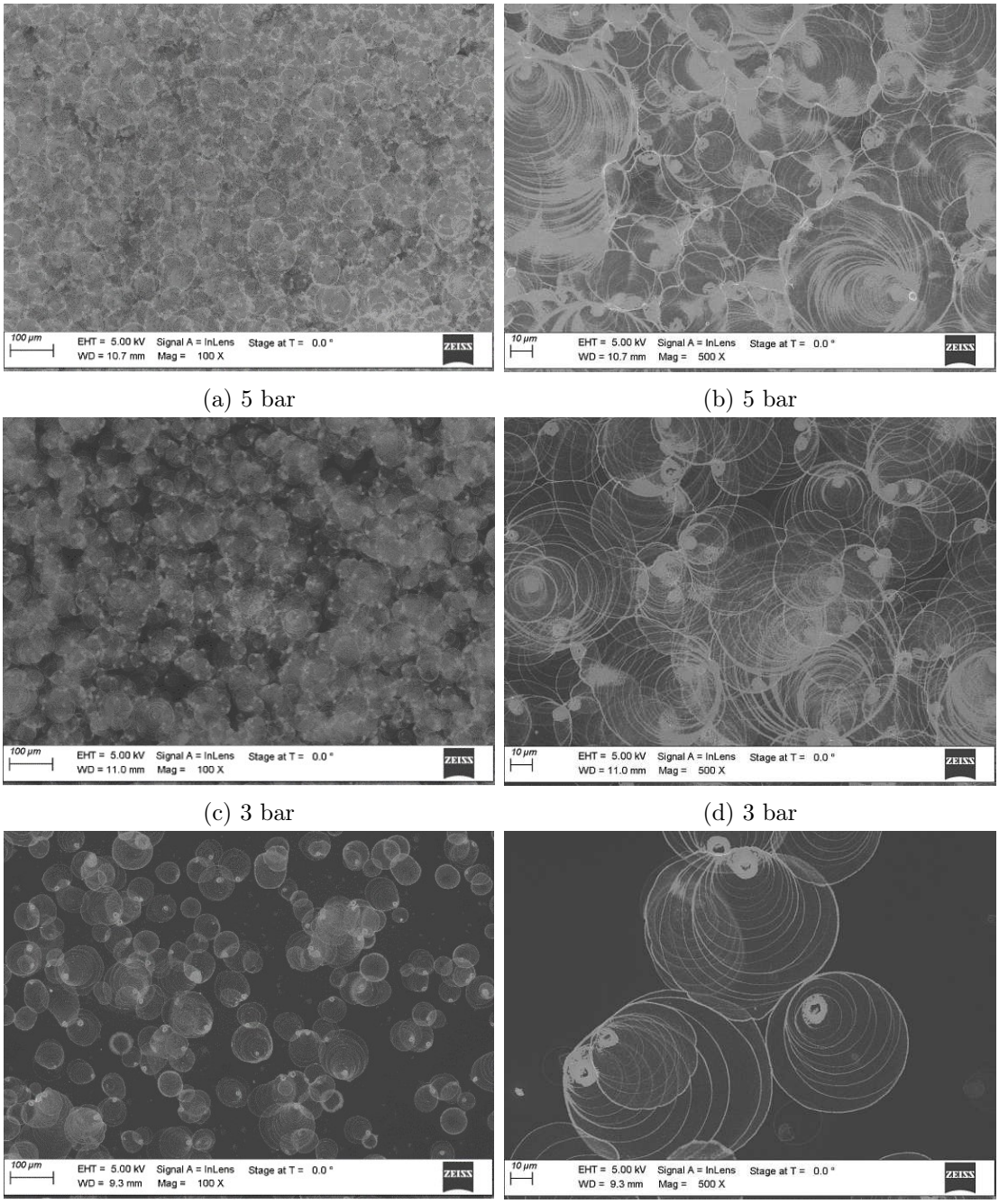

(a) 5 bar (b) 5 bar

(c) 3 bar (d) 3 bar

(e) 1 bar (f) 1 bar

Figure 4.5: **Shaping air influence on ZnONPs:** The shaping air significantly influences the amount of deposited material. Spraying 10 scans of ZnONPs on Si-substrates was performed with shaping air pressures of 5, 3 and 1 bar. Inner coffee ring deposits are due to elevated substrate temperature (100 °C) and were explained before.

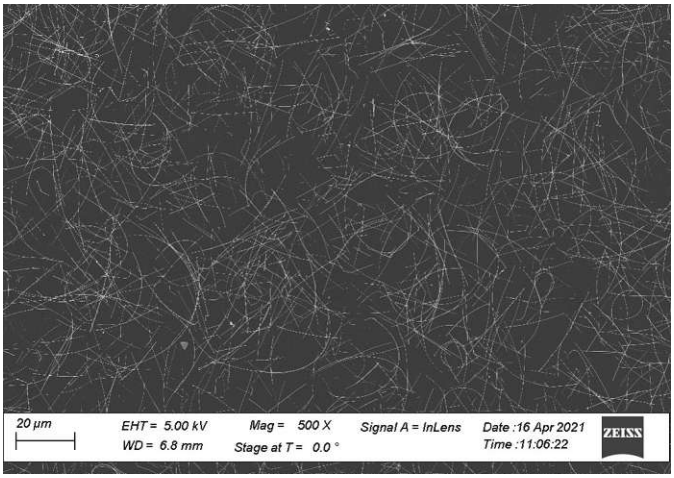

Figure 4.6: **Shaping air AgNW:** AgNWs were sprayed with 9 bar shaping air without deformation or significant material loss. AgNWs here are coated with PEDOT:PSS.

4.1.2.6 Sample positioning and overspray

Non-centered positioning causes conductivity variations due to AgNW-density variations. As a matter of precaution, the samples were placed under the exhaust outlet to avoid sidewards deflection of droplets and deformation of the spraying cone. The positioning of samples was optimized by spraying water on a steel plate and marking centered positions within wet areas. The overspray from actual depositions is hardly visible due to the coating's transparency. Spraying water made it possible to optimize the sample positioning systemetically.

A picture of sprayed water for five seconds on steel without any nozzle movement is shown in figure 4.7. This is a projection of the spraying cone. More water appears centered in the middle. The edge region of the cone inevitably causes gradients and overspray. Non-desired gradients in R_s at sample edges were reduced by increasing the spraying area. Taking more overspray into account assures that the center of the spraying cone interacts with the sample area. This reduces the standard deviation of R_s.

Overspray is evident in small-scale depositions and R_s gradients will assumably become less evident in industrial scales, due to lower spraying area to overspray ratios. A minor upscaling was realized from three samples 2.5 x 2.5 cm to two samples 5 x 5 cm, by increasing the spraying area. For that purpose, spraying areas of $\sim$33 cm^2 and $\sim$75 cm^2 were used. Fractions of these spraying areas are directed on surroundings. Oversprays of $\sim$43 % for 2.5 x 2.5 cm samples and $\sim$33 % for 5 x 5 cm were taken into account to be able to place the samples in central positions. For this minor upscaling, overspray could thus be reduced.

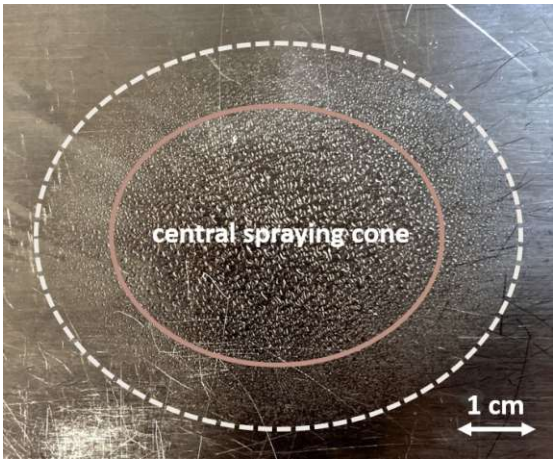

Figure 4.7: **Spraying cone:** Picture of the projected spraying cone. Water was sprayed on a steel plate for 5 seconds on one spot. A centered concentration of droplets is visible, supposedly caused by the vent trajecting a fraction of the stream.

4.1.2.7 Spraying pattern, spacing and speed

An arc spraying pattern was well investigated and employed for AgNW- and ZnONP-depositions. For the spacing between spraying lines and the spraying speed, the demands for AgNW- and ZnONP-depositions were different. AgNWs were deposited with narrow spacing and low speed, to build a network from minimal scan numbers to avoid 3D character of the deposits. ZnONPs were sprayed for embedding purposes. The spraying speed and spacing were increased to decrease deposition time per scan to build the layer from higher scan numbers.

4.1.2.8 Scan number

The desired film density is adjusted by the scan number. The outcome of the developed recipe for a film of sprayed ZnONPs on Si-substrate is shown in figure 4.8 with morphological and cross-sectional SEM images. Local inhomogeneities and non-sufficient coverage from coffee rings are compensated by higher scan numbers. Random rings layered in 30 scans lead to satisfying coverage for our purposes.

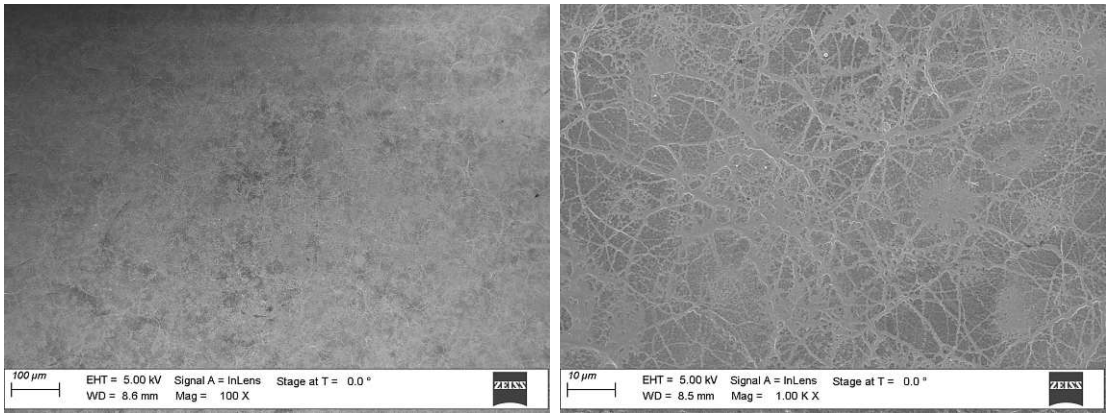

(a) (b)

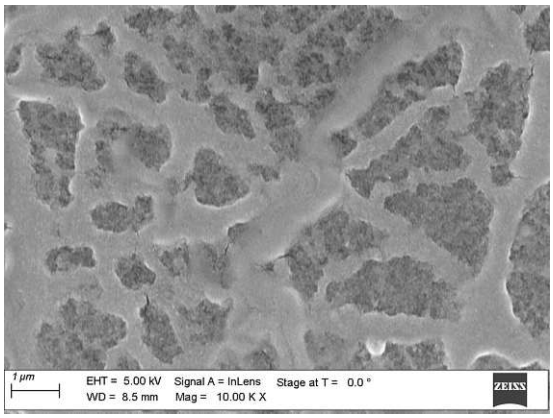

(c)

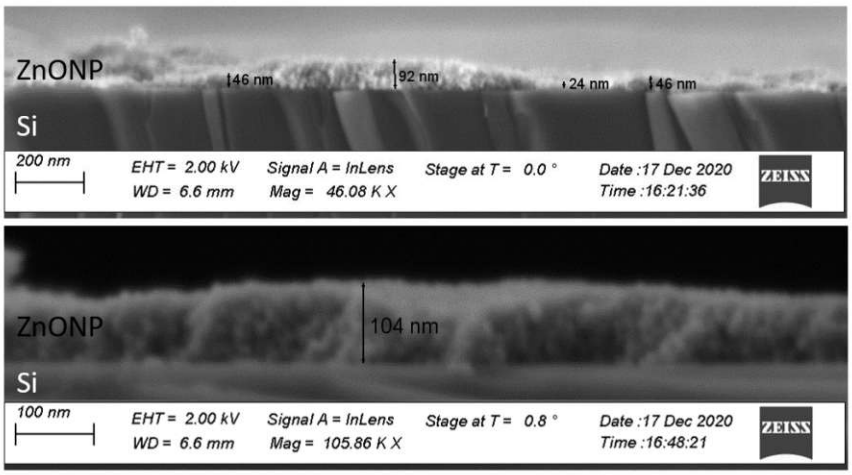

(d) cross sections with thickness measurements

Figure 4.8: **Final ZnONP-layer on Si-substrate:** Desired surface coverage could be accomplished by using 30 scans. This mostly compensates inhomogeneities from coffee-rings. The SEM image at 1000 x magnification show that ring formations are observed while the layer appears homogeneous over broad areas. Cross sections show that thicknesses vary as a result of overlapping coffee rings. This causes high surface roughness of sprayed ZnONPs.

4.1.3 Spray-coating of ZnONPs and AgNWs

Spray coating of elongated AgNWs and spherical ZnONPs is compared. The nanostructures are of very different shape. Based on discussed reasons, deposition recommendations are summarized in table 4.3.

Table 4.3: **Overview spray coating of nanostructures:** xperienced to follow listed desires for obtaining homogenous coatings of sprayed nanoparticles and nanowires.

	temp.	**dilution**	**flow rate**	**shaping air**	**speed**	**spacing**	**scans**
NPs	moderate	moderate	moderate	moderate	fast	wide	high
NWs	moderate	high	low	high	slow	narrow	low

Spray-coating of ZnONPs

Deposition of the ZnONPs is influenced by coffee rings. The pattern at 100 °C substrate temperature is based on inner coffee ring deposits. These result from subsequent stages of pinned contact lines. Further temperature increase was limited by the PC substrate, which would undergo deformation. Adjusting shaping air and scan number lead to sufficient surface coverage. Certain surface roughness is caused by ZnONP coffee rings which affects the optical properties, as discussed later.

Spray-coating of AgNWs

Random distribution of AgNWs is the premise for a conductive network. AgNWs are sensitive towards the flow rate. High flow rate leads to more stacked AgNWs (figure 4.4). Reproducibility of AgNW density is challenging. The solid content is required to be reproducible from batch to batch. AgNW sedimentation is fast and affects the reproducibility of solid contents from dilution. A quality control tool for AgNW suspensions was introduced by solution transmittance. High AR AgNWs are suppressed in diffusion within sessile droplets, the diffusion rate for large particle sizes is small.[32] Coffee rings are thus not an issue. It is although important, that the droplet size in USS is larger than the AgNW length. Otherwise, curved AgNWs are caused.[128] The substrate temperature does not significantly influence the film morphology of AgNWs.

4.1.4 Spin-coating of PEDOT:PSS

PEDOT:PSS was spin-coated at the current state of investigations. As the Clevios PH1000 formulation is viscous, further aqueous dilution was required for deposition. The formulation from the supplier was diluted 1:1 with DI water. The change of concentration resulted in coating thickness on AgNWs from 18 ± 3 nm (concentrated dispersion) to 10 ± 1 nm (50 vol. %). These were measured from SEM images, as shown in 4.9.

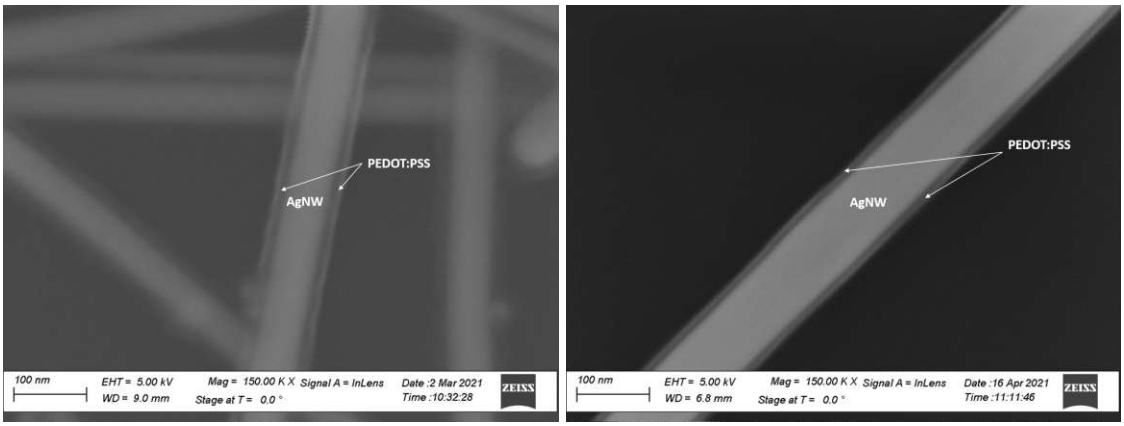

(a) concentrated PEDOT:PSS (b) 50 vol.% PEDOT:PSS

Figure 4.9: **Thickness PEDOT:PSS coating on AgNWs:** Concentrated PEDOT:PSS causes thicker coatings than 50 vol%. Observations were confirmed from SEM.

Samples prepared with concentrated PEDOT:PSS suffered from homogeneity and non sufficient coverage. Islands were visible with bare eye. Spinning speed of 4000 rpm and 50 vol. % diluted Clevios PH1000 resulted in the good results from optical and SEM investigations and was maintained.

4.2 Transparent electrode development

Two different AgNW-based TEs were developed. The three building blocks of ZnONP, AgNWs and PEDOT:PSS were stacked in PC/ZnONP/AgNW/ZnONP and PC/AgNW/PEDOT:PSS. These TEs were compared to uncoated PC/AgNW. Processing temperature never exceeded 100 °C. The top-layer of ZnONPs and PEDOT:PSS-coating on AgNWs were optimized as well as the AgNW-density. Samples of different AgNW-densities were obtained for characterization and percolation fitting.

4.2.1 AgNW-density optimization

The AgNW-density was varied by varying the dilution (1:5 to 1:40) and the scan number (2 to 5) of sprayed AgNW-layers. This way, samples from a gradient in AgNW-density were obtained. Samples of PC/ZnONP/AgNW/ZnONP of different AgNW-density are shown in figure 4.10. The gradient is apparent visually as well as from R_s (italic font) and total transmittance (underlined) values, as noted in the figure.

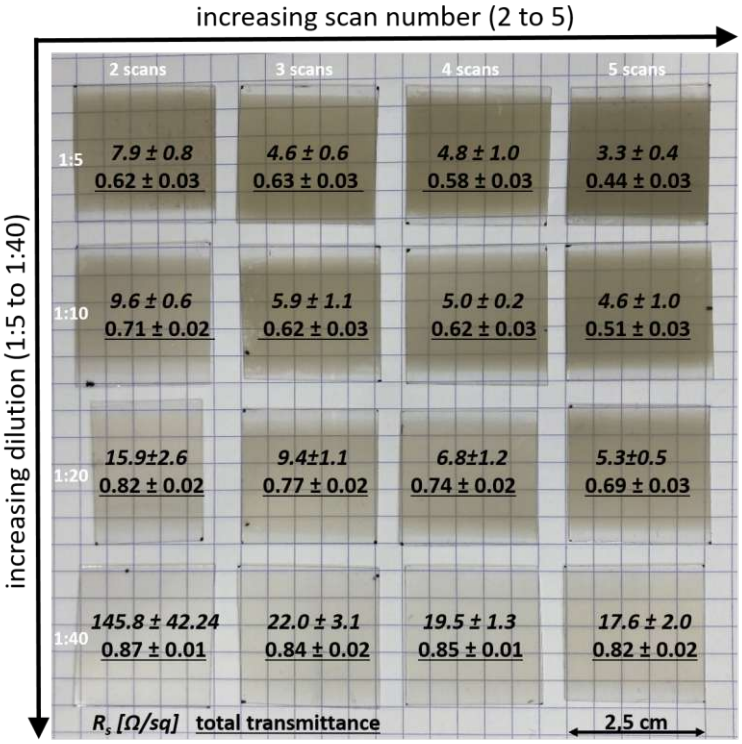

Figure 4.10: **Optical appearance of PC/ZnONP/AgNW/ZnONP:** Samples of different AgNW-density were obtained from varying AgNW-dilution and scan number. The two dimensional gradient in AgNW-density is visible with the naked eye and is also apparent in averaged total transmittance values from 500-800 nm (underlined) and sheet resistance from five spots (italic font), as indicated.

Figure 4.11 shows SEM images of the same samples as in figure 4.10. It shows the different densities of AgNW-networks. The different densities of randomly distributed AgNWs are causing a gradient in electrical as well as optical characteristics as indicated with noted values in figure 4.10.

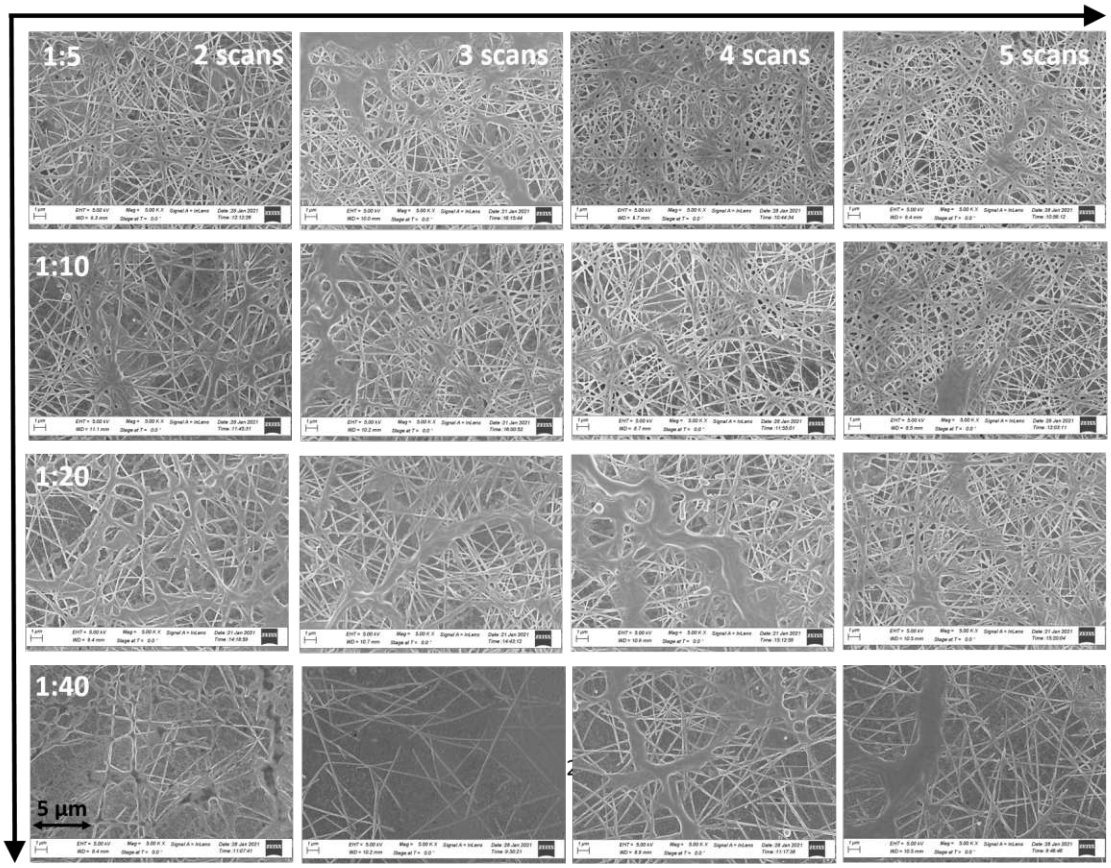

Figure 4.11: **SEM appearance of PC/ZnONP/AgNW/ZnONP:** Varied AgNW dilution and scan number caused samples of a two dimensional gradient in AgNW-density. The density is corresponding to a balance between R_s and T_{total}, as shown in figure 4.10 before.

4.2.2 Top-layer optimization

For PC/ZnONP/AgNW/ZnONP, the top-layer thickness was varied between 20 and 60 scans. The base layer of ZnONPs was held constant with 30 scans in the described recipe. The AgNW-network was the same for this set of samples (1:20 dilution, 3 scans). A top-layer of 20 scans ZnONPs did not fully cover the AgNWs and showed higher R_s. From figure 4.12 and 4.13 it is apparent that exceeding 30 scans for the top layer of ZnONPs is required to decrease R_s and avoid large parts of uncovered AgNWs. The R_s is constant and standard deviation is decreased when good coverage is obtained >30 scans ZnONPs.

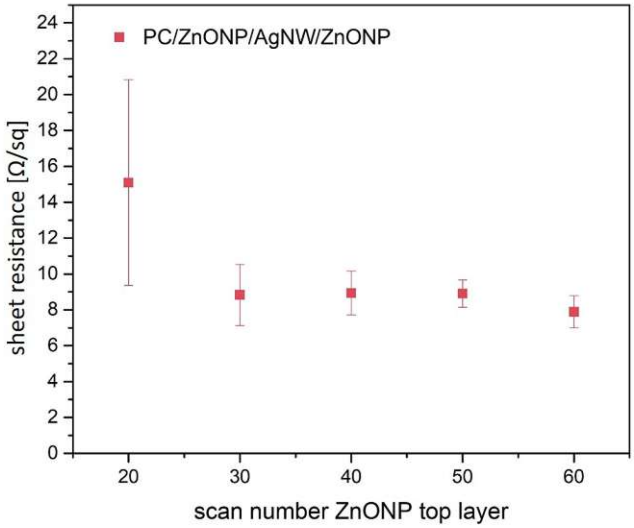

Figure 4.12: R_s **vs. ZnONP top-layer scan number:** The top-layer of ZnONPs is required to minimize R_s and fully cover and protect AgNWs.This is obtained by a minimum of 30 scans of ZnONPs in the described recipe.

The coverage appears sufficient from SEM for ZnONP top layers $>$ 30 scans. Figure 4.13 shows that increasing the top layer scan number gradually increases the apparent coating thickness. Base and top layers of 30 scans ZnONPs in PC/ZnONP/AgNW/ZnONP was considered appropriate for the developed TE.

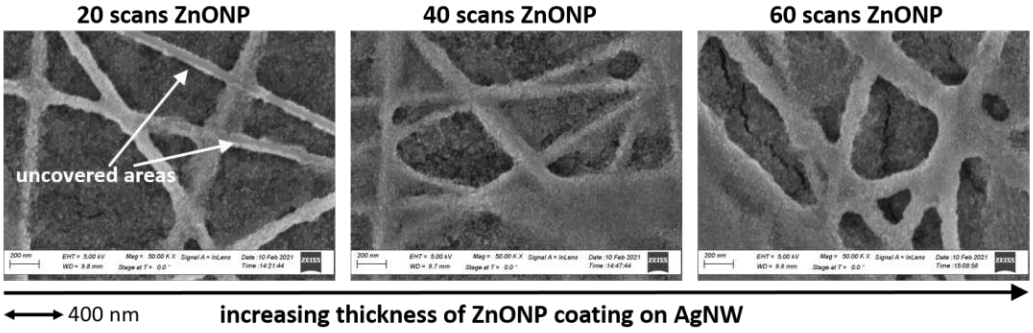

Figure 4.13: **PC/ZnONP/AgNW/ZnONP top-layer variation:** The ZnONP top-layer was varied 20 - 60 scans while the base-layer was constant. In accordance with figure 4.12, a minimum of 30 scans ZnONP top-layer was considered appropriate for R_s-decrease and full coverage of AgNWs.

The homogeneity and coverage of PEDOT:PSS in PC/AgNW/PEDOT:PSS was satisfying from 50 vol. % diluted suspension and spin coating with 4000 rpm. This resulted in a coating thickness of $\approx$ 10 nm on AgNWs as shown before in figure 4.9.

4.2.3 Developed TEs

The TEs were compared to uncoated PC/AgNW. Three series of samples, each of different AgNW-densities, were prepared for further investigations. The impact of the AgNW-density on TE-properties is studied in the following chapter. SEM images of representative samples are depicted in figure 4.14 below.

Uncovered areas of PC cause charging in the electron beam, visible in a different appearance in SEM. Sprayed ZnONPs cause a lower contrast in SEM with a secondary electron detector. Ring-shaped concentrated regions of ZnONPs are visible, linkable to the coffee ring effect. PEDOT:PSS is a very thin coating on AgNWs. A homogeneous coverage of PEDOT:PSS on AgNWs can be concluded from no charging appearance in SEM in uncovered PC areas, due to the low conductivity of PEDOT:PSS.

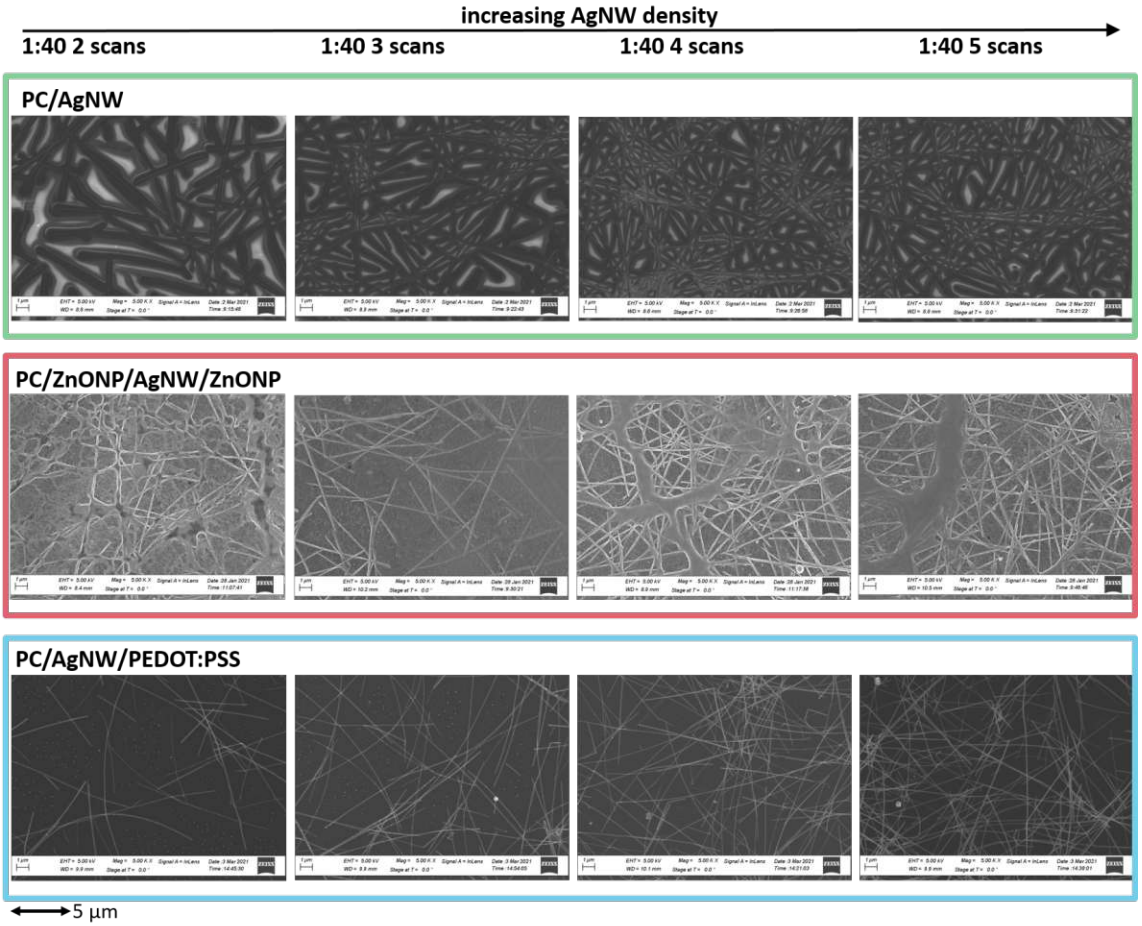

Figure 4.14: **SEM images of developed TEs:** Developed TEs are compared to uncovered AgNWs on PC. Concentrated regions of ZnONPs are visible. Uncovered PC causes charging which disappears by PEDOT:PSS-coating.

Figure 4.15 shows the optical appearance of representative 2.5 cm x 2.5 cm samples of PC/ZnONP/AgNW/ZnONP (T_{total} (550 nm) = 0.79, R_s=8.2 ± 1.0 Ω/sq) and PC/AgNW/PEDOT:PSS (T_{total} (550 nm) = 0.81, R_s=9.2 ± 1.2 Ω/sq) compared to the PC-substrate.

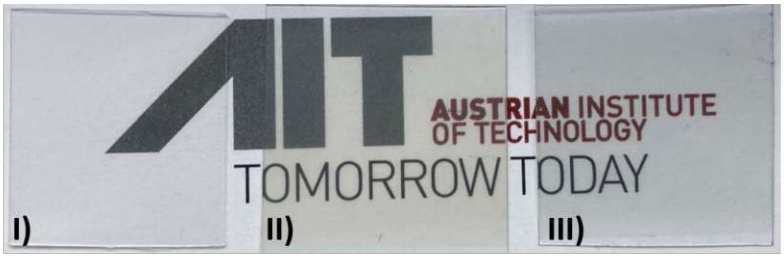

Figure 4.15: **Photo of developed TEs:** Photo of coated AgNW-networks compared to I) PC-substrate. ZnONPs cause a yellowish colour in II) PC/ZnONP/AgNW/ZnONP. The PEDOT:PSS causes a blueish tone in III) PC/AgNW/PEDOT:PSS. Good optical transmittance in the visible is combined with $R_s \approx 10$ Ω/sq in both TEs.

The total transmittance spectra of these samples are shown in figure 4.16. The yellowish appearance of PC/ZnONP/AgNW/ZnONP in figure 4.15 can be explained by a slight transmittance drop < 700 nm. Apart from that, rather constant transmittance is observed in all shown spectra over a broad range in the visible light range.

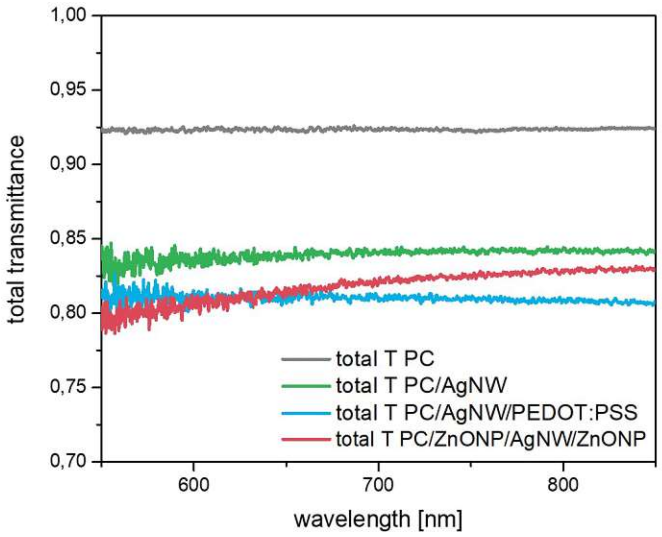

Figure 4.16: **Transmittance of developed TEs:** The TEs show constant total transmittance over a broad range in the visible light spectrum. ZnONPs cause a minor transmittance drop < 700 nm, explaining a slightly yellowish appearance in figure 4.15.

Typically, electrical and optical properties are counter-active. To visualize this, it is common to plot the transmittance as a function of the sheet resistance.[84, 134, 135]

Figure 4.17 shows a) T_{normal} and b) T_{total} as a function of the R_s for uncoated AgNWs (green), AgNWs in ZnONPs (pink) and coated with PEDOT:PSS (blue). The curves have the expected and for AgNW-networks typical shape. High transmittance and low sheet resistance is a challenging combination, as the transmittance drops significantly below a certain R_s value.

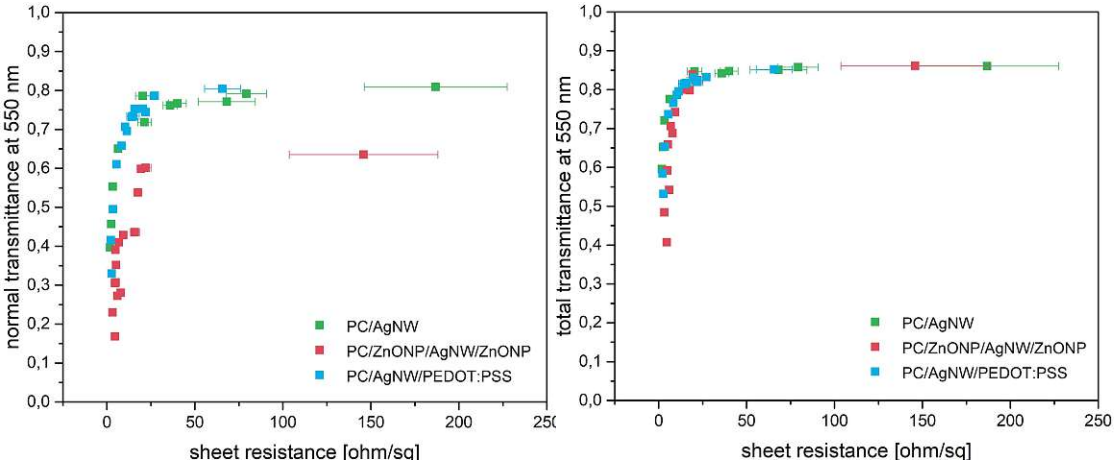

(a) normal transmittance (b) total transmittance

Figure 4.17: **Sheet resistance vs. transmittance:** The plots show the typical shape for AgNW-networks, whereas R_s drops significantly below certain value. AgNW-coatings influence optical properties, most significantly T_{normal}, where the curve shifts towards lower transmittance values, due to lost intensity to scattering effects. T_{total} on the other hand, is not significantly affected by the ZnONPs.

It is noticable from figure 4.17, that there is significant difference between T_{normal} and T_{total}, which is caused by the ZnONPs. For same R_s values, the T_{normal} for PC/ZnONP/AgNW/ZnONP is decreased in comparison to PC/AgNW or PC/AgNW/PEDOT:PSS. The PEDOT:PSS-coating on the other hand, mostly conserves the optical properties of uncoated AgNWs. For T_{total}, all curves are mostly overlapping in this representation. This difference between T_{total} and T_{normal} is linked to light scattering and can be quantified in values for the optical haze, as discussed later.

It is further apparent from figure 4.17 that there is a general relationship between optical and electrical properties. Both, electrical and optical behaviour are dependent on the AgNW-density. This behaviour is followingly described with percolation models. PEDOT:PSS itself is conductive and ZnONPs are transparent conductive oxides, when doped. The contribution of additional materials to the AgNW-composite conductivity was in this context of interest.

4.3 Percolating AgNW-networks

Sprayed AgNW-networks are percolating systems, working as a fully interconnected system when a critical coverage ϕ_c is exceeded. Optical properties and most prominently the electrical properties, are dependent on the AgNW-density, which is represented by the AgNW surface coverage ϕ_s. The phenomenon is typical for AgNW-based TEs. The influence of PEDOT:PSS- and ZnONP-coating on the percolating behaviour of AgNW-networks is studied. The developed TEs PC/ZnONP/AgNW/ZnONP and PC/AgNW/PEDOT:PSS are in this context compared to a reference of uncoated PC/AgNW.

4.3.1 Electrical dependence on the AgNW-density

Electrical percolation is described with a power law, as explained in chapter 2. The power law is again shown in equation 4.3. Research effort is put into further describing the material factor M, the critical density ϕ_c and the critical exponent t.

$$R_s(\phi_s) = \frac{M}{(\phi_s - \phi_c)^t} \quad [84] \tag{4.3}$$

Based on Khanarian et al. [84], the ϕ_c is calculated to ϕ_c=0.04 for the used AgNW-dimensions of L=$9,2 \pm 2.8\mu m$ and D=$58.3 \pm 15.2nm$ (Sigma60 in table 4.1). Using the averaged D- and L-values in equation 4.4 below, the AgNW-networks should theoretically become percolating for an electrical current when ϕ_s is exceeding 0.04.

$$\phi_{c,theory} \approx \frac{18 * D}{\pi * L} \approx \frac{18}{\pi} \frac{58.3nm}{9200nm} \approx 0.04 \tag{4.4}$$

4.3.2 Optical dependence on the AgNW-density

It was further shown in chapter 2 that the transmittance is kown to drop linearly with a certain slope β with increasing AgNW-density.

$$T = T_{substr}(1 - \beta\phi_s) \quad [92] \tag{4.5}$$

The T is the composite transmittance and T_{substr} is the transmittance of the substrate.

4.3.3 Electro-optical properties

As both, electrical and optical properties, are dependent on ϕ_s, attempts are made to link electro-optical dependences in an expression for T as a function of R_s. An equation for $T(R_s)$ can be used to fit the dependences shown in figure 4.17 before. For that purpose, a similar attempt to Bellet et al. [94], to combine electrical properties (equation 4.3) and optical properties (equation 4.5), follows.

Equation 4.5 can be rewritten to express ϕ_s, as shown in equation 4.6.

$$\phi_s = \frac{1 - \frac{T}{T_{substr}}}{\beta} \tag{4.6}$$

This is inserted in equation 4.3 and leads to equation 4.7.

$$R_s = \frac{M}{(\frac{1-\frac{T}{T_{substr}}}{\beta} - \phi_c)^t} \tag{4.7}$$

Rearrangements result in $T(R_s)$, which is shown in equation 4.8.

$$T(R_s) = T_{substr}(1 - \beta((\frac{M}{R_s})^{\frac{1}{t}} + \phi_c)) \tag{4.8}$$

The used total transmittance spectra of uncoated and coated AgNW-networks of different ϕ_s as well as the spectra of the substrates without AgNWs are depicted in figure 4.18. To fit experimental data to the introduced equations for electrical, optical and electro-optical properties, T_{total} values at 550 nm were used.

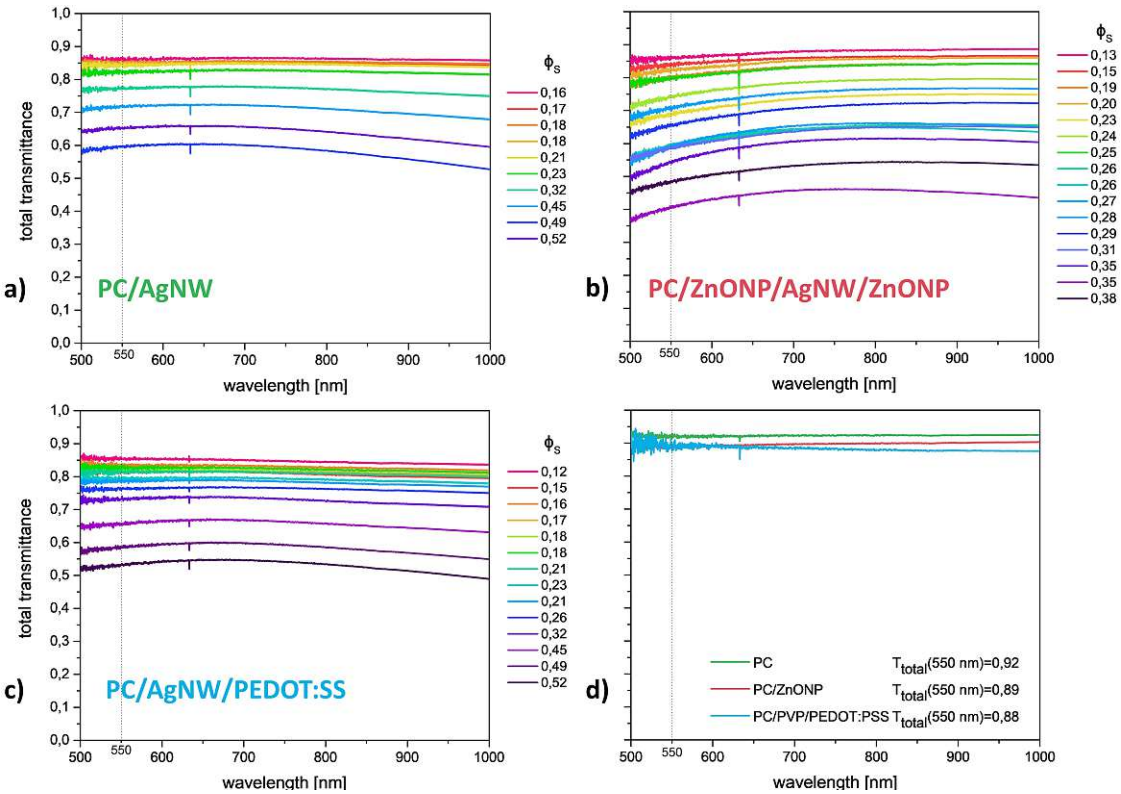

Figure 4.18: **Total transmittance spectra:** T_{total} values at 550 nm were used to fit the dependences shown in figure 4.19. Graphs a-c show T_{total} spectra of the TEs of different ϕ_s. In d), the substrate spectra (T_{substr}) without AgNWs are shown.

4.3.4 Percolation modelling

Figure 4.19 shows the fitted experimental data from samples of different ϕ_s of uncoated PC/AgNW and the developed TEs. Highlighted parameters were fitted to 1.) electrical (equation 4.3) and 2.) optical dependences on ϕ_s (equation 4.5), which are accordingly noted in the figure. The obtained parameters were tested to describe the 3.) electro-optical dependence of R_s on T_{total} (equation 4.8).

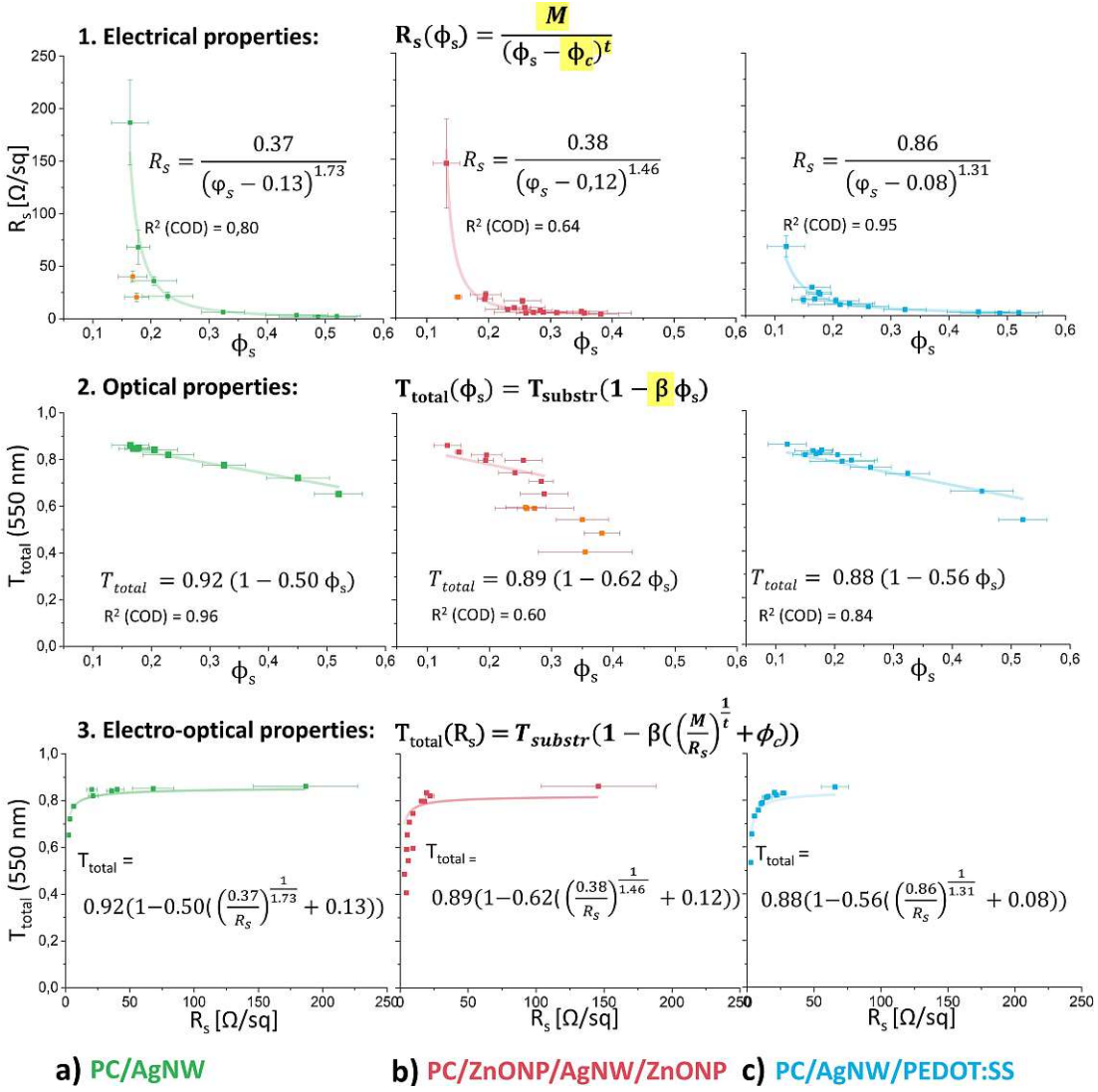

Figure 4.19: **Percolation modelling:** Highlighted parameters were determined from fitting with stated equations (equation 4.3 and 4.5). Obtained fitting parameters were tested to fit $R_s(T)$, based on equation 4.8. The R_s were determined from five measured spots, T_{total} was taken at 550 nm and the ϕ_s was extracted from 4-5 SEM images. The uncoated reference PC/AgNW is compared to coated AgNWs.

The error bars result from the following measurement routines and equal the standard deviations from the average. The ϕ_s were averaged from 4-5 SEM images and the R_s were averaged from five measured spots. The T_{total} values were taken at 550 nm. The critical exponent t, the material factor M and the critical AgNW-density ϕ_c were extracted from the power law $R_s(\phi_s)$. The β was determined from $T_{total}(R_s)$. High-ϕ_s samples in PC/ZnONP/AgNW/ZnONP (orange in figure 4.19) were excluded for fitting $T_{total}(\phi_s)$, due to discrepancies from linearity at high AgNW-densities. Higher standard deviations and lower regressions in the plots from PC/ZnONP/AgNW/ZnONP samples result from ϕ_s determination from lower contrast SEM images. Dependences of T_{total} on R_s are described with the extracted parameters as fixed values. Good agreement is obtained, which supports the accuracy of the theoretical parameters.

The parameters obtained from fittings in figure 4.19 are summarized in table 4.4.

Table 4.4: **Percolation modelling results:** The extracted optical parameter β, critical exponent t, material factor M and critical AgNW surface fraction ϕ_c are summarized.

	β	t	M	ϕ_c
PC/AgNW	0.50 ±0.02	1.73 ±0.48	0.37 ±0.15	0.13 ±0.03
PC/ZnONP/AgNW/ZnONP	0.62 ±0.08	1.46 ±0.45	0.38 ±0.28	0.12 ±0.02
PC/AgNW/PEDOT:PSS	0.56 ±0.04	1.31 ±0.26	0.86 ±0.17	0.08 ±0.02

In regard to these theoretical parameters, the following conclusions are drawn.

4.3.4.1 Reference network: PC/AgNW

From uncoated PC/AgNW we can conclude that predicted ϕ_c is higher than the theoretical value of 0.04. Khanarian et al. [84] assume intimate and optimized contact between wires so that R_j can be neglected. They assume that the current cannot be blocked at junctions of overlapping AgNWs. This makes the ϕ_c in reality larger than expected from the calculation shown in equation 4.4.

4.3.4.2 AgNW-networks coated with ZnONPs or PEDOT:PSS

For coated AgNWs, the ϕ_c values are reduced when compared to PC/AgNW. But the ϕ_c are still above 0.04. A prominent decrease is caused by PEDOT:PSS. The free-standing coatings of PEDOT:PSS and ZnONPs have low lateral conductivity ($R_s \approx$ M Ω/sq). PEDOT:PSS is a thin layer and not optimized towards high conductivity, no acid- or DMSO-treatment was performed. ZnONPs are inefficient for charge carrier transport due to their small size (D $\approx$ 15 nm) and absence of doping. It is considered that their contribution to the lateral charge carrier transport is not significant. For ZnONPs, the

contribution can even be considered negligible. But they can mitigate the charge carrier transfer between wires over small distances. This is equivalent to lowering the R_j.

Having this in mind, the effective lowering of ϕ_c is linked to lowering R_j, which is further linked to following different effects or a combination of them.

a) The acidity of PEDOT:PSS might partly destroy the insulating shell of AgNWs. This causes a more intimate contact.
b) PEDOT:PSS, and to a lesser extent ZnONPs, help to transfer charge carriers at small distances between AgNWs at the junction proximity.
c) AgNWs are exposed to additional heat treatment at 100 °C during deposition of the coating, which may partly pyrolyze insulating surfactants.

So, we assume that the effective impact of the coating is the lowering of the junction-resistance, while the lateral resistance is not modified. Lateral resistance decrease would be visible in negative ϕ_c values, indicating that additional paths are created to enable the current to flow through the ZnONPs or PEDOT:PSS. But this is not the case. The ϕ_c are approaching $\phi_{c,theory}$, but still $\phi_c > \phi_{c,theory}$. The R_j has the most pronounced effect on the conductivity of sparse networks, close to the percolation threshold.[93] This is reflected in the shown data by enhanced resistance decline for coated AgNW-TE samples of low ϕ_s and observed shifts in ϕ_c.

Further, the decrease in the resistance ratio $\frac{R_j}{R_w}$ through the coating with additional materials may influence the critical exponent t, as shown by Fata et al.[93] For reduced R_j, the t is expected to assume lower values. This effect is observed in the data from fitting $R_s(\phi_s)$ and supports the assumed decrease of R_j by coating AgNW-networks.

From the model by Khanarian et al. [84], the material factor is further linked to a C value. The C is defined as the deviation from bulk silver resistivity (ρ). When C=1, the resistivity of AgNWs is said to equal the resistivity of bulk silver. The C could thus be linked to R_w. But the equation can only be applied, when R_j is assumed to be negligible and when the t is considered to equal the theoretical value of 1.3 for 2D-networks. A dependency on R_j, which apparently affects t and M, is not considered.

A dependency of C, t and M on the resistance ratio $\frac{R_j}{R_w}$ would thus be required in percolation equations to describe coated AgNW-networks of different $\frac{R_j}{R_w}$.

4.3.5 Effects of coating AgNW-networks

Modelling has shown that the critical AgNW-density is smaller for coated AgNW-networks. Hence, the percolating regime is achieved earlier by coating the AgNWs. The R_j is assumed to be reduced by PEDOT:PSS- or ZnONP-coating, due to their vertical resistance decrease at junctions of AgNWs.

Coating of AgNW-networks have the following effects on models from the literature.

1) AgNWs are effectively longer in the model by Khanarian et al. [84].
2) The charge transport probability is higher in the model by Lagrange et al. [92]
3) The junction areas for charge carrier transport are enlarged, which decreases R_j.

These effects result from shifted $\frac{R_j}{R_w}$ in coated AgNW-networks. The coatings on AgNWs lower ϕ_c and decrease t, which supports that R_j is lowered. The resistance ratio $\frac{R_j}{R_w}$ is thus shifted to lower values. This effect is sketched in figure 4.20 below.

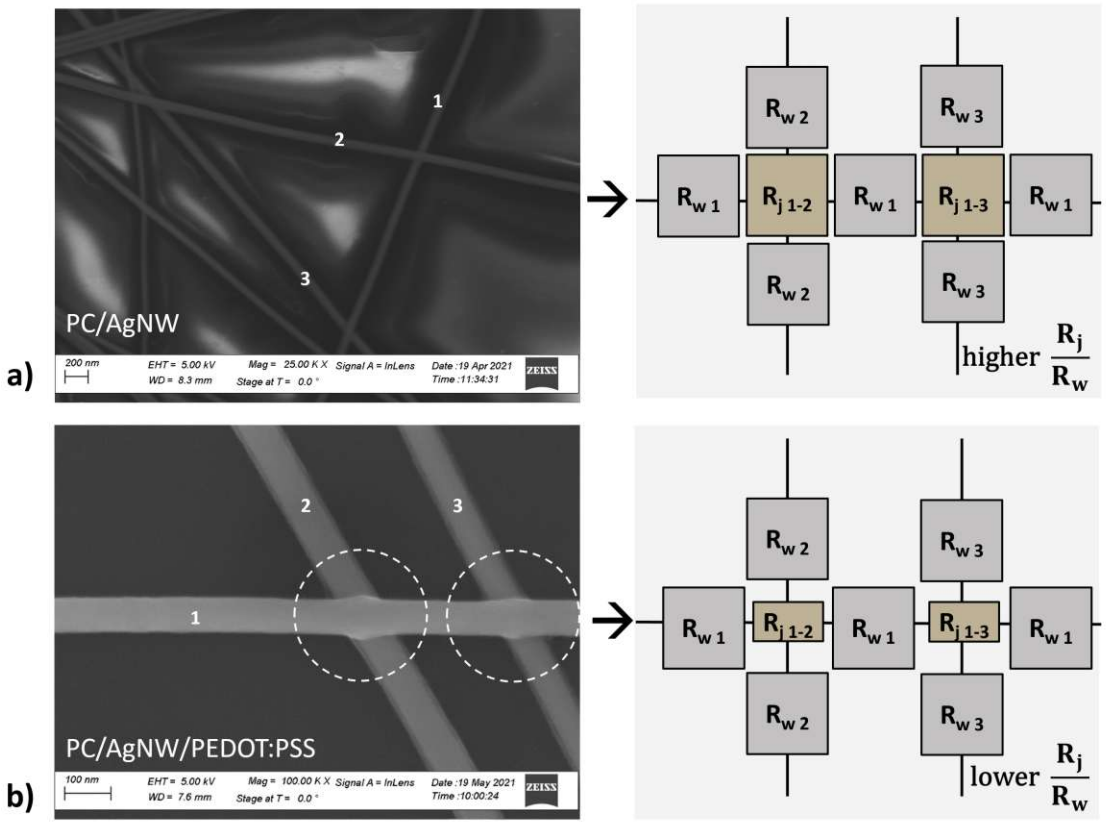

Figure 4.20: **Reduced R_j by coating AgNWs:** Junction resistances are reduced by coating AgNW-networks with PEDOT:PSS or ZnONP. The coatings lower the critical AgNW-density. Charge carriers at junctions are transported more efficiently.

It can be imagined as a subway-effect. Usually a subway network is fast. But if one line is blocked, slower bus lines are beneficial for the mobility. The slow lines are not required when the line-density is high. But approaching a critical line-density, slow lines improve the mobility significantly due to an improvement of weak points in the network.

4.4 Haze

Haze is an optical property that is either desired to be high or low, depending on the application. Dependences of the haze on the roughness, the AgNW-density and the two coatings of either ZnONPs or PEDOT:PSS, are discussed.

4.4.1 Dependence of haze on the roughness

Haze (H) is the ratio of diffuse transmittance (T_{total} - T_{normal}) per T_{total}. It is mostly determined by the surface roughness and further dependent on the refractive indices of the material and atmosphere and also, the wavelength of the incident light.[136, 137] This relationship is shown in equation 4.9.

$$H = 1 - exp(-(2\pi(n_1 - n_2) * \frac{Rq}{\lambda})^2) \quad [136, 137] \tag{4.9}$$

Rq...	root mean square surface roughness
λ...	wavelength of the incident light
n_1 and n_2...	refractive indices of the media on either side of the scattering interface

Figure 4.22 shows the surface height profiles of coated AgNW-networks in comparison to uncoated PC/AgNW. ZnONP-layers cause periodic peaks in the height profiles and increase the surface roughness significantly. PEDOT:PSS-coating does not evidently change the AgNW-morphology and mostly conserves the roughness of PC/AgNW.

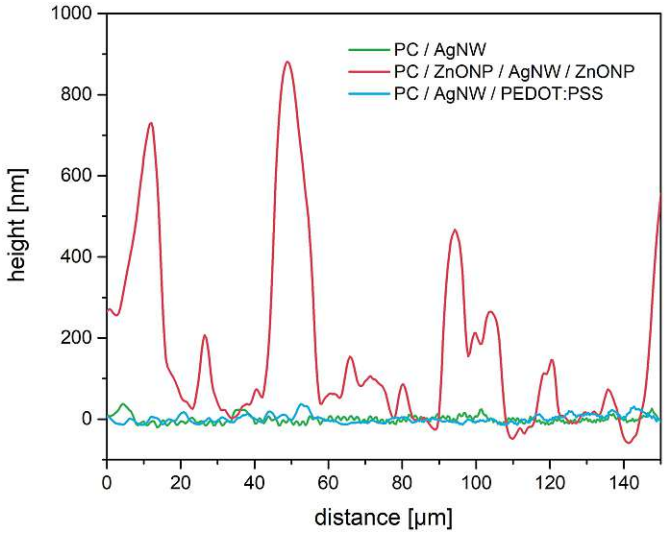

Figure 4.21: **Surface height profiles:** ZnONP-coating increases the surface roughness.

The root mean square surface roughness values (Rq) were extracted and averaged from three lines per sample. The results are listed in table 4.5.

Table 4.5: **Surface roughness:** Haze is determined by the surface roughness. The root mean square surface roughness values (Rq) of the developed TEs and the PC/AgNW reference are shown.

	Rq
PC/AgNW	7.7 ± 0.9 nm
PC/ZnONP/AgNW/ZnONP	154 ± 5 nm
PC/AgNW/PEDOT:PSS	7.8 ± 0.4 nm

The increased surface roughness from sprayed ZnONP-coating results from the coffee ring effect (see section 4.1). SEM images of PC/ZnONP/AgNW/ZnONP and PC/AgNW/PEDOT:PSS are shown in figure 4.22. Concentrated regions of ZnONPs result from nanoparticles that diffuse to the edges of the sessile droplets during spray deposition. These regions are marked with white arrows. Surface profilometry has confirmed that the coffee rings of ZnONPs increase the roughness, when combined with AgNW-networks on PC-substrate. Due to the increased roughness, the T_{normal} of PC/ZnONP/AgNW/ZnONP is decreased in comparison to PC/AgNW or PC/AgNW/PEDOT:PSS, as shown in figure 4.17 before. As a result, the haze ($H=\frac{T_{total}-T_{normal}}{T_{total}}$) is increased by coating AgNW-networks with ZnONPs. The effect is discussed in more detail by separate discussion of the dependence of haze on the AgNW-density and the ZnONP-coating thickness.

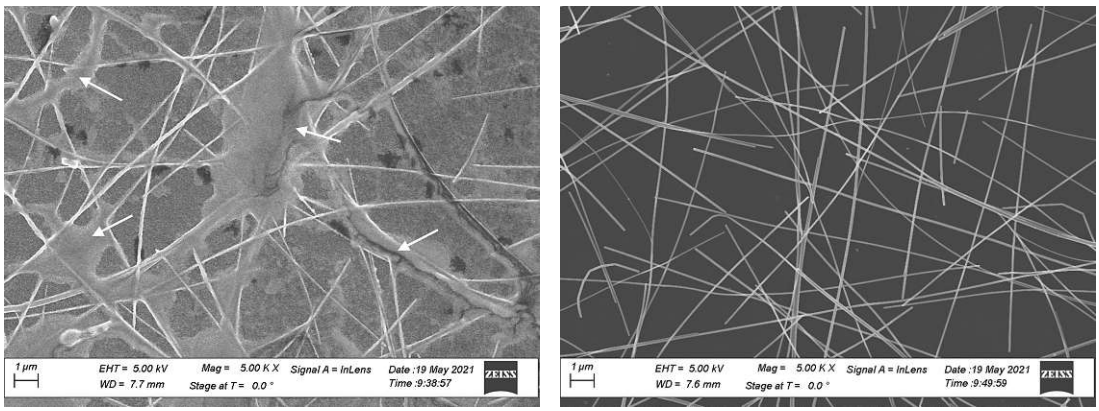

(a) PC/ZnONP/AgNW/ZnONP (b) PC/AgNW/PEDOT:PSS

Figure 4.22: **Surface morphology:** SEM images are shown. a) Regions of concentrated ZnONPs result from coffee rings. b) PEDOT:PSS is homogeneously distributed. These observations affect the roughness, as confirmed by profilometry. This further affects the haze.

4.4.2 Dependence of haze on the AgNW-density

Studies have interrelated haze and AgNW-diameters (D).[134, 84] The D is important to estimate the haze of AgNW-networks. A diameter increase of AgNWs from D=30 nm to D=100 nm is predicted to increase the haze up to 8 times.[134] In this work, AgNWs of

same dimensions have been used and influences of the additional coatings were studied. Lagrange et al. [92] plotted haze as a function of the AgNW-density for different AgNW-AR values and showed that the haze is linearly dependent on ϕ_s with a slope δ. But they could not report a dependence of haze on the AgNW-AR, when ϕ_s is considered. For coated AgNWs of same AR, an additional factor (m) is hereinafter introduced. The linear dependence of H on ϕ_s is shown in equation 4.10. The data was fitted to this equation, as depicted in figure 4.23. The m and δ were free fitting parameters. Results from figure 4.23 are listed in table 4.6.

$$H(\phi_s) = m + \delta * \phi_s \tag{4.10}$$

m... extrapolated haze at ϕ_s=0 δ... haze increase per ϕ_s increase

Table 4.6: **Results from fitting H(ϕ_s):** Fitting parameters from figure 4.23 to equation 4.10 are listed for developed TEs in comparison to the reference PC/AgNW.

	m	δ
PC/AgNW	0.0 ±0.02	0.6 ±0.07
PC/ZnONP/AgNW/ZnONP	0.1 ±0.04	1.3 ±0.16
PC/AgNW/PEDOT:PSS	0.0 ±0.02	0.6 ±0.08

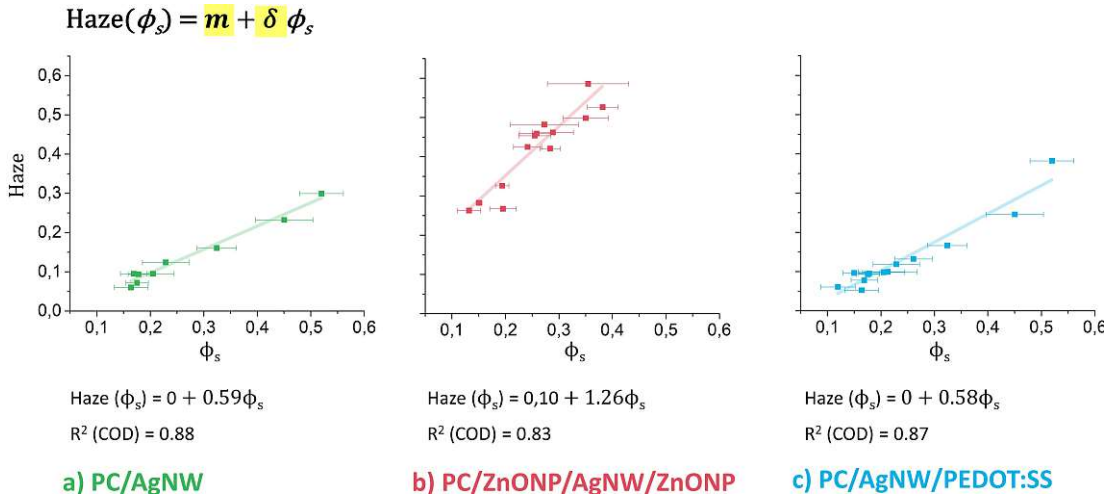

Figure 4.23: **H(ϕ_s):** Haze as a function of ϕ_s is shown and fitted to equation 4.10. Sprayed layers of ZnONPs significantly increase haze when combined with AgNW networks.

It is shown that the haze-parameters can be affected by coatings of AgNW-networks. The m is a parameter for the extrapolated haze at ϕ_s=0 and refers to a haze contribution

that results from the additional coatings. PC/AgNW and PC/AgNW/PEDOT:PSS do not show significant haze at ϕ_s=0, thus m=0. In PC/ZnONP/AgNW/ZnONP m $\neq$ 0 is due to the surface roughness from spray-coated ZnONPs. PC/ZnONP was measured H (550 nm) = 0.15 which is in approximate agreement with the extracted m = 0.1. The δ is similar for PC/AgNW and PC/AgNW/PEDOT:PSS, but significantly increased by ZnONPs. The increase in haze with increasing ϕ_s is steeper for ZnONP-coating. Sprayed layers of ZnONPs thus offer a way to increase the haze, as further adjustable with the top-layer thickness of ZnONPs.

4.4.3 Dependence of haze on the sprayed ZnONP-coating thickness

The haze is affected by the single layers that build PC/ZnONP/AgNW/ZnONP and PC/AgNW/PEDOT:PSS. The PEDOT:PSS is expected to fill gaps and slightly decrease roughness and haze, as reported in literature.[138] But the polymer layer would be required to be thicker to observe this effect. ZnONP layers on the contrary, are shown to increase the haze, which is dependent on the thickness of the top layer of sprayed ZnONPs.

Figure 4.24 shows that the haze of PC/ZnONP/AgNW/ZnONP can be partly controlled by the scan number of the sprayed ZnONP-coating. The data was collected during optimization of the ZnONP top-layer thickness. A top-layer scan number of 30 scans was considered appropriate, due to reduced R_s (see figure 4.12). More scans of ZnONP-coating subsequently increase the haze. Mehra et al. [139] introduced ZnO-nanopyramids layers to control haze and showed the relevance of haze-tuning layers. The controlled morphology of sprayed ZnONP-layers is in this regard interesting.

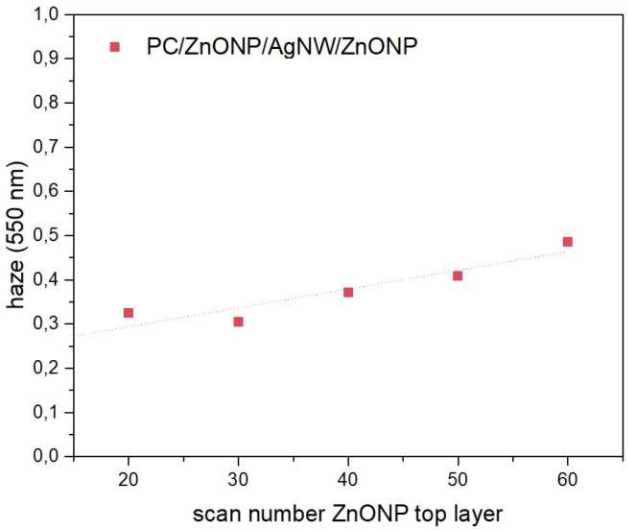

Figure 4.24: **Haze-tuning with sprayed ZnONPs:** The top layer scan number of ZnONPs increases the haze. A minimum of 30 scans is required to minimize R_s (see figure 4.12). More layers of ZnONPs subsequently increase the haze.

4.5 Application of developed transparent electrodes

Properties of developed TEs are summarized and the stability at ambient and elevated temperature conditions is discussed. Finally, application as transparent flexible heaters serve as a proof of concept.

4.5.1 Properties of developed TEs

The main properties of developed TEs are summarized in table 4.7. The TE PC/ZnONP/AgNW/ZnONP would be convenient for photovoltaics or OLED applications, due to the higher haze. This improves the interaction of incident light with the material. The TE PC/AgNW/PEDOT:PSS would be appropriate for display applications, touch screens, smart windows or transparent heater devices due to the lower haze, which does not disturb the vision.

Table 4.7: **Transparent electrode properties:** Obtained properties of developed low temperature processed TEs are shown.

	R_s	**T**	**H**
PC/ZnONP/AgNW/ZnONP	$\approx 10\ \Omega$/sq	≈ 0.8	≈ 0.3
PC/AgNW/PEDOT:PSS	$\approx 10\ \Omega$/sq	≈ 0.8	≈ 0.1

The TEs were deposited on PC, which is a heat-sensitive and flexible substrate. The composite-TEs are good in terms of their low cost and ambient processing at 100 °C from solution. Further, no toxic materials are used and upscalability is expected to be easy by ultrasonic spray-coating. The developed TEs are therefore interesting alternatives to common transparent conductive oxides like ITO.

4.5.2 Figure of merit by Haacke

Figures of Merit (FOM) are convenient to rank the performance of materials. High FOM_{Haacke} express high T and low R_s. In figure 4.25, the FOM_{Haacke} ($T_{total} = 550$ nm) as a function of ϕ_s are shown, bell-shaped data sets are observed.

The data suggests that the coatings are beneficial for low ϕ_s. For high ϕ_s, uncoated AgNWs show higher FOM_{Haacke} values. This observation is linkable to results from percolation modelling. It was shown that the coatings have a prominent impact on the electrical properties of sparse AgNW-networks and that lower ϕ_c are obtained by coating AgNW-networks. The coatings shift the maximal FOM_{Haacke} values to lower AgNW-densities. Both coatings lead to highest FOM_{Haacke} at $\phi_s \approx 0.2$. The AgNW-PEDOT:PSS-TEs show higher maximal FOM_{Haacke} than the AgNW-ZnONP-TEs.

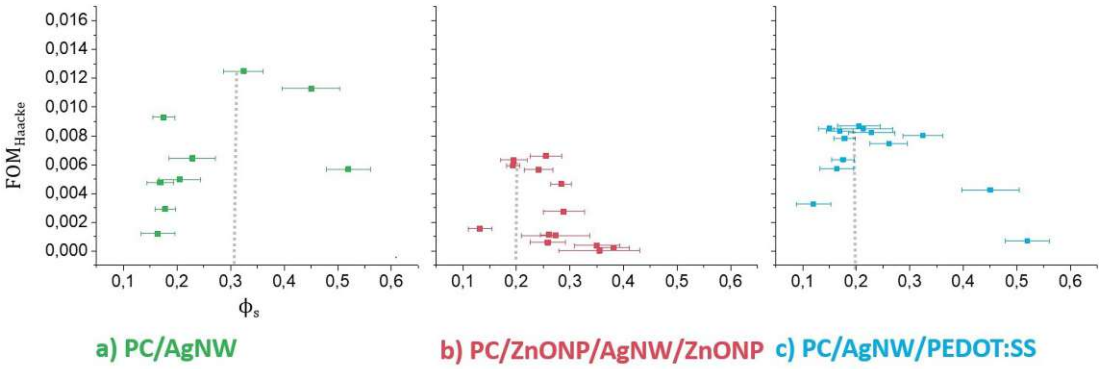

Figure 4.25: **Figure of merit by Haacke et al. [37]:** This FOM is common to illustrate high T_{total} and low R_s in high FOM values. Maximal values are shifted to lower ϕ_s by the additional coatings on AgNW-networks.

4.5.3 Thermal stability

The influence of ZnONP- and PEDOT:PSS-coating on the electrical stability of AgNW-networks at elevated temperature was of interest, because these conditions are relevant for flexible transparent heaters. Samples of higher ϕ_s ($R_s \approx 10\ \Omega/sq$) and lower ϕ_s ($R_s \approx 20\ \Omega/sq$) were prepared. The samples were stored at 70 °C in ambient atmosphere for one month. The R_s was monitored as a function of time, as shown in figure 4.26. The PC/AgNW-samples served as a reference for coated AgNW-networks.

PC/AgNW of low-ϕ_s did electrically degrade over time, as stored at 70 °C. The R_s and standard deviations are increasing from spatial differences in R_s. In SEM, deformations are visible in high- and low-ϕ_s samples of PC/AgNW. After one month, the microscopic degradations are not yet affecting the working order of high-ϕ_s networks. A low quantity of disturbed electrical pathways have a bigger impact, when AgNW-density is lower and closer to ϕ_c. High-ϕ_s networks can buffer more degraded wires, before the network breaks down. The microscopic degradation progress of PC/AgNW at 70 °C is depicted in figure 4.27. Nanoparticles were formed within one week on uncoated AgNW surfaces. Ag migration is well studied in literature.[111] Silver oxidizes and migrates as Ag^+ before it is deposited elsewhere in form of Ag nanoparticles (AgNP). The AgNPs grew bigger over time. After approximately three weeks, distorted junctions were found. This duration matches the increasing R_s in figure 4.26. No such AgNW-formation or R_s-increase was observed in reference samples of PC/AgNW stored in inert gas atmosphere at room temperature for one month.

It is apparent from literature that silver migration and AgNW degradation mechanisms can be very complex, particulary, when coated with PEDOT:PSS due to the polymer's acidic and hygroscopic nature.[140, 112, 117, 141, 142] But it can be concluded that ZnONPs and PEDOT:PSS are both sufficient to prevent premature electrical degradation of AgNWs at stated elevated temperature conditions.

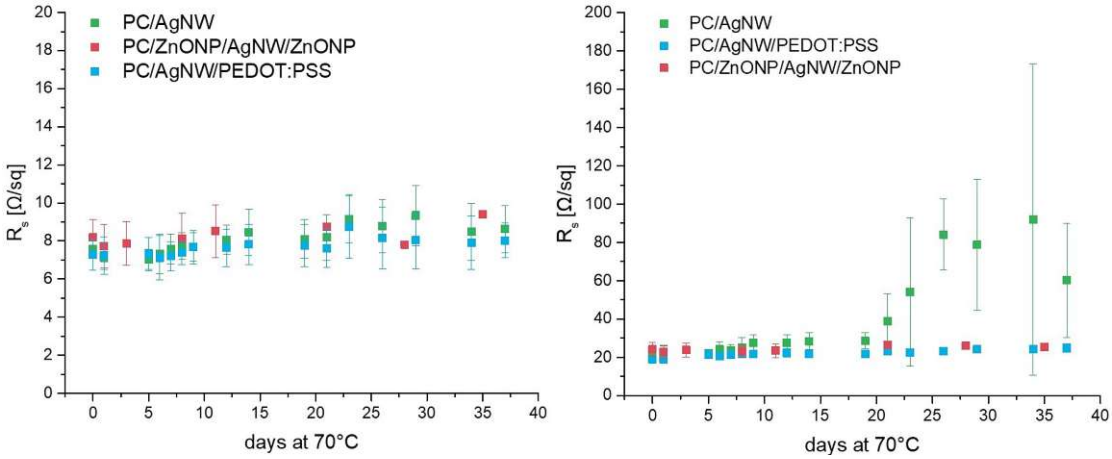

(a) high-density AgNW-TEs ($R_s < 10\ \Omega$/sq) (b) low-density AgNW-TEs ($R_s \approx 20\ \Omega$/sq)

Figure 4.26: **AgNW stability at 70°C:** Shown are R_s of AgNWs coated with ZnONP (pink), PEDOT:PSS (blue) and uncoated (green), stored at 70 °C and monitored over the duration of one month. Lower AgNW-density lead to an earlier break-down. Uncoated AgNWs of lower AgNW-density began to electrically degrade after approximately three weeks.

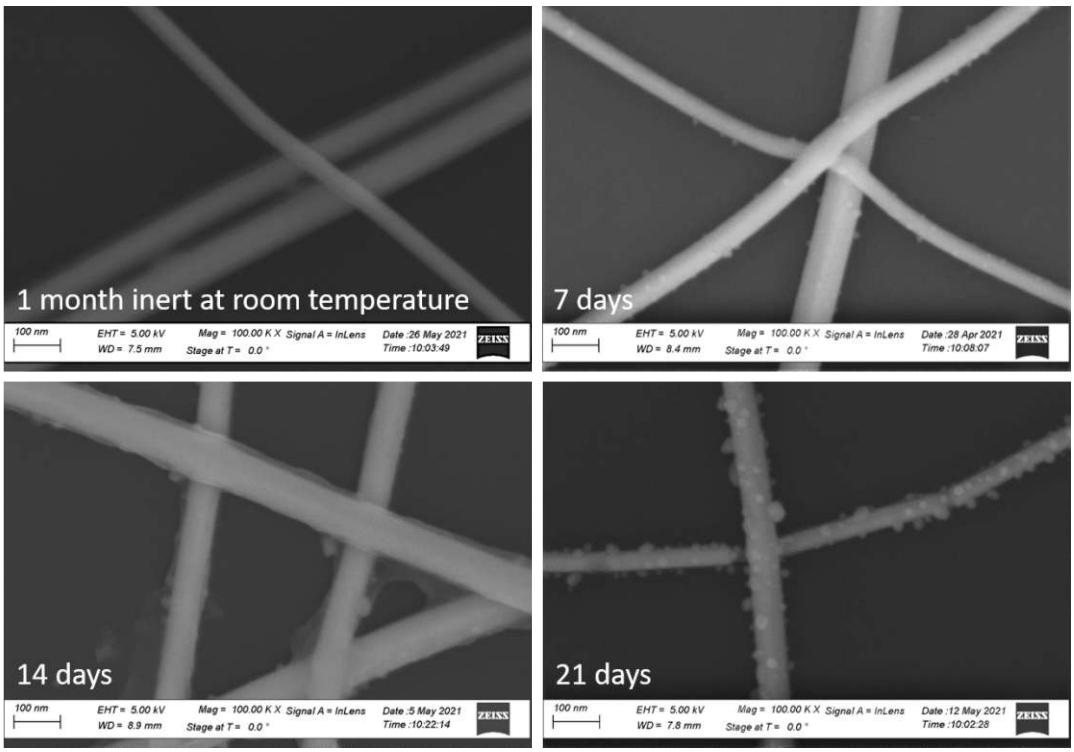

Figure 4.27: **PC/AgNW at 70°C:** Complementary SEM images to figure 4.26 show progressive degradation of uncoated AgNWs. Protrusions grew bigger over time. No protrusions were observed in the reference sample stored at inert conditions.

4.5.4 Flexible transparent heater

Resistive heating is based on Joule's law (equation 2.9), as explained before and as shown in equation 4.11.

$$\mathbf{\Delta T} = \frac{\mathbf{t}}{\mathbf{C} * \mathbf{m} * \mathbf{R}} * \mathbf{U^2} \tag{4.11}$$

T...	temperature	t...	time	R...	resistance
U...	voltage	m...	sample mass	C...	specific heat capacity

The temperature increase ($\triangle T_{steady}$) is thus controlled by the applied voltage and affected by the heat capacity, mass and resistance of the sample. The R_s of the samples are similar. Different behaviour in heating can thus be linked to the additional coatings. Figure 4.28 shows the temperature increases from room temperature, obtained by applied, stated voltages. It shows that both developed TEs can be used as sufficient transparent heaters. Observations from figure 4.28 are summarized in table 4.8. Further, figure 4.28 b) shows seven temperature cycles from switching ON/OFF 3.5 V. The temperature increase is in both TEs is reliable and reproducible.

Table 4.8: **Heating results:** Applied voltages generate following temperature increases. Heat generation follows equation 2.11. Corresponding graphs are given in figure 4.28

	voltage [V]	**resistance** [Ω]	$\triangle T_{steady}$ [°C]
PC/ZnONP/AgNW/ZnONP	1.0	12.2	≈ 6
(R_s = 11 Ω/sq)	2.0	12.4	≈ 25
	3.0	12.4	≈ 50
	3.5	12.7	≈ 65
PC/AgNW/PEDOT:PSS	1.0	12.6	≈ 9
(R_s = 12 Ω/sq)	2.0	12.9	≈ 30
	3.0	13.5	≈ 60
	3.5	13.9	≈ 80

Higher $\triangle T_{steady}$ is obtained with PC/AgNW/PEDOT:PSS, which can be linked to the different heat capacity and mass quantity of the additional materials. PEDOT:PSS is applied as a very thin coating. ZnONPs are used as base layer and coating. It is assumed, that the ZnONPs in PC/ZnONP/AgNW/ZnONP absorb more heat than PEDOT:PSS in PC/AgNW/PEDOT:PSS.

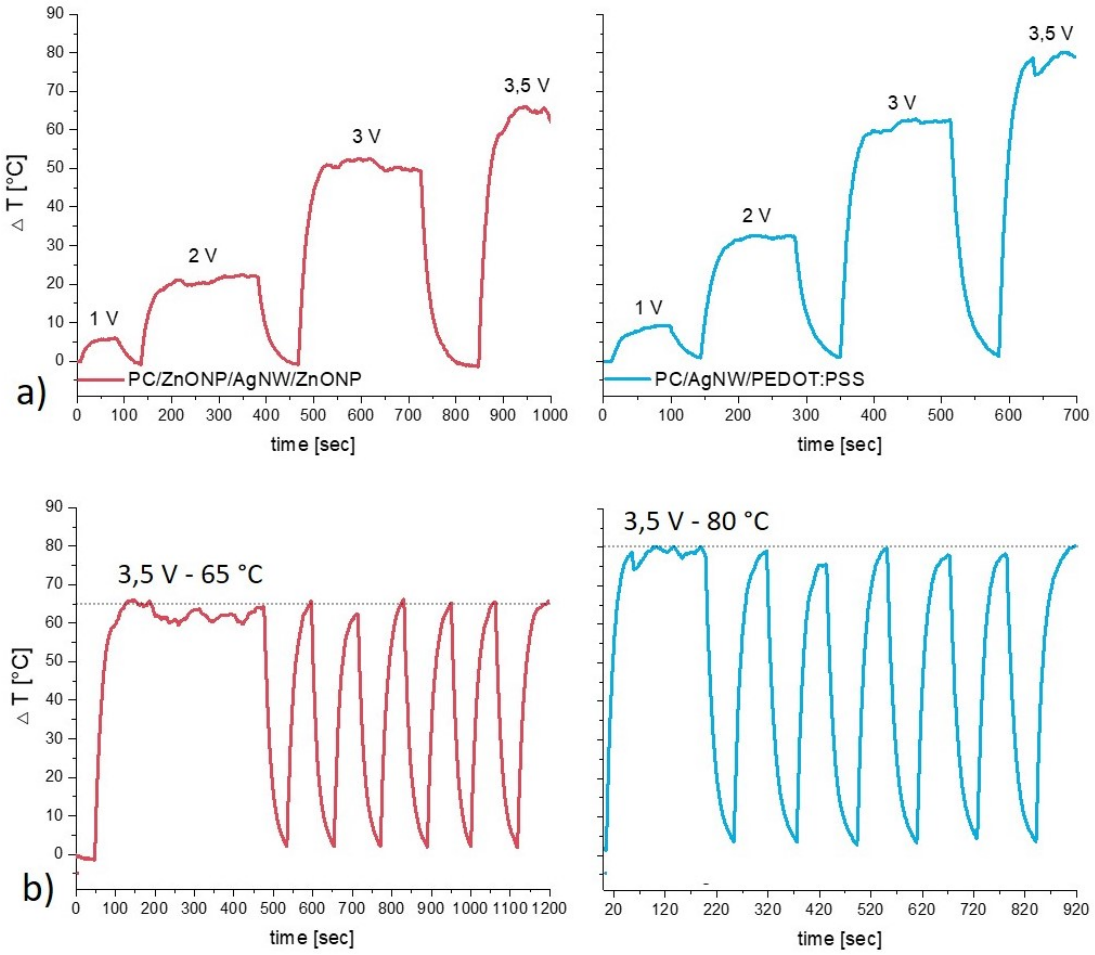

Figure 4.28: **Heating:** Applied voltages induce heating of both developed TEs of coated AgNW-networks with PEDOT:PSS and ZnONPs. The emissivity ϵ of PC is taken 0.8 and resistances were measured, as stated in table 4.8. Temperature increases from room temperature to the steady-state temperatures as a function of time are shown in a). Graphs in b) show seven heating cycles by switching ON/OFF 3.5 V, which indicates that the heating is reproducible and reliable.

It can be concluded that from 3.5 V, PC/ZnONP/AgNW/ZnONP delivers a temperature increase of + 65 °C while PC/AgNW/PEDOT:PSS increases the surface temperature by + 80 °C. Both temperature increases are reproducible from thermal cycling. The heating could be obtained from common 3.6 V batteries.

5 Conclusions

Transparent electrodes of AgNW-networks coated with PEDOT:PSS or ZnONPs were developed on flexible and low-cost polycarbonate (PC) substrate. The spraying parameters for deposition of ZnONPs and AgNWs from suspensions were thoroughly studied. All materials were processed from solution and at 100°C. The developed TEs have high optical transmittance (T_{total} including the substrate $\approx$ 0.8) and low sheet resistance ($R_s \approx 10\ \Omega$/sq). The TEs differ in their optical scattering properties. The AgNW-PEDOT:PSS-TEs have low haze (H $\approx$ 0.1), whereas the haze for AgNW-ZnONP-TEs is increased (H $\approx$ 0.3). The increased haze for the electrodes with ZnONP-layers is due to the increased roughness and can be controlled through the ultrasonic spray-coating parameters. The roughness results from the coffee ring effect. A prominent positive impact in electrical properties was obtained from coating sparse AgNW-networks with PEDOT:PSS due to the decrease of the junction-resistance. The effect is less prominent in the TEs employing ZnONPs. The decrease in junction-resistance is supported by theoretical values extracted from percolation modelling. Coatings decrease the critical AgNW-density (ϕ_c (PC/AgNW) $\approx$ 0.13, ϕ_c (PC/ZnONP/AgNW/ZnONP) $\approx$ 0.12 and ϕ_c (PC/AgNW/PEDOT:PSS) $\approx$ 0.08). At the same time, the critical exponent t is also decreased (t (PC/AgNW) $\approx$ 1.7, t (PC/ZnONP/AgNW/ZnONP) $\approx$ 1.5 and t (PC/AgNW/PEDOT:PSS) $\approx$ 1.3). These decreased ϕ_c and t values indicate a shift of the junction-resistance to lower values. The percolation regime is thus reached at lower AgNW-density by coatings. Coated AgNW-networks were shown to be suitable transparent heaters of increased stability, compared to bare AgNWs on PC. The coatings protect the AgNW-networks from premature electrical degradation, when stored in ambient atmosphere at 70 °C for one month. Developed TEs were successfully used as heaters. With an applied voltage of 3.5 V, a steady-state temperature increase of + 65°C was obtained from PC/ZnONP/AgNW/ZnONP ($R_s = 11\ \Omega$/sq) and + 80°C from PC/AgNW/PEDOT:PSS ($R_s = 12\ \Omega$/sq). But the developed TEs could find several other applications, apart from transparent heaters. The PC/ZnONP/AgNW/ZnONP would be particularly suitable for applications that target high haze (photovoltaics, light emitting diodes, etc.) while the PC/AgNW/PEDOT:PSS is convenient for low-haze applications (displays, smart windows, etc.). The insights gained in percolation modelling and ultrasonic spray-coating contribute to more understanding of coated AgNW-networks, of coffee ring formation from spray-coating and the design of AgNW-composites for industrial-scale and low-cost processing of transparent electrodes on flexible substrates.

6 Outlook

The developed TEs could be implemented in other devices, apart from transparent heaters and the presented building blocks could be used in other transparent electrode architectures and on other substrates, various combinations would be possible. Further, the dilution of commercial Heraeus Clevios PH 1000 was shown to be sufficient to obtain homogeneous coverage by spin-coating, this dilution is thus recommended for ultrasonic spray-coating of PEDOT:PSS at 100 °C. Spray-coating of PEDOT:PSS is well reported in literature [143, 144, 145, 146, 147] and should be manageable in a straight-forward manner. Also, ultrasonic spray-coating of ZnONPs could open more ways to gradually control scattering properties. Using other substrates, decreasing the flow rate, increasing the substrate temperature, doing systematic wetting studies and further investigations of the patterns of inner coffee ring deposits from spray-coated ZnONPs would be interesting.

Appendix

Table 6.1: **Twelve principles for greener chemistry:** The principles were introduced by Anastas and Warner [3] as guidelines.

1. **Prevention**
2. **Atom Economy**
3. **Less Hazardous Chemical Synthesis**
4. **Designing Safer Chemicals**
5. **Safer Solvents and Auxiliaries**
6. **Design for Energy Efficiency**
7. **Use of Renewable Feedstocks**
8. **Reduce Derivatives**
9. **Catalysis**
10. **Design for Degradation**
11. **Real-Time Analysis for Pollution Prevention**
12. **Inherently Safer Chemistry for Accident Prevention**

List of Abbreviations

AgNW Silver Nanowires

AR Aspect ratio

amd Areal Mass Densitry

CNT Carbon Nanotube

CS Cold Spray

CVD Chemical Vapor Deposition

DMD Dielectric Metal Dielectric

DMSO Dimethylsulfoxide

EDX Energy Dispersive X-Ray Analysis

EG Ethyleneglycol

FoM Figure of Merit

FT-IR Fourier-transform Infrared Spectroscopy

H Haze

ICRD Inner Coffee Ring Deposits

IPA Isopropanol

OLED Organic Light Emitting Diode

PANI Polyaniline

PC Polycarbonate

PEDOT:PSS Poly(3,4-ethylendioxythiophene)-poly(styrenesulfonate)

PVD Physical Vapor Deposition

PVP Poly(vinylpyrrolidone)

s*acro* :$\phi_s\phi_s$ *sacro* :ϕ_sAgNW surface coverage

R2R Roll to Roll

R_s Sheet resistance

R_s Junction resistance

R_s Wire resistance

RT Room temperature

SC Spin Coating

SEM Scanning Electron Microscopy

SP Spray Pyrolysis

TCF Transparent Conductive Film

TCM Transparent Conductive Material

TCO Transparent Conductive Oxide

TE Transparent Electrode

TH Transparent Heater

T Transmittance

US Ultrasonic

USC Ultrasonic Spray Coating

USP Ultrasonic Spray Pyrolysis

UV Ultraviolet light region

Vis Visible light region

XRD X-ray Diffraction

ZnONP Zinc Oxide Nanoparticles

Bibliography

[1] Douglas Adams. *The hitchhiker's guide to the galaxy*. First American edition. New York : Harmony Books, 1980. ©1979, 1980.

[2] United Nations Conference of the Parties, 2015.

[3] P.T. Anastas and J.C. Warner. *Green Chemistry: Theory and Practice*. Oxford University Press, 1998.

[4] Lado Filipovic, Siegfried Selberherr, Giorgio C Mutinati, Elise Brunet, Stephan Steinhauer, Anton Köck, Jordi Teva, Jochen Kraft, Jörg Siegert, and Franz Schrank. Methods of simulating thin film deposition using spray pyrolysis techniques. *Microelectronic Engineering*, 117:57–66, 2014.

[5] Yu Xie, Siyi Gao, and Morteza Eslamian. Fundamental study on the effect of spray parameters on characteristics of p3ht: Pcbm active layers made by spray coating. *Coatings*, 5(3):488–510, 2015.

[6] B Fleury, G Dantelle, S Darbe, JP Boilot, and T Gacoin. Transparent coatings made from spray deposited colloidal suspensions. *Langmuir*, 28(20):7639–7645, 2012.

[7] Daniel Langley, Gaël Giusti, Céline Mayousse, Caroline Celle, Daniel Bellet, and Jean-Pierre Simonato. Flexible transparent conductive materials based on silver nanowire networks: a review. *Nanotechnology*, 24(45):452001, 2013.

[8] Samira Naghdi, Kyong Yop Rhee, David Hui, and Soo Jin Park. A review of conductive metal nanomaterials as conductive, transparent, and flexible coatings, thin films, and conductive fillers: Different deposition methods and applications. *Coatings*, 8(8):278, 2018.

[9] Thomas Sannicolo, Mélanie Lagrange, Anthony Cabos, Caroline Celle, Jean-Pierre Simonato, and Daniel Bellet. Metallic nanowire-based transparent electrodes for next generation flexible devices: a review. *Small*, 12(44):6052–6075, 2016.

[10] Theo Henckens. Scarce mineral resources: Extraction, consumption and limits of sustainability. *Resources, Conservation and Recycling*, 169:105511, 2021.

[11] Ursus Wehrli, Geri Born, Daniel Spehr, and Daniel Spehr. *Die Kunst, aufzuräumen*. Kein & Aber Zürich, 2011.

[12] Janghoon Park, Keehyun Shin, and Changwoo Lee. Roll-to-roll coating technology and its applications: A review. *International Journal of Precision Engineering and Manufacturing*, 17(4):537–550, 2016.

[13] Robert Abbel, Yulia Galagan, and Pim Groen. Roll-to-roll fabrication of solution processed electronics. *Advanced Engineering Materials*, 20(8):1701190, 2018.

[14] Shanmuga Sundar Dhanabalan and Sivanantharaja Avaninathan. Review of flexible substrates suitable for opto-electronic devices. *International Journal of Applied Engineering Research*, 10:21293–21295, 01 2015.

[15] John Mackenzie Grant Cowie and Valeria Arrighi. *Polymers: chemistry and physics of modern materials*. CRC press, 2007.

[16] Muhammad Khalil, Shaukat Saeed, and Zahoor Ahmad. Properties of binary polyimide blends containing hexafluoroisopropylidene group. *Journal of Macromolecular Science Part A: Pure and Applied Chemistry*, 44(1):55–63, 2007.

[17] Saeed Rahemi Ardekani, Alireza Sabour Rouh Aghdam, Mojtaba Nazari, Amir Bayat, Elnaz Yazdani, and Esmaiel Saievar-Iranizad. A comprehensive review on ultrasonic spray pyrolysis technique: Mechanism, main parameters and applications in condensed matter. *Journal of Analytical and Applied Pyrolysis*, 141:104631, 2019.

[18] Robert J Lang. Ultrasonic atomization of liquids. *The journal of the acoustical society of America*, 34(1):6–8, 1962.

[19] Raghavachari Rajan and Aniruddha B Pandit. Correlations to predict droplet size in ultrasonic atomisation. *Ultrasonics*, 39(4):235–255, 2001.

[20] Dainius Perednis and Ludwig J Gauckler. Thin film deposition using spray pyrolysis. *Journal of electroceramics*, 14(2):103–111, 2005.

[21] Peter J Yunker, Tim Still, Matthew A Lohr, and AG Yodh. Suppression of the coffee-ring effect by shape-dependent capillary interactions. *Nature*, 476(7360):308–311, 2011.

[22] Robert D Deegan, Olgica Bakajin, Todd F Dupont, Greb Huber, Sidney R Nagel, and Thomas A Witten. Capillary flow as the cause of ring stains from dried liquid drops. *Nature*, 389(6653):827–829, 1997.

[23] Dileep Mampallil, Julien Reboud, Rab Wilson, Douglas Wylie, David R Klug, and Jonathan M Cooper. Acoustic suppression of the coffee-ring effect. *Soft matter*, 11(36):7207–7213, 2015.

[24] H Burak Eral, D Mampallil Augustine, Michael HG Duits, and Frieder Mugele. Suppressing the coffee stain effect: how to control colloidal self-assembly in evaporating drops using electrowetting. *Soft Matter*, 7(10):4954–4958, 2011.

[25] Maryam Parsa, Souad Harmand, and Khellil Sefiane. Mechanisms of pattern formation from dried sessile drops. *Advances in colloid and interface science*, 254:22–47, 2018.

[26] Nagesh D Patil, Prathamesh G Bange, Rajneesh Bhardwaj, and Atul Sharma. Effects of substrate heating and wettability on evaporation dynamics and deposition patterns for a sessile water droplet containing colloidal particles. *Langmuir*, 32(45):11958–11972, 2016.

[27] Dileep Mampallil, Meenakshi Sharma, Ashwini Sen, and Shubham Sinha. Beyond the coffee-ring effect: Pattern formation by wetting and spreading of drops. *Physical Review E*, 98(4):043107, 2018.

[28] Thomas Young. Iii. an essay on the cohesion of fluids. *Philosophical transactions of the royal society of London*, (95):65–87, 1805.

[29] Yueh-Feng Li, Yu-Jane Sheng, and Heng-Kwong Tsao. Evaporation stains: suppressing the coffee-ring effect by contact angle hysteresis. *Langmuir*, 29(25):7802–7811, 2013.

[30] Liying Cui, Junhu Zhang, Xuemin Zhang, Yunfeng Li, Zhanhua Wang, Hainan Gao, Tieqiang Wang, Shoujun Zhu, Hailing Yu, and Bai Yang. Avoiding coffee ring structure based on hydrophobic silicon pillar arrays during single-drop evaporation. *Soft Matter*, 8(40):10448–10456, 2012.

[31] Dileep Mampallil and Huseyin Burak Eral. A review on suppression and utilization of the coffee-ring effect. *Advances in colloid and interface science*, 252:38–54, 2018.

[32] Yanan Li, Qiang Yang, Mingzhu Li, and Yanlin Song. Rate-dependent interface capture beyond the coffee-ring effect. *Scientific reports*, 6(1):1–8, 2016.

[33] Tuan AH Nguyen, Marc A Hampton, and Anh V Nguyen. Evaporation of nanoparticle droplets on smooth hydrophobic surfaces: the inner coffee ring deposits. *The Journal of Physical Chemistry C*, 117(9):4707–4716, 2013.

[34] Martin ER Shanahan. Simple theory of" stick-slip" wetting hysteresis. *Langmuir*, 11(3):1041–1043, 1995.

[35] Tony M Yen, Xin Fu, Tao Wei, Roshan U Nayak, Yuesong Shi, and Yu-Hwa Lo. Reversing coffee-ring effect by laser-induced differential evaporation. *Scientific reports*, 8(1):1–11, 2018.

[36] K Badeker. Concerning the electricity conductibility and the thermoelectric energy of several heavy metal bonds. *Annalen der Physik*, 22:749, 1907.

[37] G Haacke. New figure of merit for transparent conductors. *Journal of Applied Physics*, 47(9):4086–4089, 1976.

[38] Lukas Kinner, Emil JW List-Kratochvil, and Theodoros Dimopoulos. Gentle plasma process for embedded silver-nanowire flexible transparent electrodes on temperature-sensitive polymer substrates. *Nanotechnology*, 31(36):365303, 2020.

[39] José A. Solera-Rojas, Marisol Ledezma-Gairaud, and Leslie W. Pineda. *Dye-sensitized Devices: Photovoltaic and Photoelectrolytic Applications*, pages 317–336. 2018.

[40] Caroline Celle, Céline Mayousse, Eléonore Moreau, Henda Basti, Alexandre Carella, and Jean-Pierre Simonato. Highly flexible transparent film heaters based on random networks of silver nanowires. *Nano Research*, 5(6):427–433, 2012.

[41] Qijin Huang, Wenfeng Shen, Xingzhong Fang, Guofei Chen, Junchao Guo, Wei Xu, Ruiqin Tan, and Weijie Song. Highly flexible and transparent film heaters based on polyimide films embedded with silver nanowires. *RSC Advances*, 5(57):45836–45842, 2015.

[42] Dorina T Papanastasiou, Amélie Schultheiss, David Muñoz-Rojas, Caroline Celle, Alexandre Carella, Jean-Pierre Simonato, and Daniel Bellet. Transparent heaters: a review. *Advanced Functional Materials*, 30(21):1910225, 2020.

[43] Harold A Mcmaster. Conductive coating for glass and method of application, October 21 1947. US Patent 2,429,420.

[44] Klaus Ellmer. Past achievements and future challenges in the development of optically transparent electrodes. *Nature Photonics*, 6(12):809–817, 2012.

[45] Alicia de Andrés, Félix Jiménez-Villacorta, and Carlos Prieto. *The Compromise Between Conductivity and Transparency*, pages 1–30. 2018.

[46] Klaus Ellmer, Rainald Mientus, and Stefan Seeger. *Metallic Oxides (ITO, ZnO, SnO2 , TiO2)*, pages 31–80. 2018.

[47] Grzegorz Luka, Tomasz Krajewski, Lukasz Wachnicki, Bartlomiej Witkowski, Elzbieta Lusakowska, Wojciech Paszkowicz, Elzbieta Guziewicz, and Marek Godlewski. Transparent and conductive undoped zinc oxide thin films grown by atomic layer deposition. *physica status solidi (a)*, 207(7):1568–1571, 2010.

[48] Huiyong Liu, V Avrutin, N Izyumskaya, Ü Özgür, and H Morkoç. Transparent conducting oxides for electrode applications in light emitting and absorbing devices. *Superlattices and Microstructures*, 48(5):458–484, 2010.

[49] S Edinger, N Bansal, M Bauch, RA Wibowo, G Újvári, R Hamid, G Trimmel, and T Dimopoulos. Highly transparent and conductive indium-doped zinc oxide films deposited at low substrate temperature by spray pyrolysis from water-based solutions. *Journal of Materials Science*, 52(14):8591–8602, 2017.

[50] Nina Winkler, Adhi Rachmat Wibowo, Bernhard Kubicek, Wolfgang Kautek, Giovanni Ligorio, Emil JW List-Kratochvil, and Theodoros Dimopoulos. Rapid processing of in-doped zno by spray pyrolysis from environment-friendly precursor solutions. *Coatings*, 9(4):245, 2019.

[51] E Fortunato, L Raniero, L Silva, A Goncalves, A Pimentel, P Barquinha, H Aguas, L Pereira, G Goncalves, I Ferreira, et al. Highly stable transparent and conducting gallium-doped zinc oxide thin films for photovoltaic applications. *Solar Energy Materials and Solar Cells*, 92(12):1605–1610, 2008.

[52] Akbar Eshaghi and Mohammad Hajkarimi. Optical and electrical properties of aluminum zinc oxide (azo) nanostructured thin film deposited on polycarbonate substrate. *Optik*, 125(19):5746–5749, 2014.

[53] AV Moholkar, SM Pawar, KY Rajpure, CH Bhosale, and JH Kim. Effect of fluorine doping on highly transparent conductive spray deposited nanocrystalline tin oxide thin films. *Applied Surface Science*, 255(23):9358–9364, 2009.

[54] Andre K Geim and Konstantin S Novoselov. The rise of graphene. In *Nanoscience and technology: a collection of reviews from nature journals*, pages 11–19. World Scientific, 2010.

[55] Hideki Shirakawa. Nobel lecture: the discovery of polyacetylene film—the dawning of an era of conducting polymers. *Reviews of Modern Physics*, 73(3):713, 2001.

[56] Philip Richard Wallace. The band theory of graphite. *Physical review*, 71(9):622, 1947.

[57] Zhuangchun Wu, Zhihong Chen, Xu Du, Jonathan M Logan, Jennifer Sippel, Maria Nikolou, Katalin Kamaras, John R Reynolds, David B Tanner, Arthur F Hebard, et al. Transparent, conductive carbon nanotube films. *Science*, 305(5688):1273–1276, 2004.

[58] George Gruner. Carbon nanotube films for transparent and plastic electronics. *Journal of Materials Chemistry*, 16(35):3533–3539, 2006.

[59] Edgar J López-Naranjo, Luis J González-Ortiz, Luis M Apátiga, Eric M Rivera-Muñoz, and Alejandro Manzano-Ramírez. Transparent electrodes: a review of the use of carbon-based nanomaterials. *Journal of Nanomaterials*, 2016, 2016.

[60] Jose Abad and Javier Padilla. *Transparent Conductive Polymers*, pages 193–244. 2018.

[61] Kuan Sun, Shupeng Zhang, Pengcheng Li, Yijie Xia, Xiang Zhang, Donghe Du, Furkan Halis Isikgor, and Jianyong Ouyang. Review on application of pedots and pedot: Pss in energy conversion and storage devices. *Journal of Materials Science: Materials in Electronics*, 26(7):4438–4462, 2015.

[62] Tatsuhiro Horii, Yuechen Li, Yusaku Mori, and Hidenori Okuzaki. Correlation between the hierarchical structure and electrical conductivity of pedot/pss. *Polymer Journal*, 47(10):695–699, 2015.

[63] Yuta Mochizuki, Tatsuhiro Horii, and Hidenori Okuzaki. Effect of ph on structure and conductivity of pedot/pss. *Transactions of the Materials Research Society of Japan*, 37(2):307–310, 2012.

[64] Oleg P Dimitriev, Yuri P Piryatinski, and Alexander A Pud. Evidence of the controlled interaction between pedot and pss in the pedot: Pss complex via concentration changes of the complex solution. *The Journal of Physical Chemistry B*, 115(6):1357–1362, 2011.

[65] Magatte N Gueye, Alexandre Carella, Jérôme Faure-Vincent, Renaud Demadrille, and Jean-Pierre Simonato. Progress in understanding structure and transport properties of pedot-based materials: A critical review. *Progress in Materials Science*, 108:100616, 2020.

[66] Yifan Yao, Huanli Dong, and Wenping Hu. Charge transport in organic and polymeric semiconductors for flexible and stretchable devices. *Advanced Materials*, 28(22):4513–4523, 2016.

[67] Hui Shi, Congcong Liu, Qinglin Jiang, and Jingkun Xu. Effective approaches to improve the electrical conductivity of pedot: Pss: a review. *Advanced Electronic Materials*, 1(4):1500017, 2015.

[68] Alexandre Mantovani Nardes, Martijn Kemerink, René AJ Janssen, Jolanda AM Bastiaansen, Nicole MM Kiggen, Bea MW Langeveld, Albert JJM Van Breemen, and Margreet M De Kok. Microscopic understanding of the anisotropic conductivity of pedot: Pss thin films. *Advanced Materials*, 19(9):1196–1200, 2007.

[69] JY Kim, JH Jung, DE Lee, and Jinsoo Joo. Enhancement of electrical conductivity of poly (3, 4-ethylenedioxythiophene)/poly (4-styrenesulfonate) by a change of solvents. *Synthetic Metals*, 126(2-3):311–316, 2002.

[70] Jianyong Ouyang, Qianfei Xu, Chi-Wei Chu, Yang Yang, Gang Li, and Joseph Shinar. On the mechanism of conductivity enhancement in poly (3, 4-ethylenedioxythiophene): poly (styrene sulfonate) film through solvent treatment. *Polymer*, 45(25):8443–8450, 2004.

[71] Charles E. Mortimer, Johannes Beck, and Ulrich Müller. *Chemie : das Basiswissen der Chemie*. Thieme, Stuttgart [u.a.], 2014.

[72] Selina Goetz, Rachmat Adhi Wibowo, Martin Bauch, Neha Bansal, Giovanni Ligorio, Emil List-Kratochvil, Christian Linke, Enrico Franzke, Jörg Winkler, Markus Valtiner, et al. Fast sputter deposition of moo x/metal/moo x transparent electrodes on glass and pet substrates. *Journal of Materials Science*, 56(15):9047–9064, 2021.

[73] Lukas Kinner, Martin Bauch, Rachmat Adhi Wibowo, Giovanni Ligorio, Emil JW List-Kratochvil, and Theodoros Dimopoulos. Polymer interlayers on flexible pet substrates enabling ultra-high performance, ito-free dielectric/metal/dielectric transparent electrode. *Materials & Design*, 168:107663, 2019.

[74] Serhiy Z Malynych and George Chumanov. Vacuum deposition of silver island films on chemically modified surfaces. *Journal of Vacuum Science & Technology A: Vacuum, Surfaces, and Films*, 21(3):723–727, 2003.

[75] David R Lide. *CRC handbook of chemistry and physics*, volume 85. CRC press, 2004.

[76] Hsun-Chen Chu, Yen-Chen Chang, Yow Lin, Shu-Hao Chang, Wei-Chung Chang, Guo-An Li, and Hsing-Yu Tuan. Spray-deposited large-area copper nanowire transparent conductive electrodes and their uses for touch screen applications. *ACS applied materials & interfaces*, 8(20):13009–13017, 2016.

[77] Sooyeon Lim, Donggeon Han, Hoyeon Kim, Soohyun Lee, and Seunghyup Yoo. Cu-based multilayer transparent electrodes: A low-cost alternative to ito electrodes in organic solar cells. *Solar Energy Materials and Solar Cells*, 101:170–175, 2012.

[78] Johannes HM Maurer, Lola González-García, Beate Reiser, Ioannis Kanelidis, and Tobias Kraus. Sintering of ultrathin gold nanowires for transparent electronics. *ACS applied materials & interfaces*, 7(15):7838–7842, 2015.

[79] Enrico Della Gaspera, Yong Peng, Qicheng Hou, Leone Spiccia, Udo Bach, Jacek J Jasieniak, and Yi-Bing Cheng. Ultra-thin high efficiency semitransparent perovskite solar cells. *Nano Energy*, 13:249–257, 2015.

[80] Chao Chen and Changhui Ye. *Metal Nanowires*, pages 105–131. 2018.

[81] Yugang Sun, Byron Gates, Brian Mayers, and Younan Xia. Crystalline silver nanowires by soft solution processing. *Nano letters*, 2(2):165–168, 2002.

[82] Dan Shan, Lumin Liu, Zhao Chen, Jianwei Zhang, Runmeng Cui, Enlv Hong, and Baiqi Wang. Controlled hydrothermal synthesis of ag nanowires and their antimicrobial properties. *Arabian Journal of Chemistry*, 14(3):102978, 2021.

[83] Sangyeob Lee, Jiseong Jang, Taejun Park, Young Min Park, Joon Sik Park, Yoon-Kee Kim, Hyoung-Keun Lee, Eun-Chae Jeon, Doh-Kwon Lee, Byungmin Ahn, et al. Electrodeposited silver nanowire transparent conducting electrodes for thin-film solar cells. *ACS applied materials & interfaces*, 12(5):6169–6175, 2020.

[84] Garo Khanarian, Jaebum Joo, X-Q Liu, Peter Eastman, Daniel Werner, K O'Connell, and Peter Trefonas. The optical and electrical properties of silver nanowire mesh films. *Journal of Applied Physics*, 114(2):024302, 2013.

[85] Hugh G Manning, Claudia Gomes da Rocha, Colin O'Callaghan, Mauro S Ferreira, and John J Boland. The electro-optical performance of silver nanowire networks. *Scientific reports*, 9(1):1–9, 2019.

[86] Yugang Sun, Brian Mayers, Thurston Herricks, and Younan Xia. Polyol synthesis of uniform silver nanowires: a plausible growth mechanism and the supporting evidence. *Nano letters*, 3(7):955–960, 2003.

[87] Sujie Chang, Kai Chen, Qing Hua, Yunsheng Ma, and Weixin Huang. Evidence for the growth mechanisms of silver nanocubes and nanowires. *The Journal of Physical Chemistry C*, 115(16):7979–7986, 2011.

[88] Y Gao, P Jiang, DF Liu, HJ Yuan, XQ Yan, ZP Zhou, JX Wang, L Song, LF Liu, WY Zhou, et al. Evidence for the monolayer assembly of poly (vinylpyrrolidone) on the surfaces of silver nanowires. *The Journal of Physical Chemistry B*, 108(34):12877–12881, 2004.

[89] Jian-Yang Lin, Yu-Lee Hsueh, and Jung-Jie Huang. The concentration effect of capping agent for synthesis of silver nanowire by using the polyol method. *Journal of Solid State Chemistry*, 214:2–6, 2014.

[90] Dietrich Stauffer and Ammon Aharony. *Introduction to percolation theory*. CRC press, 2018.

[91] Ming Li, Run-Ran Liu, Linyuan Lü, Mao-Bin Hu, Shuqi Xu, and Yi-Cheng Zhang. Percolation on complex networks: Theory and application. *Physics Reports*, 2021.

[92] M Lagrange, DP Langley, G Giusti, Carmen Jiménez, Y Bréchet, and Daniel Bellet. Optimization of silver nanowire-based transparent electrodes: effects of density, size and thermal annealing. *Nanoscale*, 7(41):17410–17423, 2015.

[93] Nicholas Fata, Shreshtha Mishra, Ying Xue, Yunong Wang, Jeremy Hicks, and Ant Ural. Effect of junction-to-nanowire resistance ratio on the percolation conductivity and critical exponents of nanowire networks. *Journal of Applied Physics*, 128(12):124301, 2020.

[94] Daniel Bellet, Mélanie Lagrange, Thomas Sannicolo, Sara Aghazadehchors, Viet Huong Nguyen, Daniel P Langley, David Muñoz-Rojas, Carmen Jiménez, Yves Bréchet, and Ngoc Duy Nguyen. Transparent electrodes based on silver nanowire networks: From physical considerations towards device integration. *Materials*, 10(6):570, 2017.

[95] Andrea Ponzoni. The contributions of junctions and nanowires/nanotubes in conductive networks. *Applied Physics Letters*, 114(15):153105, 2019.

[96] Milan Žeželj and Igor Stanković. From percolating to dense random stick networks: Conductivity model investigation. *Physical Review B*, 86(13):134202, 2012.

[97] Claudia Gomes da Rocha, Hugh G Manning, Colin O'Callaghan, Carlos Ritter, Allen T Bellew, John J Boland, and Mauro S Ferreira. Ultimate conductivity performance in metallic nanowire networks. *Nanoscale*, 7(30):13011–13016, 2015.

[98] Colin O'Callaghan, Claudia Gomes da Rocha, Hugh G Manning, John J Boland, and Mauro S Ferreira. Effective medium theory for the conductivity of disordered metallic nanowire networks. *Physical Chemistry Chemical Physics*, 18(39):27564–27571, 2016.

[99] GE Pike and CH Seager. Percolation and conductivity: A computer study. i. *Physical review B*, 10(4):1421, 1974.

[100] Franz Selzer, Carlo Floresca, David Kneppe, Ludwig Bormann, Christoph Sachse, Nelli Weiß, Alexander Eychmüller, Aram Amassian, Lars Müller-Meskamp, and Karl Leo. Electrical limit of silver nanowire electrodes: Direct measurement of the nanowire junction resistance. *Applied Physics Letters*, 108(16):163302, 2016.

[101] Jiun-Yi Tseng, Ling Lee, Yu-Chen Huang, Jung-Hao Chang, Teng-Yu Su, Yu-Chuan Shih, Hao-Wu Lin, and Yu-Lun Chueh. Pressure welding of silver nanowires networks at room temperature as transparent electrodes for efficient organic light-emitting diodes. *Small*, 14(38):1800541, 2018.

[102] Chih-Jui Ni and Franklin Chau-Nan Hong. Electroless nanowelding of silver nanowires at room temperature. *RSC Advances*, 4(76):40330–40338, 2014.

[103] Arash Vafaei, Anming Hu, and Irene A Goldthorpe. Joining of individual silver nanowires via electrical current. *Nano-Micro Letters*, 6(4):293–300, 2014.

[104] Milind Jagota and Isaac Scheinfeld. Analytical modeling of orientation effects in random nanowire networks. *Physical Review E*, 101(1):012304, 2020.

[105] Ankush Kumar, NS Vidhyadhiraja, and Giridhar U Kulkarni. Current distribution in conducting nanowire networks. *Journal of Applied Physics*, 122(4):045101, 2017.

[106] Liangbing Hu, David S Hecht, and George Gruner. Carbon nanotube thin films: fabrication, properties, and applications. *Chemical reviews*, 110(10):5790–5844, 2010.

[107] Sidney Redner. Fractal and multifractal scaling of electrical conduction in random resistor networks. *arXiv preprint arXiv:0710.1105*, 2007.

[108] Yasuo Chiba, Ashraful Islam, Ryoichi Komiya, Naoki Koide, and Liyuan Han. Conversion efficiency of 10.8% by a dye-sensitized solar cell using a ti o 2 electrode with high haze. *Applied Physics Letters*, 88(22):223505, 2006.

[109] Corsin Battaglia, Jordi Escarré, Karin Söderström, Mathieu Charriere, Matthieu Despeisse, Franz-Josef Haug, and Christophe Ballif. Nanomoulding of transparent zinc oxide electrodes for efficient light trapping in solar cells. *Nature Photonics*, 5(9):535–538, 2011.

[110] Xiao-Yan Zeng, Qi-Kai Zhang, Rong-Min Yu, and Can-Zhong Lu. A new transparent conductor: silver nanowire film buried at the surface of a transparent polymer. *Advanced materials*, 22(40):4484–4488, 2010.

[111] Richard D Glover, John M Miller, and James E Hutchison. Generation of metal nanoparticles from silver and copper objects: nanoparticle dynamics on surfaces and potential sources of nanoparticles in the environment. *ACS nano*, 5(11):8950–8957, 2011.

[112] Céline Mayousse, Caroline Celle, Alexandra Fraczkiewicz, and Jean-Pierre Simonato. Stability of silver nanowire based electrodes under environmental and electrical stresses. *Nanoscale*, 7(5):2107–2115, 2015.

[113] Wen Zhang, Ying Yao, Nicole Sullivan, and Yongsheng Chen. Modeling the primary size effects of citrate-coated silver nanoparticles on their ion release kinetics. *Environmental science & technology*, 45(10):4422–4428, 2011.

[114] Tanya S Peretyazhko, Qingbo Zhang, and Vicki L Colvin. Size-controlled dissolution of silver nanoparticles at neutral and acidic ph conditions: kinetics and size changes. *Environmental science & technology*, 48(20):11954–11961, 2014.

[115] S Chen, L Song, Z Tao, X Shao, Y Huang, Q Cui, and X Guo. Neutral-ph pedot: Pss as over-coating layer for stable silver nanowire flexible transparent conductive films. *Organic Electronics*, 15(12):3654–3659, 2014.

[116] Seyul Kim, So Yeon Kim, Moon Hyun Chung, Jeonghun Kim, and Jung Hyun Kim. A one-step roll-to-roll process of stable agnw/pedot: Pss solution using imidazole as a mild base for highly conductive and transparent films: optimizations and mechanisms. *Journal of Materials Chemistry C*, 3(22):5859–5868, 2015.

[117] Joseph Cameron and Peter J Skabara. The damaging effects of the acidity in pedot: Pss on semiconductor device performance and solutions based on non-acidic alternatives. *Materials Horizons*, 7(7):1759–1772, 2020.

[118] Shiwei Long, Xun Cao, Guangyao Sun, Ning Li, Tianci Chang, Zewei Shao, and Ping Jin. Effects of v2o3 buffer layers on sputtered vo2 smart windows: Improved thermochromic properties, tunable width of hysteresis loops and enhanced durability. *Applied Surface Science*, 441:764–772, 2018.

[119] Jiadong Zhou, Yanfeng Gao, Zongtao Zhang, Hongjie Luo, Chuanxiang Cao, Zhang Chen, Lei Dai, and Xinling Liu. Vo 2 thermochromic smart window for energy savings and generation. *Scientific reports*, 3(1):1–5, 2013.

[120] Magatte N Gueye, Alexandre Carella, Renaud Demadrille, and Jean-Pierre Simonato. All-polymeric flexible transparent heaters. *ACS applied materials & interfaces*, 9(32):27250–27256, 2017.

[121] Xin He, Xuyang Hu, Mingxia Song, Feng Duan, Qiuming Lan, Jundong Xiao, Junyan Liu, Mei Zhang, Yeqing Chen, and Qingguang Zeng. Temperature-controlled transparent-film heater based on silver nanowire–pmma composite film. *Nanotechnology*, 27(47):475709, 2016.

[122] Dorina T Papanastasiou, Nicolas Charvin, Joao Resende, Viet Huong Nguyen, Abderrahime Sekkat, David Muñoz-Rojas, Carmen Jiménez, Lionel Flandin, and Daniel Bellet. Effects of non-homogeneity and oxide coating on silver nanowire networks under electrical stress: comparison between experiment and modeling. *Nanotechnology*, 32(44):445702, 2021.

[123] Su-juan Yu, Yong-guang Yin, Jing-bo Chao, Mo-hai Shen, and Jing-fu Liu. Highly dynamic pvp-coated silver nanoparticles in aquatic environments: chemical and morphology change induced by oxidation of ag0 and reduction of ag+. *Environmental science & technology*, 48(1):403–411, 2014.

[124] Yinqing Zhang, Junchao Xia, Jinliang Xu, Binbin Sun, Wei Wu, and Lingyan Zhu. Impacts of surfactants on dissolution and sulfidation of silver nanowires in aquatic environments. *Environmental Science: Nano*, 5(10):2452–2460, 2018.

[125] Matthew J Large, Jake Burn, Alice A King, Sean P Ogilvie, Izabela Jurewicz, and Alan B Dalton. Predicting the optoelectronic properties of nanowire films based on control of length polydispersity. *Scientific reports*, 6(1):1–6, 2016.

[126] Joseph Palathinkal Thomas, Liyan Zhao, Donald McGillivray, and Kam Tong Leung. High-efficiency hybrid solar cells by nanostructural modification in pedot: Pss with co-solvent addition. *Journal of Materials Chemistry A*, 2(7):2383–2389, 2014.

[127] Anang WM Diah, Clovia I Holdsworth, Darfiana Nur, and Eric Beh. Statistical modelling of the conductivity performance of poly (3, 4-ethylenedioxythiophene/poly (styrene sulfonic acid) films. *Current Analytical Chemistry*, 12(2):124–140, 2016.

[128] Jonathan Crepelliere, Kevin Menguelti, Sabrina Wack, Olivier Bouton, Mathieu Gerard, Petru Lunca Popa, Bianca Rita Pistillo, Renaud Leturcq, and Marc Michel. Spray deposition of silver nanowires on large area substrates for transparent electrodes. *ACS Applied Nano Materials*, 4(2):1126–1135, 2021.

[129] Sadie I White, Rose M Mutiso, Patrick M Vora, David Jahnke, Sam Hsu, James M Kikkawa, Ju Li, John E Fischer, and Karen I Winey. Electrical percolation behavior in silver nanowire–polystyrene composites: simulation and experiment. *Advanced Functional Materials*, 20(16):2709–2716, 2010.

[130] Aveek Bid, Achyut Bora, and AK Raychaudhuri. Temperature dependence of the resistance of metallic nanowires of diameter 15 nm: Applicability of bloch-grüneisen theorem. *Physical Review B*, 74(3):035426, 2006.

[131] Surface tension values of some common test liquids for surface energy analysis. http://www.surface-tension.de/.

[132] Santosh Kumar, Manoj Kumar, and Neeru Jindal. Overview of cold spray coatings applications and comparisons: a critical review. *World Journal of Engineering*, 2020.

[133] Pieter Verding, Wim Deferme, and Werner Steffen. Velocity and size measurement of droplets from an ultrasonic spray coater using photon correlation spectroscopy and turbidimetry. *Applied Optics*, 59(25):7496–7503, 2020.

[134] Mikita Marus, Aliaksandr Hubarevich, Wei Jun Fan, Hong Wang, A Smirnov, K Wang, H Huang, and XW Sun. Optical haze of randomly arranged silver nanowire transparent conductive films with wide range of nanowire diameters. *Aip Advances*, 8(3):035201, 2018.

[135] Shengrong Ye, Aaron R Rathmell, Zuofeng Chen, Ian E Stewart, and Benjamin J Wiley. Metal nanowire networks: the next generation of transparent conductors. *Advanced materials*, 26(39):6670–6687, 2014.

[136] Sajad Haghanifar, Rafael T Rodriguez De Vecchis, Ki-Joong Kim, Jeffrey Wuenschell, Sooraj P Sharma, Ping Lu, Paul Ohodnicki, and Paul W Leu. Flexible nanograss with highest combination of transparency and haze for optoelectronic plastic substrates. *Nanotechnology*, 29(42):42LT01, 2018.

[137] Nasim Sahraei, Karen Forberich, Selvaraj Venkataraj, Armin G Aberle, and Marius Peters. Analytical solution for haze values of aluminium-induced texture (ait) glass superstrates for a-si: H solar cells. *Optics Express*, 22(101):A53–A67, 2014.

[138] Yunkyung Kim. Investigation of silver nanowires with a pedot: Pss layer for haze reduction. *Journal of the Korean Physical Society*, 69(8):1391–1396, 2016.

[139] Saahil Mehra, Mark G Christoforo, Peter Peumans, and Alberto Salleo. Solution processed zinc oxide nanopyramid/silver nanowire transparent network films with highly tunable light scattering properties. *Nanoscale*, 5(10):4400–4403, 2013.

[140] Dong Chul Choo and Tae Whan Kim. Degradation mechanisms of silver nanowire electrodes under ultraviolet irradiation and heat treatment. *Scientific reports*, 7(1):1–12, 2017.

[141] Jinting Jiu, Jun Wang, Tohru Sugahara, Shijio Nagao, Masaya Nogi, Hirotaka Koga, Katsuaki Suganuma, Masanao Hara, Eri Nakazawa, and Hiroshi Uchida. The effect of light and humidity on the stability of silver nanowire transparent electrodes. *Rsc Advances*, 5(35):27657–27664, 2015.

[142] M Lagrange, T Sannicolo, D Muñoz-Rojas, B Guillo Lohan, A Khan, M Anikin, Carmen Jiménez, F Bruckert, Y Bréchet, and D Bellet. Understanding the mechanisms leading to failure in metallic nanowire-based transparent heaters, and solution for stability enhancement. *Nanotechnology*, 28(5):055709, 2016.

[143] Jonathan Griffin, Anthony J Ryan, and David G Lidzey. Solution modification of pedot: Pss inks for ultrasonic spray coating. *Organic Electronics*, 41:245–250, 2017.

[144] Ganesh S Lonakar, Mrunal S Mahajan, Sanjay S Ghosh, and Jaydeep V Sali. Modeling thin film formation by ultrasonic spray method: A case of pedot: Pss thin films. *Organic Electronics*, 13(11):2575–2581, 2012.

[145] Shihao Liu, Xiang Zhang, Letian Zhang, and Wenfa Xie. Ultrasonic spray coating polymer and small molecular organic film for organic light-emitting devices. *Scientific reports*, 6(1):1–10, 2016.

[146] Fatemeh Zabihi and Morteza Eslamian. Substrate vibration-assisted spray coating (svasc): significant improvement in nano-structure, uniformity, and conductivity of pedot: Pss thin films for organic solar cells. *Journal of Coatings Technology and Research*, 12(4):711–719, 2015.

[147] F Zabihi, Y Xie, S Gao, and M Eslamian. Morphology, conductivity, and wetting characteristics of pedot: Pss thin films deposited by spin and spray coating. *Applied Surface Science*, 338:163–177, 2015.